UNIVERSITÀ DEGLI STUDI DI PADOVA

Sede Amministrativa : Università degli Studi di Padova

Dipartimento di FISICA ″GALILEO GALILEI″

SCUOLA DI DOTTORATO DI RICERCA IN FISICA
INDIRIZZO : FISICA NUCLEARE
CICLO XXI

The neutron capture cross sections of ^{186,187,188}Os and their application to Re/Os cosmochronometer

Direttore della Scuola : Ch.mo Prof. Attilio Stella
Supervisore : Ch.ma Prof.ssa Giovanna Montagnoli
Correlatori : Dott. Pierfrancesco Mastinu
Dott. Paolo Maria Milazzo

Dottoranda : Kaori Fujii

2 Febbraio 2009

NASEBA NARU.

Abstract

The aim of this thesis is a fine determination of ^{186,187,188}Os neutron capture cross sections, in order to remove principal nuclear physics uncertainties on the age of the universe determined using the Re/Os cosmochronometer.

A general introduction including stellar nucleosynthesis, nuclear cosmochronometry, available neutron facilities and neutron reaction features is given. Dedicated measurements of the ^{186,187,188}Os capture cross sections have been performed at the CERN neutron time-of-flight facility, n_TOF, in the neutron energy range from 1 eV up to 1 MeV. The details of the measurement and the data treatment are reported.

Using obtained capture yields, resolved resonance region analysis is completed. Resonance parameters have been extracted from a full R-matrix fit. A statistical analysis has been performed and the related averaged resonance parameters are derived. This information is crucial for a complete understanding and modeling in terms of the Hauser-Feshbach statistical model of the capture and inelastic reaction channels, required for the evaluation of the stellar reaction rates of these isotopes. The neutron capture cross sections averaged over the thermal neutron spectrum, Maxwellian averaged cross sections, for the range of temperatures relevant for s-process nucleosynthesis have been derived from the combined information of the experimental data in the resolved and unresolved resonance regions.

The implications of this analysis in the estimation of the s-process component of the ^{187}Os abundance and the related impact on the evaluation of the time-duration of the Galactic nucleosynthesis through the Re/Os cosmochronometer is shown. Moreover, further considerations for a realistic stellar condition, astration and s-process branchings are discussed. In conclusion, results of present analysis are compared with the alternative cosmic age by means of astronomical and cosmological ways.

Sommario

Scopo di questa tesi è una precisa determinazione delle sezioni d'urto di cattura neutronica di ^{186,187,188}Os, al fine di ridurre le indeterminazioni legate alla fisica nucleare nel calcolo dell'età dell'universo con il metodo del cosmo-cronometro Re/Os.

Innanzituto viene fornita una introduzione generale per inquadrare la nucleo-sintesi stellare, la cosmo-cronometria nucleare, i fasci di neutroni disponibili presso diversi laboratori e le caratteristiche generali delle reazioni indotte da neutroni. Misure dedicate allo studio delle sezioni d'urto di cattura neutronica di ^{186,187,188}Os sono state portate a termine presso la facility n_TOF del CERN, con neutroni di energia incidente compresa tra 1 eV ed 1 MeV. I dettagli di questa misura e l'analisi dei dati vengono qui riportati.

L'analisi della regione delle risonanze risolte è stata eseguita a partire dalla definizione degli spettri di cattura. I parametri di ogni risonanza sono stati estratti a partire da minimizzazioni che utilizzano la matrice R di Wigner. Inoltre è stata portata a termine una analisi statistica per estrarre i valori medi dei parametri delle risonanze. Quest'ultima informazione è fondamentale per una completa comprensione, nei termini del modello statistico di Hauser-Feschbach, dei processi di cattura o diffusione anelastica dei neutroni; questa informazione serve per la valutazione dei processi stellari che coinvolgono gli isotopi dell'Os. La convoluzione delle sezioni d'urto di cattura sullo spettro energetico dei neutroni (Maxwellian averaged cross sections), per temperature di interesse per processi di nucleo-sintesi attraverso il processo s, sono state ottenute combinando le informazioni sperimentali sia della regione delle risonanze risolte, sia quella delle risonanze non risolte.

Le implicazioni di questa analisi nella stima dell'abbondanza del ^{187}Os, generata da processi di nucleo-sintesi di tipo s, e la conseguente valutazione attraverso il cosmo-cronometro Re/Os della durata della nucleo-sintesi galattica è qui discussa. Inoltre vengono affrontate ulteriori considerazioni riguardanti le condizioni stellari, fenomeni di astrazione e ramificazioni lungo il processo s. Infine i risultati di questa analisi vengono confrontati con i valori dell'età dell'universo ottenuti utilizzando altri metodi, di carattere astronomico e cosmologico.

Contents

List of Tables

List of Figures

Chapter 1

Introduction

The study of neutron capture cross section has three principal motivations.

1. Basic nuclear physics : accurate and complete cross section data are providing a crucial test of nuclear reaction theory.
2. Nuclear astrophysics : neutron capture reactions in the energy range from 1 - 600 keV are the fundamental information for the formation of the heavy elements during stellar nucleosynthesis, and the Os isotopes are particularly important for the evaluation of the Re/Os cosmochronometer.
3. Nuclear technology : accurate neutron cross sections in the energy range from 1 keV - 2 MeV are essential for the reliable design of nuclear waste transmutation and future generation reactors.

The present work on the osmium isotopes is mainly concerned with the nuclear astrophysics issues, but touches also upon the basic physics aspects.

1.1 Synthesis of the elements in stars : from B^{2}FH to present

Nuclear astrophysics has been developed in the 20th century, and was essentially formulated as a well defined field of research by the seminal paper of Burbidge, Burbidge, Fowler and Hoyle (B^{2}FH) in 1957 [1]. In this work, eight processes were suggested to produce almost all known elements in stars. Forty years later, Wallerstein et al. [2] updated this work and summarized the most current information available. The following discussion provides a brief account of the processes proposed by B^{2}FH including the updated information of Ref. [2].

1.1.1 Hydrogen burning

This process is responsible for the energy production in main sequence stars as, for example, in the sun (the solar mass $\equiv M_\odot$). During hydrogen burn-

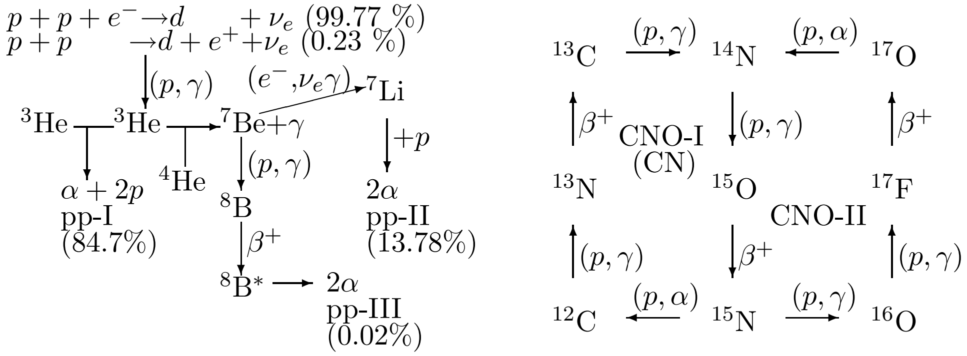

Figure 1.1: Hydrogen burning via the pp-chain (left) and the CNO cycle (right).

ing protons are fused into helium, which can be simply expressed by the sequence $4p \rightarrow {}^4\mathrm{He} + 2e^+ + 2\nu_e + 26.7$ MeV. Up to a stellar mass (M) of about 1.4 $M_\odot$, the lower central temperatures favor the so-called pp-chain whereas hydrogen burning in more massive stars proceeds via the CNO (carbon-nitrogen-oxygen) cycle. According to the reaction pattern one can distinguish pp-chain I, II, and III and CNO cycle as sketched in Fig. 1.1.

pp − chain ($M \leq 1.4\ M_\odot$): the initial reaction is $p + p \rightarrow d + e^+ + \nu_e$. The electron neutrinos produced in the β^+ decay are important for the Solar neutrino problem [3], which denotes the fact that the observed solar neutrino flux is only about one third of the flux expected from the solar luminosity. To explain this, neutrino oscillations were suggested and neutrino detection experiments performed [4].

CNO cycle (more massive main sequence stars): the main mechanism is the CNO-I cycle. The ^{14}N(p,γ)^{15}O reaction represents a bottleneck because it is the slowest reaction in the CNO-I cycle [5]. Consequently, the initial CNO abundances are almost completely transformed into ^{14}N. There are additional weak side branches (CNO-II, III, IV), which are of minor importance. At higher stellar temperatures, proton captures on ^{13}N become faster than the β^+ decay, marking the transition from the CNO cycle to the Hot-CNO cycle.

1.1.2 Helium burning

At the end of hydrogen burning in the stellar core, the core contracts and becomes hotter because of the gravitational energy. With the higher temperature, helium can be fused into carbon and oxygen. The main process during He burning is the triple α reaction ($^4\mathrm{He} + {}^4\mathrm{He} \leftrightarrows {}^8\mathrm{Be}$, $^8\mathrm{Be} + {}^4\mathrm{He} \leftrightarrows {}^{12}\mathrm{C}^* \rightarrow {}^{12}\mathrm{C} + \gamma$). In spite of the short life time of ^{8}Be at the density and temperature of the He burning environment, a small ^{8}Be abundance is built up to allow for the additional α capture to form ^{12}C. Some of the ^{12}C is subsequently transformed into ^{16}O by $^{12}\mathrm{C}(\alpha, \gamma)^{16}\mathrm{O}$ reactions. This reaction is difficult to study experimentally because of its extremely low cross section. For a discussion of various experimental approaches see Ref. [6].

1.1.3 The α (α capture) - process

B^2FH suggested that nucleosynthesis beyond ^{16}O could continue by further α capture reactions to ^{20} Ne, ^{24}Mg, etc., up to ^{40}Ca. However, it was shown experimentally that the $^{16}O(\alpha,\gamma)^{20}Ne$ rate is too slow to contribute to the synthesis of heavier nuclei. Instead, carbon and oxygen burning becomes the dominant mechanisms. Carbon and oxygen are the ashes of helium burning. Since oxygen is tightly bound, carbon burning (^{12}C + ^{12}C) is the next stage after helium burning, producing Ne and Na. The following processes are neon burning, which yields Mg and O, and oxygen burning (^{16}O + ^{16}O) producing Si and S. These series of progressive burning phases leads eventually to silicon burning where temperatures are becoming so high that nuclear fusion is challenged by reverse photodisintegration (see e-process). The main products of Si burning are the nuclei up to the iron peak of the abundance distribution [7].

1.1.4 The e (equilibrium) - process

This process, which almost merges with Si burning, is responsible for the origin of the iron peak (see Fig. 1.3). High energy thermal photons decompose some of the ^{28}Si into free α particles, which are captured on the remaining ^{28}Si nuclei to produce ^{32}S and heavier nuclei. In fact, the temperature becomes so high that all nuclear reactions involving proton, neutron, and α particles are in thermodynamic equilibrium with their inverse reactions. In this situation the resulting abundance distribution favors the most tightly bound nuclei around ^{56}Fe. This scenario is also called nuclear statistical equilibrium (NSE).

1.1.5 The s (slow neutron capture) - process

Beyond the iron group up to the actinides, s (slow) and r (rapid) neutron capture processes are the dominant reaction mechanisms because the fusion is no more convenient in terms of the biding energy. The terms slow and rapid refer to the time scale for neutron capture compared to the typical β decay times. Both processes are responsible for the synthesis of approximately half of the elements heavier than iron. Essentially all relevant features of these processes were already considered by B^2FH, in particular the fact that the s abundances are almost completely determined by the (n,γ) cross sections of the involved isotopes averaged over the stellar neutron spectrum. Through the continuous improvement of the experimental techniques, experimental uncertainties of these cross sections could be greatly reduced.

The s-process takes place in the helium-burning zones of Asymptotic Giant Branch (AGB) and massive stars ($> 10M_{\odot}$) at temperatures of $\sim 1 - 3.5 \times 10^8$ K and neutron density ($n_n \sim 10^8 - 10^{10}$ cm^{-1}). These temperatures and neutron density are relatively lower with respect to r-process. Neutrons are produced via ^{13}C$(\alpha, n)^{16}$O and ^{22}Ne$(\alpha, n)^{25}$Mg reactions with the ^{13}C being produced via ^{12}C$(p, \gamma)^{13}$N$(\beta^+)^{13}$C and ^{22}Ne from double α capture on ^{14}N left behind from the CNO cycle. Because of the slow neutron capture times the s-process path follows the valley of β stability. Over wide mass regions, the s-process abundances are inversely proportional to the respective (n, γ) cross sections, because reaction flow equilibrium has been achieved between magic neutron numbers. This results in the so-called local approximation,

$$\langle\sigma_A\rangle N_A = \text{constant}, \tag{1.1.1}$$

where $\langle\sigma\rangle$ is the Maxwellian averaged cross section (MACS). For details of the definition of the MACS and the local approximation see Appendix A and B, respectively. N is the abundance. The $\langle\sigma_A\rangle$N$_A$-curve plotted versus mass number (see Fig. 1.2) shows almost constant plateaus separated by pronounced steps at the magic neutron numbers N = 50, 82, and 126 ($A \sim$ 88, 140 and 208). The stellar (n, γ) cross sections are the essential nuclear information required for the underlying s-process models [8][9].

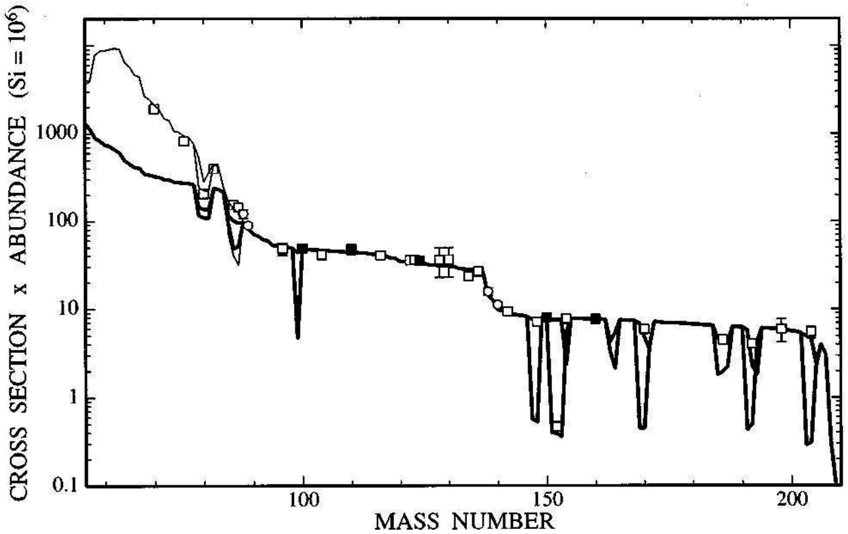

Figure 1.2: The characteristic product of cross section times s-process abundance plotted as a function of mass number [2]. Model calculations (solid line, see Appendix B) and the empirical values for the s-only nuclei (symbols) are in very good agreement.

1.1.6 The r (rapid neutron capture) - process

The r-process is characterized by neutron capture times as low as milliseconds, much faster compared to β-decay times ($\tau_n \ll \tau_\beta$). Generally speaking this process can be assigned to explosive scenarios such as supernovae explosion on the last day of the life in massive stars. Due to the extremely hot ($T > 10^9$ K) environments and high neutron densities ($n_n \gg 10^{20}$ cm^{-1}) associated with the r-process, the reaction path is shifted to the very neutron rich side of the stability valley close to the drip line where the binding energy becomes so low that further neutron captures are prevented by (γ, n) reactions with the hot stellar photon bath. The r abundances are determined by the half lives of these "waiting points". The neutron rich isotopes are thus ejected in the environment and the subsequent β-decay of the unstable isotopes populate the reaction of the elements between the neutron drip-line and the stability valley.

So far, models of the r-process are rather uncertain because of the difficulties in describing the explosion mechanism but also because the nuclear models have to be pushed to their limits for predicting the relevant nuclear properties near the drip line. One of the possible scenarios that were proposed in this context is an extremely α-rich freeze-out in Si burning [10].

1.1.7 The p (proton gain) - process

This process is required to produce the proton-rich (p) nuclei that are impossible to reach by neutron capture. It is assumed that the p nuclei originate from photo-disintegration reactions in high temperature zones of supernova explosions. Present models for the p-process are the γ-process, where a pre-existing seed distribution from the s or r-process is exposed to temperatures in excess of 2 GK. Under these conditions photon induced reactions give rise to a complex network connected by (γ, n), (γ, p), (γ, α) and their inverse reactions. This concept is capable to produce nearly all p nuclei in solar proportions. To some extent the rapid proton (rp)-process [11] and the νp-process [12] may contribute to the p nuclei with $A \leq 100$.

The recent review and model calculations can be found in [13].

Since explosive nucleosynthesis by the r and p-processes proceed off the stability valley, the experimental studies of the respective reaction rates have to rely on existing and upcoming radioactive ion beam facilities [6].

1.1.8 The x (unknown) - process

It is common to the rare light elements D, Li, Be and B to be very unstable at the conditions of the stellar interior, where they are easily converted into ^{4}He. Since their origin was unknown to B^{2}FH they were ascribed to a hypothetical x-process. The most likely production mechanism today is via spallation reactions induced by energetic Galactic cosmic rays on CNO nuclei.

1.2 Nuclear astrophysics : basic tools

The main goal of Nuclear Astrophysics is to interpret the observed isotopic abundance distributions in the Solar system and in the Universe in terms of the nuclear reactions responsible for the stellar energy and for the synthesis of the elements.

1.2.1 Nuclear abundances in the solar system

Figure 1.3 shows the solar abundance distribution as a function of mass number. In the mass region beyond Fe the s and r contributions are responsible for the double peaks at Ba/Te and Pb/Pt caused by the effect of magic neutron numbers $N = 82$ and 126. The sharper peaks at Ba and Pb are formed in the s-process and the broader ones at Te and Pt in the r-process. A similar but unresolved structure is related to $N = 50$ in the mass region between Ge and Zr.

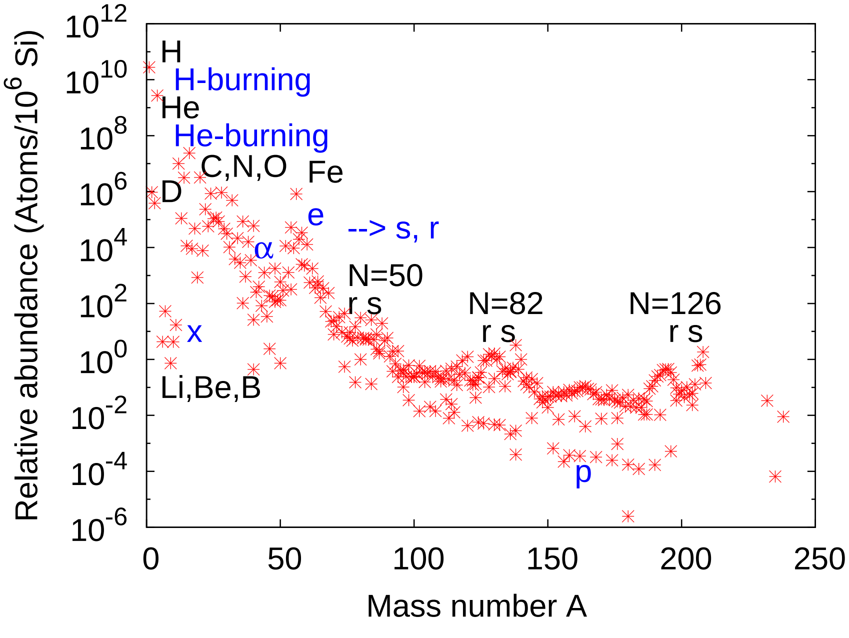

Figure 1.3: The abundances in the solar system. The data are from Ref. [14].

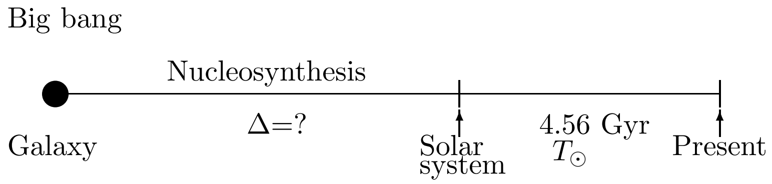

Figure 1.4: Time line of Nuclear cosmochronology.

1.2.2 Evolution of the universe

The evolution of the universe can be simplified by four stages. It is listed a series of passage of the time. Here after, **Gyr** is G(10^9) years.

1. Big bang nucleosynthesis with the production of the lightest elements such as ^{1}H, ^{2}H, ^{3}He,^{4}He, and ^{7}Li.
   (The time interval : the first few minutes.)
2. Galaxy formation.
   (The time interval $\equiv \delta < 1$ Gyr.)
3. Stellar nucleosynthesis with fusion reactions involving charged particles ($^4\mathrm{He} \sim A \lesssim 60$) and neutron capture nucleosynthesis in the s- and r-process complemented by the p-processes ($A \geq 60$) as discussed in Sec. 1.1.
   (The time interval $\equiv \Delta$, the subject of the Nuclear cosmochronology.)
4. Formation of the Solar System.
   (The time interval $\equiv T_\odot = 4.56$ Gyr [15].)

A simple sketch is shown in Fig. 1.4.

1.2.3 Nuclear cosmochronology

The age of the universe (T_u) can be obtained by summing over the duration of the four stages sketched above. The stage 1 and 2 should contribute less than 1 Gyr to the age. Nucleochronometer can be used to determine the age of the Galaxy (T_G) and hence provide a lower limit upon the age of the universe. In general the age is evaluated as $T_G = \Delta + T_\odot$ Gyr and $T_u = T_G$ + 0.5 Gyr assuming $\delta = 0.5$ Gyr.

One way of determining the duration of nucleosynthesis prior to the Solar system is to study the decay of long-lived nuclei. As shown in Table 1.1, the most promising cases are related to the r-process. Alternative examples such as ^{187}Rb and ^{147}Sm, are produced by a combination of s- and r-processes and are, therefore, difficult to analyze. The potential s-process chronometer ^{176}Lu has been shown to exhibit such a strong temperature sensitivity of the half life that it can not be used as a reliable clock [16].

Table 1.1: Long-lived nuclear chronometers.

Nucleus	Daughter	Decay mode	Half-life [yr]	Nucleosynthesis
^{232}Th	^{208}Pb	Decay chain	1.4×10^{10}	r - process
^{238}U	^{206}Pb	Decay chain	4.5×10^{9}	r - process
^{235}U	^{207}Pb	Decay chain	7.0×10^{8}	r - process
^{187}Re	^{187}Os	β^-	4.1×10^{10}	r - process

Th, U and Pu chronometers

The ^{232}Th/^{238}U, ^{235}U/^{238}U and ^{244}Pu/^{238}U abundance ratios represent the situation at the beginning of the Solar system and can be extrapolated back in time by means of their known half lives. The schematic exponential model that was originally used for the time dependence of production was presently replaced by a more realistic Galactic chemical evolution model [10]. A new way to look at the actinide chronometers is provided by accurate abundance determinations in ultra metal poor halo stars [17].

Th chronometers

Originally, an attempt of this chronometer was proposed by Butcher [18] using the relative abundances of Th and Nd at the surface of stars with various metallicities. The Th/Eu (r-process productions) abundance ratio [19] has been discussed as well. The determination of the age is reduced to the problem of mapping through a chemical evolution model.

Re/Os chronometer

This chronometer, the topic of this thesis will be discussed in detail in the next subsection.

1.2.4 Re/Os cosmochronometer

The nucleosynthesis of Os and Re represents an important alternative with respect to the actinide chronometers, which has attracted considerable attention in the past as well as at present. While ^{186}Os and ^{187}Os are synthesized only by the s process (they are "shielded" against r-process production by two stable isobars, see Fig. 1.5), an important fraction of the observed abundance of ^{187}Os is due to the slow β-decay of ^{187}Re ($t_{1/2}$ = 41.2 Gyr [20]). Clayton [21] proposed to use this decay to determine the time-duration of the Galactic nucleosynthesis, and hence, the age of the Universe (: the Re/Os clock).

For the analysis of the Re/Os clock, the essential nuclear data are the accurate neutron capture cross sections of ^{186,187}Os and the β-decay rate of ^{187}Re under stellar conditions. The latter information has been firmly estab-

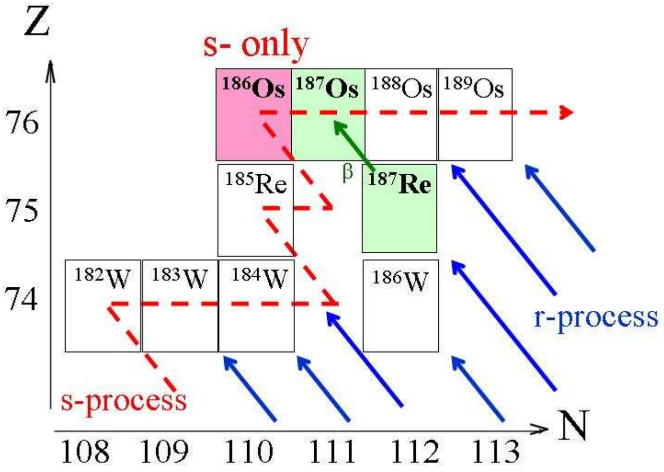

Figure 1.5: The nuclide chart in the W-Re-Os region. The s-process path is indicated by dashed lines. The r-process and β decay paths are indicated by the blue, green solid arrows, respectively. S-process branching points are in ^{185}W and ^{186}Re.

lished by a measurement of the ^{187}Re half-life for fully-stripped atoms [22]. In the present work, I will address the question of the neutron capture rates. In fact, in the classical s-process picture, the abundance ratio of this isotopic pair is directly related to the ratio of their neutron capture cross sections.

Stellar neutron capture rates are obtained by averaging the differential cross sections over a Maxwellian distribution of neutron energies (MACS). While experimental data refer necessarily to nuclei in their ground state the effect of thermally populated low-lying excited states has to be determined by means of theoretical calculations based on the Hauser-Feshbach statistical model theory (HFSM) [23]. The reliability of the latter part depends on an experimental determination of the parameters used in HFSM calculations. Among these parameters, average resonance properties such as mean level spacings $\langle D \rangle$, average radiative widths $\langle \Gamma_\gamma \rangle$, and neutron strength functions S are most important. This information can be derived from high resolution data for the respective neutron capture cross sections to establish a sound parametrization of the HFSM calculations.

Additional constraints for the HFSM calculations can be established from a measurement of the inelastic scattering cross section. This quantity provides information on the neutron transmission functions for excited nuclear levels. In fact, this additional study has been performed in a measurement of the inelastic cross section of ^{187}Os, for the first excited state of this nucleus [24].

From the astrophysical side, the analysis of the Re/Os clock has to be complemented by realistic chemical evolution models [25], but this aspect is beyond the scope of the this work.

In this thesis I report on the RRR analysis of the neutron capture cross sections of ^{186,187,188}Os, aiming at improving the nuclear data requirements for the Re/Os clock. For detailed discussions of the Re/Os clock see Chap. 5.

1.3 Neutron sources

Accurate neutron capture cross sections are essential for studies of s-process nucleosynthesis. These data are also required for the statistical model calculations that are needed to take the effect of thermally populated low lying excited states into account and to obtain the cross sections in the region of unstable nuclei, which can not be measured directly.

1.3.1 Spallation reaction source

Spallation reactions induced by energetic particle beams constitute one of the most interesting pulsed sources of fast neutrons suited for time of flight (TOF) measurements. The characteristics of the main spallation facilities are compared in Table 1.2. While LANSCE and noperation, the SNS at Oak Ridge started in 2006 [26] with emphasis on thermal or near thermal energies. JSNS is in the commissioning phase and had produced first neutrons on May 2008 [27].

Table 1.2: Characteristics of neutron spallation facilities.

Facility	n_TOF CERN	LANSCE LANL	SNS ORNL	JSNS JPARC
Accelerator	proton	proton	proton	proton
energy [GeV]	20	0.8	1	2
pulse width [ns]	6	125	700	1000
Target	Pb	W	Liquid Hg	Liquid Hg
Neutron				
energy (min)	0.1 eV	1 eV	0.1 eV	0.1 eV
(max)	800 MeV	100 keV	100 MeV	100 keV
average yield [10^{15}/s]	2	20	180	125
Flight path [m]	185	6 - 60	10 - 60	22 - 29

1.3.2 Photonuclear reaction source

High intensities can also be achieved via (γ, n) reactions by bombarding heavy metal targets with energetic electron beams from linear accelerators. The characteristics of the main facilities of this type are compared in Table 1.3.

Table 1.3: Characteristics of neutron photo-neutron facilities.

Facility @	GELINA IRMM	ORELA ORNL	n-ELBE FZ Dresden
Accelerator			
energy [MeV]	100	140	40
pulse [ns]	1	10	0.01
Target	U	Ta	Liquid Pb
Neutron			
energy (min)	10 eV	10 eV	20 keV
(max)	10 MeV	10 MeV	10 MeV
average yield [10^{13}/s]	3.4	14	2.7
Flight path [m]	8 - 400	9 - 200	3.9

1.3.3 New neutron source facility

Beside the photonuclear and spallation reaction for neutron generation, the possibility offered by the High intensity low Energy beam is opening a new and promising opportunity for novel neutron facilities. High intensity proton beam (with current higher than 1 mA) has been triggered by the ADS (Accelerator Driven System) and waste transmutation programs, in order to have the driven neutron source for the sub-critical reactors. Within this frame, high intensity RFQ (Radio Frequency Quadrupole) are under development around the world, but the more important one for the neutron production are located at Laboratori Nazionali di Legnaro (LNL, Legnaro, Italy) [28] and at the STERN-GERLACH-ZENTRUM in Frankfurt Am Main (Germany) [29]. The planed characteristics of these facilities are listed in Table 1.4. Using the low energy proton beam, a high quality neutron spectra can be obtained using the reaction $^{7}\mathrm{Li}(p,n)^{7}\mathrm{Be}$ which have a high yield even near the energy threshold (1.88 MeV) with a lowest neutron energy of about 1 keV.

The most important characteristic of such kind of facility is the high neutron flux at sample position with a good energy resolution. With such facilities will be possible to measure low mass sample never measured before. The low mass sample region is important for such isotopes that are too radioactive, rare elements or expensive one. Both the facility plan to construct targets by implanting RIB(Radioactive Ion Beam) species produced at GSI (for FRANZ) and at SPES (for LENOS). In addition, LENOS offers the unique opportunity to have the presence in situ of the neutron beam and the RIB beam, so it is planned to have the convergence of the two lines on the same target, allowing the implantation of the RIB isotopes and the neutron irradiation at the same time.

Table 1.4: Characteristics of neutron novel neutron facilities.

Facility	FRANZ	LENOS
@	Frankfurt	LNL
Accelerator	proton	proton
energy [MeV]	2	5
pulse [ns]	1	1
Target	^{7}Li	^{7}Li
Neutron		
energy (min)	1 keV	1 keV
(max)	0.5 MeV	2 MeV
average yield [10^{12}/s]	7	100
Flight path [m]	1	1

1.4 Neutron induced reactions

1.4.1 General features

The interaction between neutrons and nuclei can take place through many reaction channels. For neutron induced reactions, there are for example such a ${}^{A}_{Z}\mathrm{X}(n,n){}^{A}_{Z}\mathrm{X}$, ${}^{A}_{Z}\mathrm{X}(n,n){}^{A}_{Z}\mathrm{X}^{*}$, ${}^{A}_{Z}\mathrm{X}(n,\gamma){}^{A+1}_{Z}\mathrm{X}$, ${}^{A}_{Z}\mathrm{X}(n,p){}^{A}_{Z-1}\mathrm{Y}$, ${}^{A}_{Z}\mathrm{X}(n,d){}^{A-1}_{Z-1}\mathrm{Y}$, ${}^{A}_{Z}\mathrm{X}(n,t){}^{A-2}_{Z-1}\mathrm{Y}$, ${}^{A}_{Z}\mathrm{X}(n,\alpha){}^{A-2}_{Z-2}\mathrm{y}$ and so on. It is possible to observe elastic and inelastic channels; between inelastic channels we can mention the excitation of target nucleus, neutron capture, fission induced reactions, and many channels involving the presence of new particles in the exit channel of the reaction. Non-elastic reactions are commonly resumed in the absorption reaction [1].

More details will be given on neutron capture reaction (${}^{A}_{Z}\mathrm{X}(n,\gamma){}^{A+1}_{Z}\mathrm{X}$), in order to introduce the analysis performed in the following chapters of this thesis. Equation (1.4.1) and the sketch of Fig. 1.6 roughly resumes the neutron induced reaction channels.

---

[1] Inelastic neutron scattering (n,n') dose not included the absorption reaction occasionally.

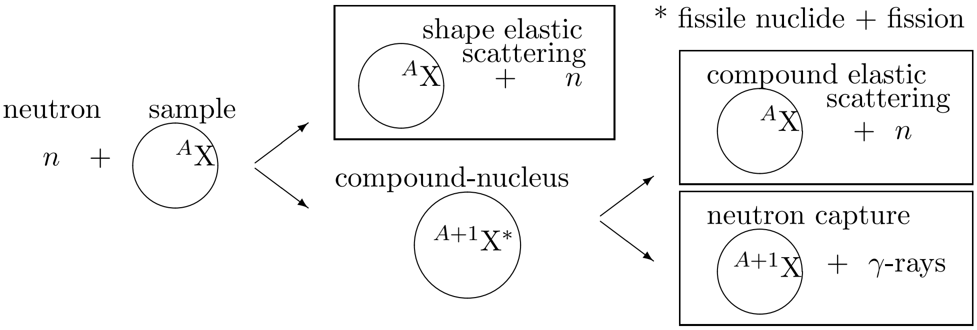

Figure 1.6: Sketch of neutron induced reactions at low energy.

$$\begin{aligned}
\sigma_{\text{total}} &= \sum_{\text{all-ch.}} \sigma = \sigma_{\text{shape-elastic}} + \sigma_{\text{reaction}} \\
&= \sigma_{\text{shape-elastic}} + \underbrace{\sigma_{\text{com-elastic}} + \sigma_{\text{inelastic}}}_{\sigma_{\text{reaction}}} \\
&= \underbrace{\sigma_{\text{shape-elastic}} + \sigma_{\text{com-elastic}}}_{\sigma_{\text{elastic}}} + \sigma_{\text{inelastic}} \\
&= \sigma_{\text{elastic}} + \underbrace{\sigma_{\text{com-inelastic}} + \sigma_{\text{direct}} + \sigma_{\text{pre-equilibrium}} + \sigma_{\text{fission}}}_{\sigma_{\text{inelastic}}}, \quad (1.4.1)
\end{aligned}$$

where 'com' is compound nucleus.

The energy of the incident neutron is a basic parameter for the reactions. Three energy ranges are usually defined :

- Epithermal ($E_n > E_n$(thermal)= 0.025 eV) and $E_n < 200$ keV
  At these energies elastic scattering (direct or through a compound nucleus formation), capture and fission are the main reaction channels, depending on the size of the target nucleus. The total cross-section can be evaluated in a geometrical way by the approximated formula $4\pi R^{'2}$, where $R^{'}$ is the scattering length ($\sim$ 10 fm for ^{186,187,188}Os).

- Fast neutron (200 keV $< E_n <$ 1 MeV)
  New reaction channels can be opened. Neutron inelastic scattering ($E_n > E_1$: first excited states of the target nucleus) and direct reaction, pre-equilibrium emissions take place. Typically elastic cross section is $\sim \pi R^{'2}$, the inelastic cross section is also $\sim \pi R^{'2}$ and total cross section can be approximated to $\sim 2\pi R^{'2}$.

- High energies ($E_n > 1$ MeV)
  Reactions induced by neutrons at these energies can give rise to the

> production of light charged particles in the exit channel: proton, deuterium, triton, α particles. The experimental data analyzed in this thesis come from incident neutron with energies up to 1 MeV.

In Fig. 1.7 partial cross sections calculated by TALYS [30] are shown.

1.4.2 Neutron capture

The absorption of the incident neutron produces a new excited compound nucleus. The excited compound nucleus decays emitting gamma-rays, with energies up to few keV. We can write this reaction $^{A}\mathrm{X} + n \rightarrow {}^{A+1}\mathrm{X}^{*} \rightarrow {}^{A+1}\mathrm{X}$ $+ \gamma$ or simply $^{A}\mathrm{X}$ $(n,\gamma)^{A+1}\mathrm{X}$. * means the excited state. The excitation energy E_c is given by the sum of the neutron separation energy S_n and of the incident neutron energy E_n, $E_c = S_n + E_n$. S_n is usually around 5 $\sim$ 8 MeV (6.3, 8.0, 5.9 MeV for ^{186,187,188}Os). The reactions of compound nucleus ($^{A+1}\mathrm{X}^{*}$) have the typical time scale $\sim 10^{-16}$ s, this is much longer than the time needed for the neutron to pass through the nucleus, which is the time scale of the direct reaction ($\sim 10^{-22}$ s). The life of the compound nucleus is $\hbar$ / Γ using Heisenberg's principle [2]. The compound nucleus decays with emission of γ-ray via bound states (E_i) until their ground state. In Fig. 1.8 the scheme is shown. At these high excitation energies for nuclei of medium and heavy mass the nuclear system is extremely complex and no nuclear model is capable of predicting the level position and other properties of these excited states. Cross sections can therefore only be accessed by measurements.

In the thermal neutron energy region, the reaction cross section is proportional to the $1/v$. Here v is the velocity of the neutron. At relatively low energy, cross sections are characterized by resonance structures. The resonances are well separated and the mean distance between them (the level spacing D, see Sec. 4.2) is large compared to their natural line width Γ and the instrumental resolution Δ_R, namely resolved resonance region (RRR) where $D > \Gamma$ and $D > \Delta_R$. With increasing energy, the level distance decreases and the total natural line width increases. Although at intermediate energies the resonance structure still exists, the resonance structure can no longer be resolved due to the limited instrumental resolution and broadening effects, that is to say un-resolved resonance region (URR) characterized by $D > \Gamma$ and $D < \Delta_R$. At higher energies resonance structure disappears ($D < \Gamma$), it is called the continuum region.

---

[2] Heisenberg's uncertainly relation can be written $\Delta E \Delta t \gtrsim \hbar$. Δt is approximated as the life τ and using $E = h\nu$, it becomes $h\Delta\nu \cdot \tau \gtrsim \hbar$. h$\Delta\nu$ can be called natural width Γ. Finally it is delivered $\tau \gtrsim \hbar/\Gamma$.

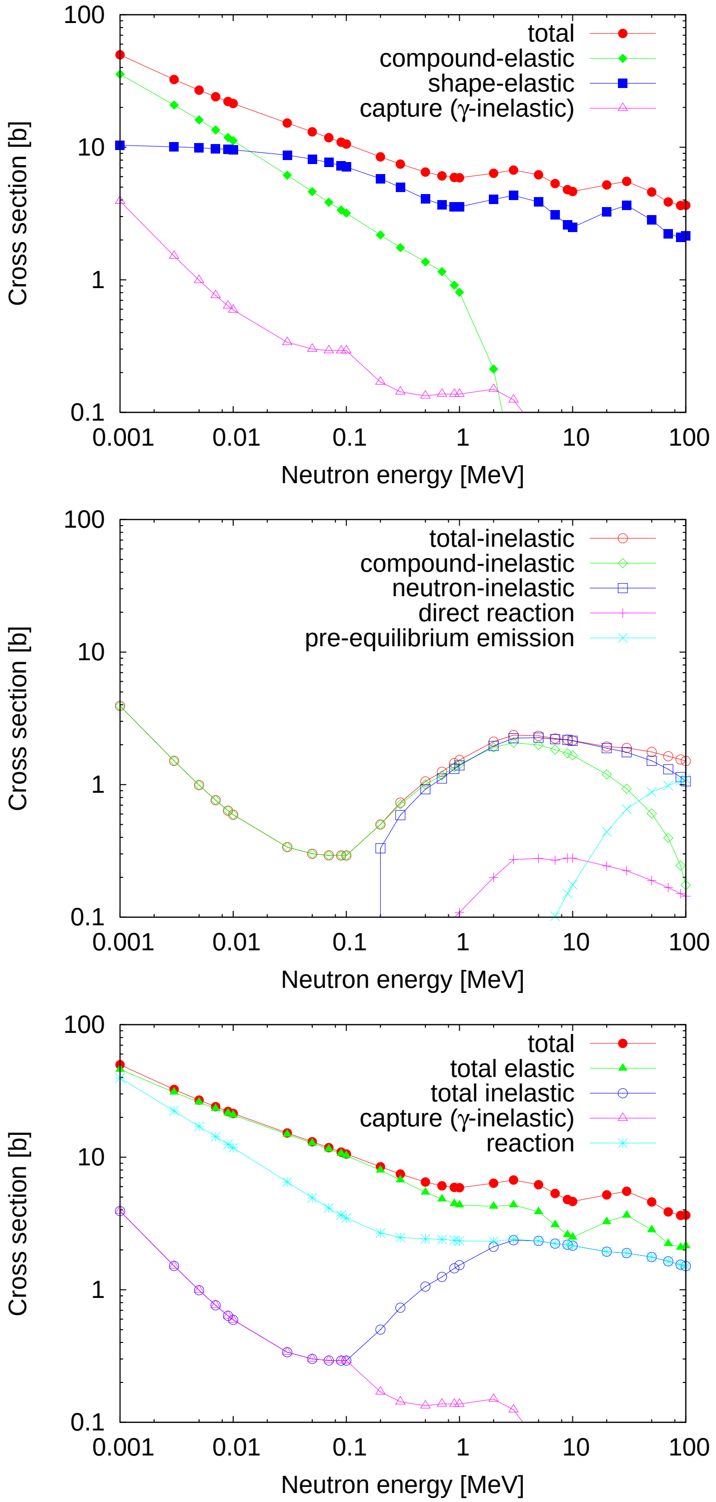

Figure 1.7: ^{186}Os partial cross sections calculated by TALYS.

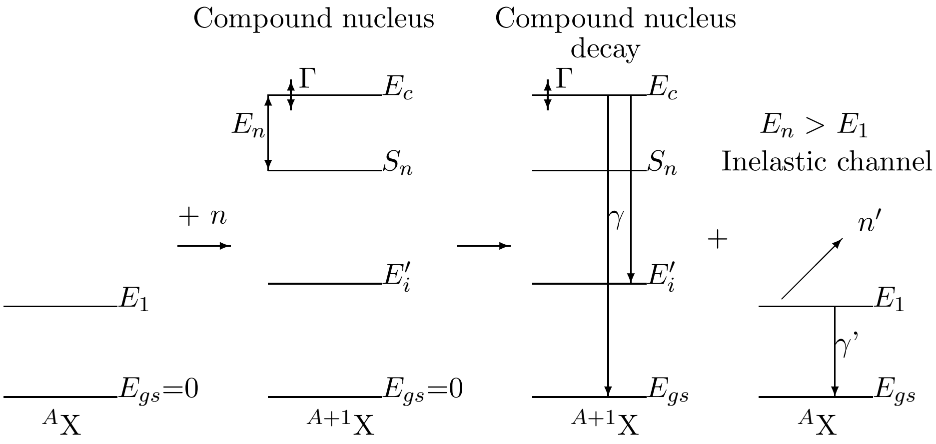

Figure 1.8: A scheme of the neutron capture reaction.

1.4.3 Resonance : Breit-Wigner formula

The capture cross section of a single isolated s-wave resonance has the following Breit-Wigner formula form with $E = S_n + E_n$:

$$\sigma_\gamma(n,\gamma) = \pi ƛ^2 g \frac{\Gamma_n \Gamma_\gamma}{(E - E_c)^2 + (\frac{\Gamma_n + \Gamma_\gamma}{2})^2}, \tag{1.4.2}$$

$ƛ$ is the reduced neutron wavelength. g is statistical weight factor (see Subsec. 1.4.5) and Γ is partial width which will be discussed in detail in the next sections.

Resonance area A is $C \times g\Gamma_n\Gamma_\gamma/(\Gamma_n + \Gamma_\gamma)$. C is the constant $2n\pi^2ƛ^2$ (where n is the sample thickness [atoms/barn]).
The simple approximation can deliver these relations,
$\Gamma_n \gg \Gamma_\gamma$, $\Gamma_{total} \approx \Gamma_n \Rightarrow A \approx ng\Gamma_\gamma$,
$\Gamma_\gamma \gg \Gamma_n$, $\Gamma_{total} \approx \Gamma_\gamma \Rightarrow A \approx ng\Gamma_n$.
On the other hand, the resonance shape is dominated by the larger partial width. These characters are very important for the resonance analysis.

1.4.4 Resonance : partial width

Statistically the fluctuations of the partial widths obey to the $\chi^2(\nu)$ distribution.

$$P(x) = \frac{e^{-x/2}x^{(\nu/2-1)}}{2^{\nu/2}\Gamma(\frac{\nu}{2})}, \qquad \text{here } \Gamma(z) = \int_0^\infty t^{(z-1)}e^{-t}dt. \tag{1.4.3}$$

ν is the number of degrees-of-freedom i.e. the number of the final states for the considered reaction.

1. Reduced neutron width

Reduced neutron width Γ_n^l is defined by using neutron width Γ_n

$$\Gamma_n^l = \Gamma_n \sqrt{E_0/E_n} V_l(E) \qquad : V_l = P_l/ka \tag{1.4.4}$$
$$V_0 = 1, \quad V_1 = k^2a^2/(1+k^2a^2), \quad V_2 = k^4a^4/(9+3k^2a^2+k^4a^4), ...$$

E_0 is an arbitrary energy, it is taken to be 1 eV usually. P_l is penetrability factor, l is orbital angular momentum (see Subsec. 1.4.5), k is wave number and a is channel radius. For single spin population, reduced neutron width distribution can be derived as $\nu = 1$, Gamma function $\Gamma(1/2) = \sqrt{\pi}$. The neutron partial width distribution is called Porter- Thomas distribution (see Sec. 4.4).

2. Radiative (γ, photon) width

There are many of primary γ transitions and a sum of these gives a radiative width. ν represents the number of exit channels or different radiative cascades. In ^{186,187,188}Os case ν could be $\sim 10^5$ (see Fig. 5.6). Increasing ν, the distribution of Eq. (1.4.3) approximates Gaussian distribution or δ function which has one peak, the mean value of this distribution is 1 and the variance is $2/\nu$. It could be assumed that the radiative (γ) width is a constant. At the high energy region, unresolved resonance region, the width is not constant any more which can be explained with theoretical models (see Subsec. 5.2.2).

1.4.5 Resonance : spin numbers

For the resonance analysis, it is needed to consider spin numbers. Resonance's orbital momentum assumptions are verified by means of statistical methods, $ESTIMA$ [31]. The $ESTIMA$ method is based on a probabilistic estimate of the 'l-wave character' of a nuclear level with a given reduced neutron width. A given state is considered with

$$\frac{g\Gamma_n}{\sqrt{E_n}} = g\Gamma_n^0 > F \times V_1 \langle g\Gamma_n^1 \rangle \ , \ V_1 = \left(1 + \frac{11369 \times 10^3}{E_n A^{2/3}}\right)^{-1} . \tag{1.4.5}$$

Here, E_n is the neutron energy of the level, and Γ_n is its neutron width. The averaged reduced neutron width for l=1 can be calculated with p-wave strength functions and p-wave level spacings. V_1 is the neutron penetrability factor for p-wave (see Subsec. 1.4.4-1), this is simply given with the neutron energy and A, mass number.

The case of F=10 sets **confident** s-wave. The probability that a nuclear level is s-wave is 99.8 %.

Table 1.5: Spin numbers for the present Os samples.

Symbol	Quantity	Present experimental case
i	spin of incident	1/2 (neutron).
l	orbital angular momentum	0 (s-wave).
I^{π}	target spin	0^+ (^{186,188}Os). $1/2^-$(^{187}Os).
$j = i + I$	channel spin	1/2 (^{186,188}Os). 0,1 (^{187}Os).
$J = j + l$	resonance spin	1/2 (^{186,188}Os). 0,1 (^{187}Os).
g	statistical weight	1 (^{186,188}Os). 1/4, 3/4 (^{187}Os).

The case of F=1 sets **likely** s-wave or can also be p-wave.
The plots of reduced neutron widths of our data sets are shown in Fig. 1.9. The data points are above the likely s-wave lines, practically points are above the confident s-wave. Thus the observed resonances can be assumed to be s-wave.

The resonance spin J is the vector sum $\mathbf{J} = \mathbf{I}+\mathbf{i}+\mathbf{l}$ (for the definitions see Table 1.5). Start with the possible combination of the channel spin $\mathbf{j} = \mathbf{I} + \mathbf{i}$ where the possible value of j are $|I - i| \leq j \leq I + i$ and combination channel spin j with the orbital momentum l, $J = j + l$ where the possible values of J are $|j - l| \leq J \leq j + l$. Statistical weight factor is $g = (2J + 1)/[(2s + 1)(2I + 1)]$.

Table 1.5 shows important contents and the values for this present analysis. The ^{186}Os and ^{188}Os levels belong to a single spin population for s-wave ($J = 1/2$). In the case of ^{187}Os, the ground-state spin is $I = 1/2$, therefore two values of the total angular momentum, $J = 0$ and $J = 1$, are possible for s-wave.

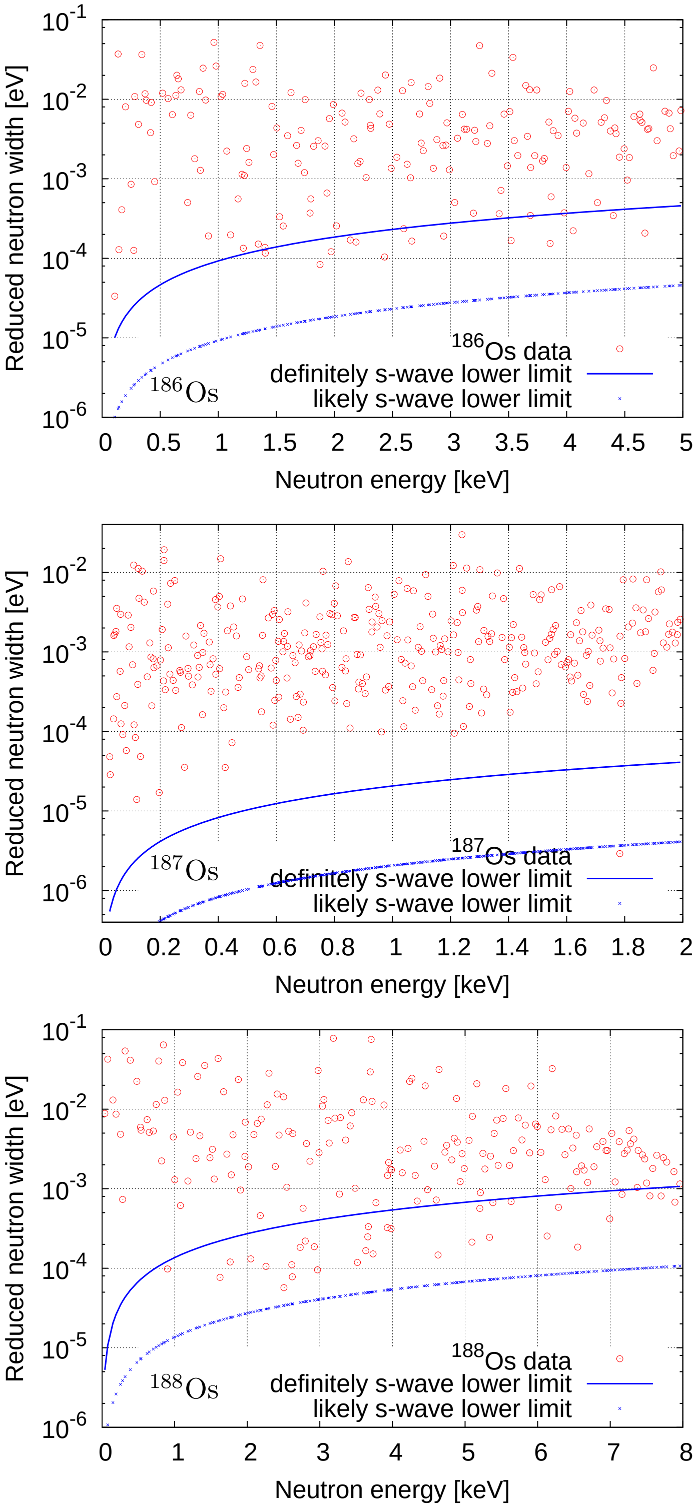

Figure 1.9: Reduced neutron width distributions and discrimination of the orbital momentum lines.

Chapter 2

Neutron capture measurements at the n_TOF facility

The n_TOF, **n**eutron **T**ime **O**f **F**light facility [32] is operating at CERN since 2000. After the commissioning phase which took place in 2000 and 2001, three measurements campaigns were performed in 2002, 2003 and 2004. A large number of samples is investigated covering studies on neutron capture reactions and neutron-induced fission. It was possible to face all the physical motivations mentioned in the introduction of this thesis. Most of the measurements have been performed within the framework defined by the n_TOF-ND-ADS (Nuclear Data for accelerator Driven System), an FP5 initiative of the European Commission on basic studies for the Partitioning and Transmutation (P&T) of nuclear wastes. These had a strong relevance in nuclear astrophysics in particular for studies on s-process nucleosynthesis. The present subject of this thesis, Os measurements were performed during the 2003 campaign.

As a further project, n_TOF Phase-2 was proposed. In November 2008, the preliminary phase of the commissioning of the new lead spallation target was successfully achieved. The full operation of the facility for 2009 is already scheduled.

2.1 The n_TOF facility

The measurements have been performed using the n_TOF pulsed neutron beam. The general n_TOF experimental layout is presented in Fig. 2.1. At n_TOF, neutrons are generated by spallation reactions induced by the 20 GeV protons beam of the CERN PS accelerator complex impinging on a massive lead target [33]. The low repetition frequency of the proton beam driver, the ex-

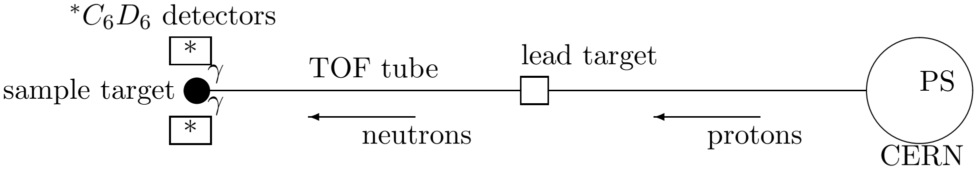

Figure 2.1: Sketch of the n_TOF capture experimental layout.

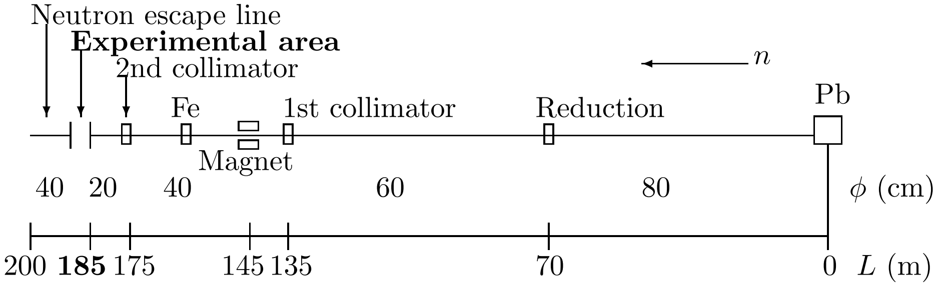

Figure 2.2: Scheme of the n_TOF tube : ϕ is the diameter of the tube. L is the distance from the lead target.

tremely high instantaneous neutron flux, the low background conditions in the experimental area, together with improvements of the neutron sensitivity of the capture detectors make this facility unique for neutron induced reaction cross section measurements, with much improved accuracy [34]. The generated neutrons are slowed down in the lead spallation target and moderated in the surrounding cooling water. An evacuated flight path with collimators at 135 and 175 m leads to the measuring station at a distance of 185 m from the spallation target. The available neutron energy in the experimental area runs from 1 eV up to 250 MeV with a nearly $1/E$ isolethargic fluence (i.e., $\phi(E) \propto 1/E$) up to 1 MeV. The neutron beam line extends for additional 12 m beyond the experimental area to minimize the background from back-scattered neutrons. Background due to fast charged particles is suppressed by a 1.5 T sweeping magnet, heavy concrete walls, and a 3.5 m thick iron shielding [34]. The TOF tube's sketch is shown in Fig. 2.2. The main parameters of n_TOF are listed in Table 2.1.

2.1.1 Neutron beam properties at n_TOF

In the time-of flight measurements, the kinetic energy of low energy region neutrons can be deduced by means of the classical formula,

$$E_n = \frac{1}{2} \times \frac{M_n}{c^2} \frac{L^2}{(t+t_0)^2} = \left(\frac{72.2977L}{t+t_0} \right)^2 , \qquad (2.1.1)$$

where M_n is the neutron rest mass (in eV), c is the speed of light in vacuum (in m/s), L is the flight-path (in m) and t is the time of flight of neutrons

Table 2.1: Characteristics of the n_TOF facility.

Proton beam momentum	20 [GeV/c]
Intensity (dedicated mode)	7×10^{12} [protons/pulse]
Repetition frequency	1 [pulse] / 2.4 [s]
Protons pulse width	6 [ns] (rms)
Lead target dimensions	$80 \times 80 \times 60$ [cm^3]
Neutrons / protons	300 (0.1 eV $\sim$ 250 MeV)
Resolution in neutron energy	$\Delta E/E = 10^{-4}$ (1 eV $\sim$ 30 keV)
	$\Delta E/E = 10^{-3}$ (30 keV $\sim$ 10 MeV)

(in μs). This expression is the same when E_n is given in MeV and t is given in ns. The neutron energy is calculated taking into account the time spent in the moderator by produced neutrons [35], the flight path can be taken as 185.2 m.

The neutron flux per one bunch is shown in Fig. 2.3. From 1 eV to 10 keV of the neutron energy, the neutron flux is quite flat in lethargic units (dN/dln$E$), approximate 1.5×10^4 [n/pulse/cm^2].

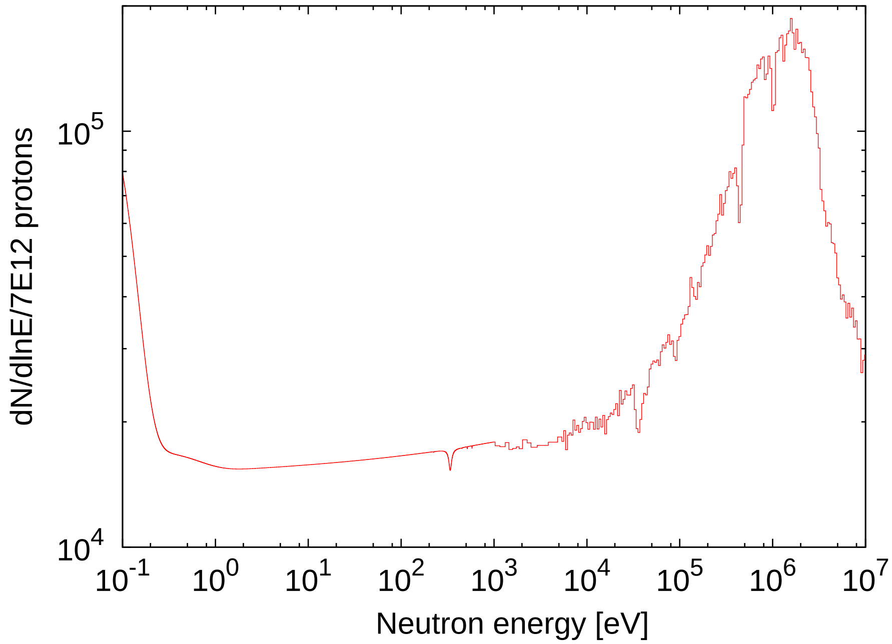

Figure 2.3: n_TOF neutron flux in the experimental area.

2.2 Experimental set-up

2.2.1 The detectors

The measurement is based on the detection of the γ-rays emitted in the deexcitation cascade following a neutron capture event. Two γ-rays detectors, consisting of C_6D_6 liquid scintillator (the composition is 0.5 % of ${}^{1}_{1}$H, 49.5 % of Deutrium ${}^{2}_{1}$H and 50.0 % of ${}^{12}_{6}$C), with minimized neutron sensitivity [36], were placed perpendicular to the neutron beam at a distance of about 3 cm from the beam axis. The background due to in-beam γ- rays [34] is strongly reduced by placing the detectors 9.2 cm upstream of the sample position. The calibrated neutron time of flight was used to determine the neutron energy.

The relative neutron flux was measured upstream of the capture samples with a low mass flux monitor consisting of a Mylar foil 1.5 μm thick with a layer of 200 μg/cm^2 of ^{6}Li surrounded by four Silicon detectors outside the neutron beam, measuring the charged particles of the ^{6}Li$(n,\alpha)^3$H reaction [37]. The stability of the experimental set-up and the neutron beam was periodically checked.

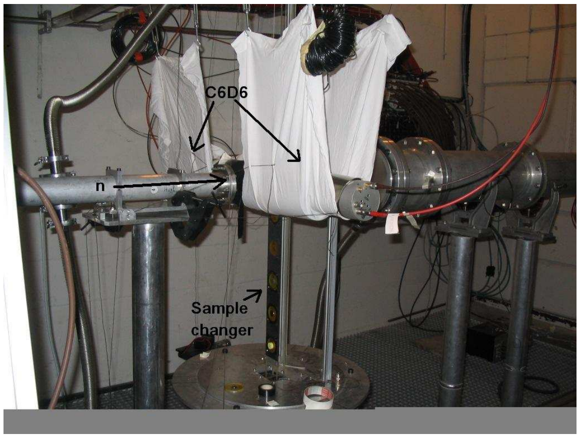

Figure 2.4: View of the n_TOF experimental area for the capture measurement.

2.2.2 Os samples

The sample powder was encapsulated in 0.1 mm thick aluminum cans 15 mm in diameter. The isotopic composition of the enriched metallic powder is listed in Table 2.2. The geometric characteristics of the Os samples are summarized in Table 2.3. Additionally samples of ^{197}Au, $^{\mathrm{nat}}$C, and $^{\mathrm{nat}}$Pb were used for the flux normalization and sample induced background measurements.

Table 2.2: Isotopic compositions of Os samples.

Sample	Isotopic composition [%]					
	^{186}Os	^{187}Os	^{188}Os	^{189}Os	^{190}Os	^{192}Os
^{186}Os	**78.48**	0.91	4.88	4.29	5.09	5.32
^{187}Os	1.06	**70.43**	12.73	5.13	5.42	5.21
^{188}Os	0.11	0.12	**94.99**	2.55	1.27	0.97

Table 2.3: Characteristics of Os samples.

Sample	Mass [g]	Diameter [mm]	Calculated thickness [mm]	Thickness [atoms/b]
^{186}Os	1.9999	15	0.5189	3.714×10^{-3}
^{187}Os	1.9212	15	0.4958	3.549×10^{-3}
^{188}Os	1.9967	15	0.5126	3.669×10^{-3}

2.3 Data analysis

2.3.1 Energy calibration

The energy calibration of the C_6D_6 detectors was done using three different γ-ray sources : ^{137}Cs : (E_γ = 662 keV), ^{60}Co : (1.173, 1.332 MeV), Pu/C(^{13}C$(\alpha, n)^{16}$O) : (6.23 MeV). The obtained spectra are shown in Fig. 2.5. It has been verified that the used detectors show a linear relation between deposited γ-rays and amplitudes of the pulses. The measured pulse height spectra were fitted with the simulated energy deposition. The calibrations performed during the measurements confirmed the gain stability of the detectors.

2.3.2 Pulse height weighting technique

The efficiency ε for detecting the capture event depends in a complex way on the emitted γ-ray spectrum when using a low efficiency detector like C_6D_6 detectors. The γ-ray spectrum is different for each isotope. For a given isotope, it differs from one resonance to another. The neutron capture event is characterized by the de-excitation of the compound nucleus by emission of one or more γ-rays.

To circumvent these problems it is preferable to have the detection efficiency proportional to the γ-ray energy E_γ and a detection efficiency low enough to detect at most one γ-ray of the cascade. In that case, the efficiency for the cascade can be shown to be proportional to the total γ energy related in the capture event $\varepsilon_\gamma = kE_c$ with proportionality k, and it is therefore independent from the details of the γ decay path.

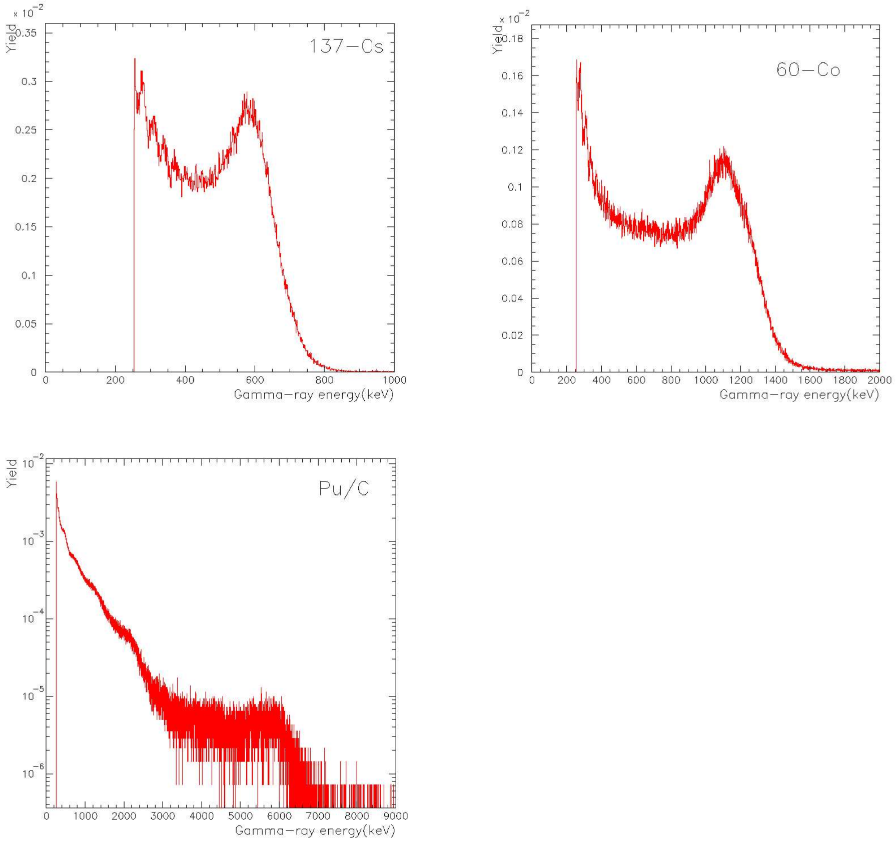

Figure 2.5: Energy calibration spectra of C_6D_6. Yields are normalized to the total area.

The energy deposited in the detector E_d is in general not proportional to E_γ but this can be introduced artificially by modifying the response function using a weighting function $W(E_d)$.

This method is know as the pulse height weighting technique (PHWT) [38]. The weighting functions for the various samples have been calculated on the basis of Monte Carlo simulations of the detector response [39, 40].

2.3.3 Capture yield

The capture yield $\mathbf{Y}(\mathbf{E_n})$, the fraction of the neutron flux $\Phi(E_n)$ with energy E_n incident on the sample that leads to a capture event, can be written as

$$Y(E_n) = N\frac{\int R(E_d)W(E_d)\mathrm{dE_d}}{\Phi(E_n)E_c}, \tag{2.3.1}$$

where $R(E_d)$ is the measured count rate. The fraction N of the flux that actually impinges on the samples must be determined by the gold standard sample which has the same diameter and measured in the same position. The resonance parameters of the gold (^{197}Au) saturated resonance at 4.9 eV are used to define the normalization constant.

This capture yield is linked to the total cross section σ_T and capture cross section σ_γ by the following expression,

$$Y(E_n) = \Big\{1 - \exp\big[-n\sigma_T(E_n)\big]\Big\}\frac{\sigma_\gamma(E_n)}{\sigma_T(E_n)}, \tag{2.3.2}$$

n is the number of atoms per barn called sample thickness. We can simplify Eq. (2.3.2) in two extreme cases

(1). $n\sigma_T \gg 1 \dashrightarrow Y \cong \sigma_\gamma/\sigma_n$ (generally thick sample),

(2). $n\sigma_T \ll 1 \dashrightarrow Y \cong n\sigma_\gamma$ (generally thin sample).

2.3.4 Background

The total background level is determined by combining the contribution of, (A) the ambient background, (B) scattering of in-beam γ-rays, and (C) capture of sample scattered neutrons in or near the scintillators. The (A) component can be determined by means of an empty position or by using an empty sample container. The (B) background source is investigated by using a Lead sample, which has negligible capture cross section. The (C) component is estimated by Carbon sample which has large neutron scattering cross section and small capture cross section. Background levels in comparison with the total count rate of the showed sample are shown in Fig. 2.6.

2.3.5 Beam stability

The silicon monitors work on the detection of α and tritium nuclei coming from the n + ^{6}Li reaction. One spectrum of the detector output is shown in Fig. 2.7 (a). In particular the yield of detected tritium is compared with the number of protons hitting on the Pb spallation target. A good linear correspondence between proton numbers and the integral area of detected tritium is shown in Fig. 2.7 (b), so neutron beam stability is well tested.

2.3.6 Os capture yields

The capture yields were obtained after a complete evaluation of the background and normalization. The cross sections and the resonance parameters were extracted from the analysis of the background-subtracted yields.

Os sample's yields obtained by n_TOF measurements are shown in Fig. 2.8

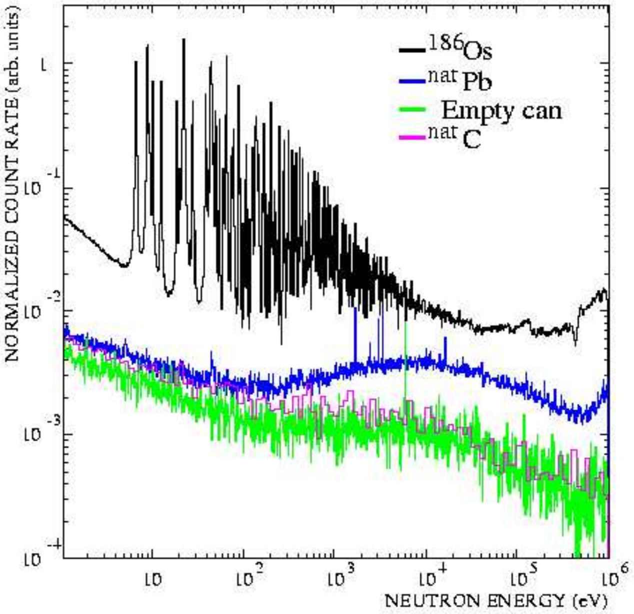

Figure 2.6: The ^{186}Os yield compared to other samples for the evaluation of background components [41] (see text).

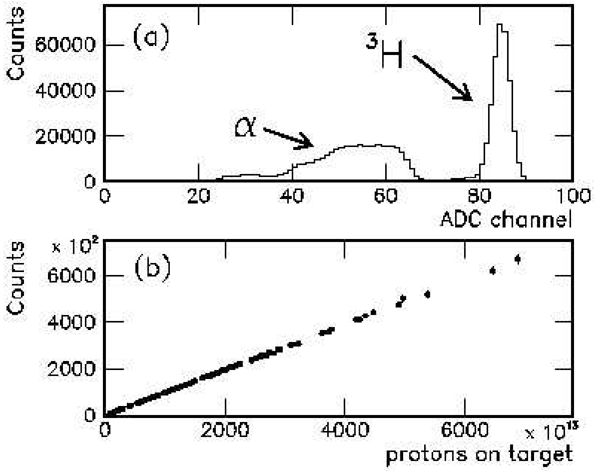

Figure 2.7: (a): An output spectrum of silicon monitors. (b): The numbers of protons on the spallation target versus the area of tritium.

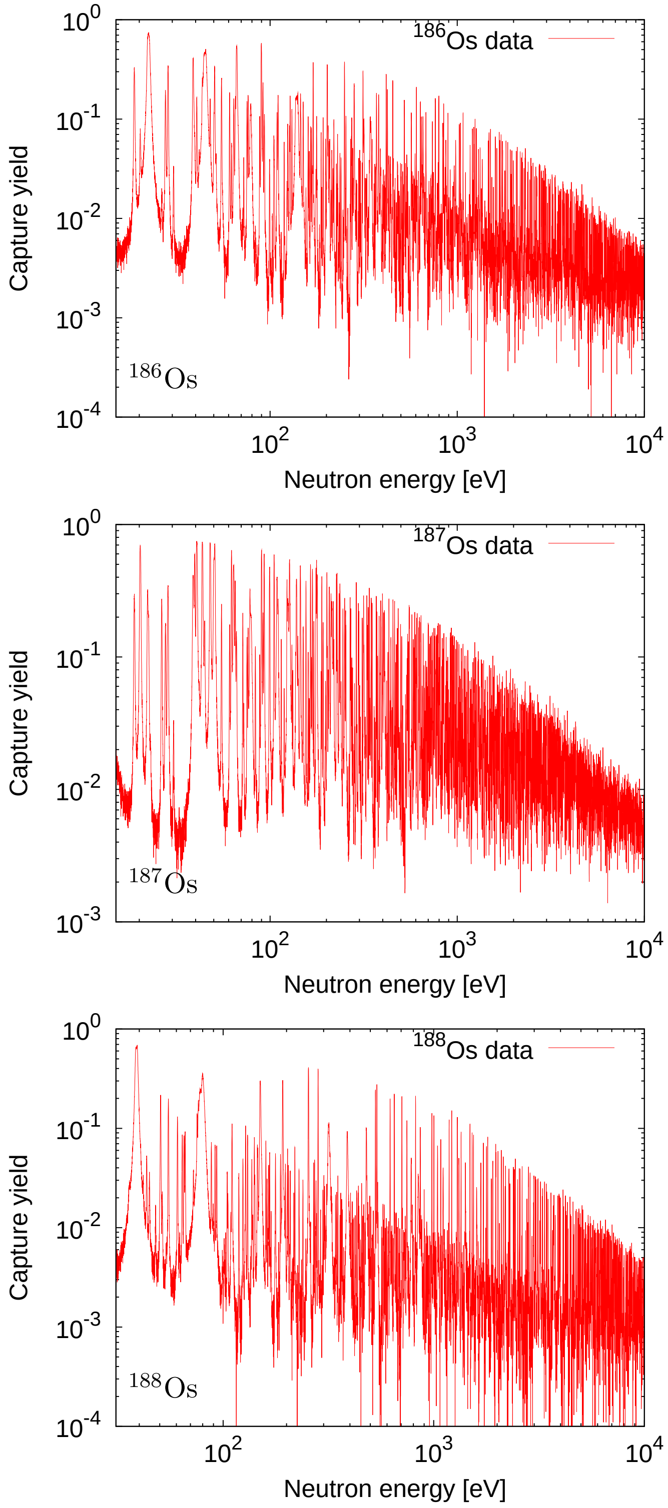

Figure 2.8: Os sample's capture yields subtracted background.

Chapter 3

Resonance parameter analysis

The resonance parameters have been extracted for ^{186}Os up to 5.0 keV, for ^{187}Os up to 3.0 keV, and for ^{188}Os up to 8.0 keV.

3.1 Resonance fit technique

In the resolved resonance region the experimental data can be classified in terms of resonance parameters, the resonance energy (E), the partial reaction width (e.g. the neutron width Γ_n, the capture (γ) width Γ_γ) and spin numbers. These parameters can be extracted from experimental data using resonance shape analysis codes such as SAMMY [42] and REFIT [43]. These codes are based on the multi-level R-matrix reaction theory. The Reich-Moore approximation (see Appendix C) is the preferred method for most modern evaluations. The present analysis was performed with SAMMY.

The following corrections for experimental conditions are included.

1. Doppler broadening

Individual nuclei within the sample are not at rest. The thermal motion of the emitting or absorbing atoms causes the Doppler broadening of the capture yield. The default of SAMMY is based on the free-gas model approximation. The broadening width is proportional to the root square of the effective temperature. Simply we can have ideas that at the low temperature, the resonance width is sharp and on the contrary at the higher temperature, the resonance width becomes wider.

2. Resolution broadening

Finite time intervals are required both for the neutron beam and for the detecting apparatus. The length of a neutron flight path depends on its position of origin within the neutron-producing target, on its position of interaction within the sample and on the position at which it is detected. The specific experimental sites or setups give their characteristic broadenings.

For the details of the n_TOF resolution function see Appendix D.

3. Self shielding

The finite size of the sample causes interactions beyond those described by the cross section for individual nuclei. Neutron absorption within the sample, the interactions of incident neutrons with other nuclei in front of the current position reduce the observed capture cross sections.

4. Multiple – scattering

Neutrons from the beam are scattered by target atoms before being captured, so the energy of the captured neutrons can be different. Besides the scattering correction is the increase in the observed capture cross section due to capture of neutrons scattered out from the original beam path. Not only single but also two or more (multiple) scatterings need to be considered. Its calculation is complicated because it involves the product of several probabilities such as reaching a position inside the sample, scattering from that position into the solid angle, scattered nuclei that reach a position and then captured at that location. The SAMMY approximation assumes that neutrons are uniformly distributed after two scatterings, both in direction of motion and in position within the sample.

3.2 Os data resonance fit

3.2.1 Radiative (γ) width (Γ_γ)

The information on the neutron width Γ_n has been taken from transmission measurements (Os data can find in [44, 45]). The analysis of the present data allowed for a fine determination of the radiative width (Γ_γ) and of the resonance energies (E_n). For resonances which have neutron width (Γ_n) larger than the radiative width, the neutron width was fixed and the radiative width was evaluated by SAMMY. I extracted a mean value ($\langle\Gamma_\gamma\rangle$) for the radiative width from these resonances (where $\Gamma_n \gg \Gamma_\gamma$), then I used this mean value ($\langle\Gamma_\gamma\rangle$) in all cases presenting small Γ_n width. The evaluated average radiative widths $\langle\Gamma_\gamma\rangle$ with their uncertainties (statistical) are shown in Table 4.5.

3.2.2 Os resonance plots and parameters

Illustrative examples of the SAMMY fit are shown in Fig. 3.1. The whole analyzed regions of ^{186,187,188}Os data are shown in Fig. 3.2, 3.3 and 3.4. Fits were done including the parameters of contaminant such a ^{189}Os.

The data sets of resonance parameters are listed in Appendix E.

Since the first resonances of ^{186}Os and ^{187}Os could not be fitted, the widths are left blank in the table. This fact is probably due to inhomogeneities in the sample. Os samples are made of powders therefore it is possible that the sample surfaces are not flat properly, in other words the

sample thickness could not be uniform. The inhomogeneity sample would make resonance shapes strange especially to strong (large) resonances. The simulation about this effect on the sample inhomogeneities on transmission data has been already performed [46]. For this effect, the important factor is the thickness compared to the grain-size of the sample powder. In Os sample's case the thicknesses are rather larger 0.5 mm, therefore effects of the inhomogeneities can take place if the average grain size is large ($\gtrsim$ 0.02 $\sim$ 0.05 mm) [47]. ^{186}Os, ^{187}Os sample grain sizes are $\sim$ 0.2 - 0.5 mm and $\sim$ 0.1 mm respectively. The ^{188}Os case is less impure and the small grain size could cancel this effect. (For the sample information see Subsec. 2.2.2.)
Inhomogeneities effects are not treated in the present version of SAMMY that I used. The released REFIT has the possibility to define the relative width of a Gaussian distribution. This model works well if the sample inhomogeneities is not too large. The latest version of SAMMY will include this effect but will be released only in January 2009.

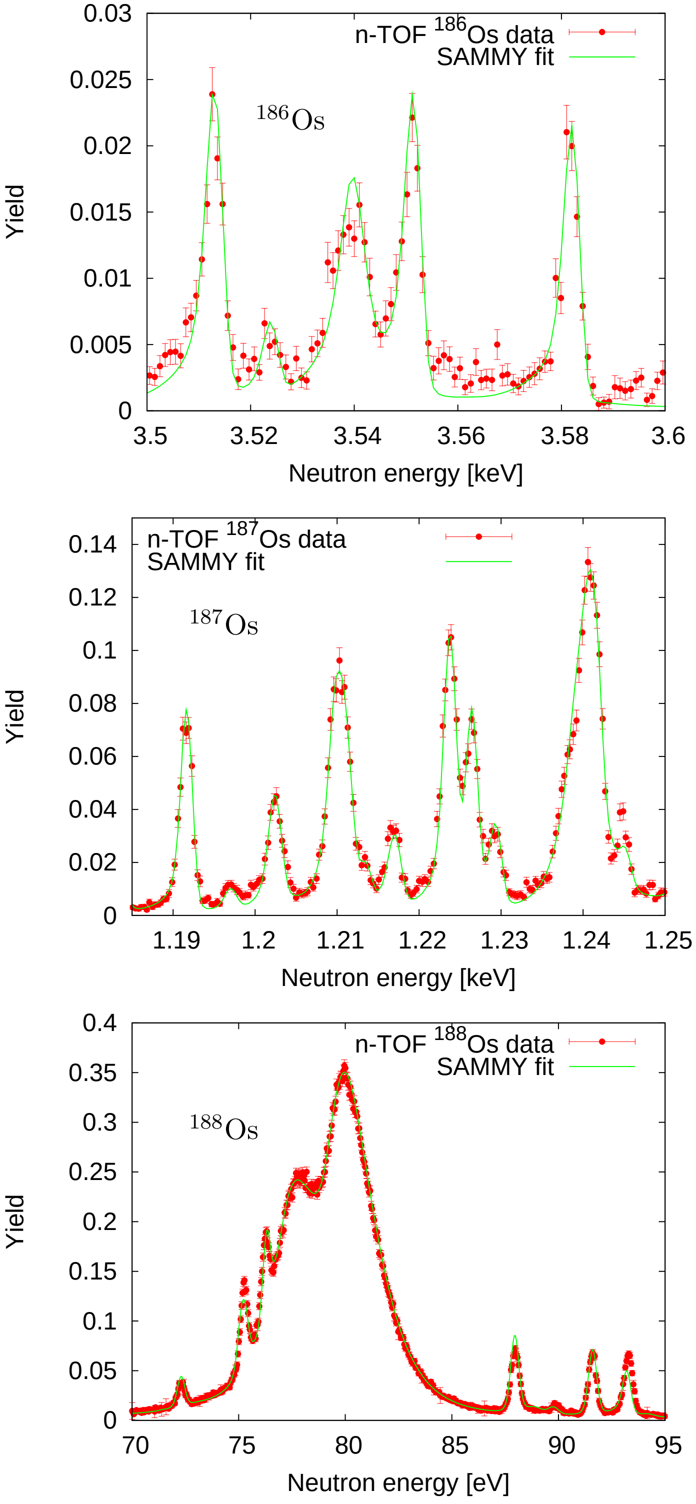

Figure 3.1: Zoomed SAMMY fits of ^{186,187,188}Os data

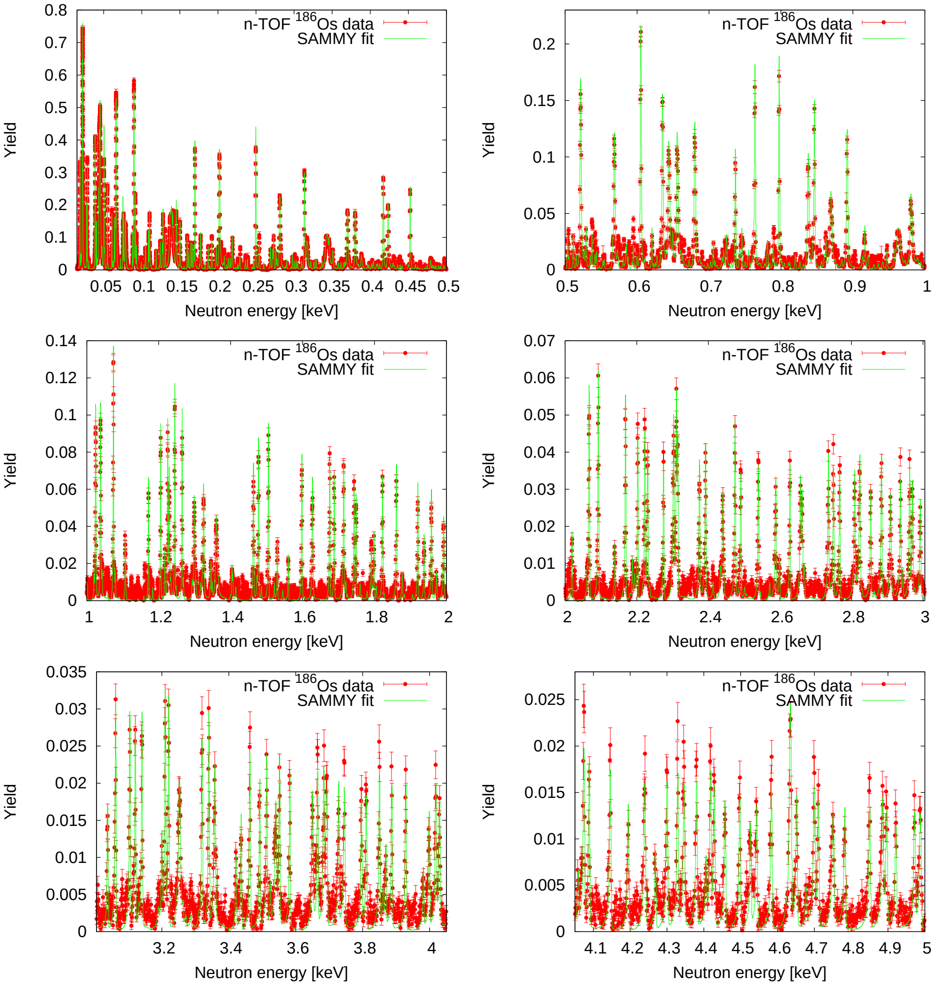

Figure 3.2: SAMMY fits of n_TOF ^{186}Os data

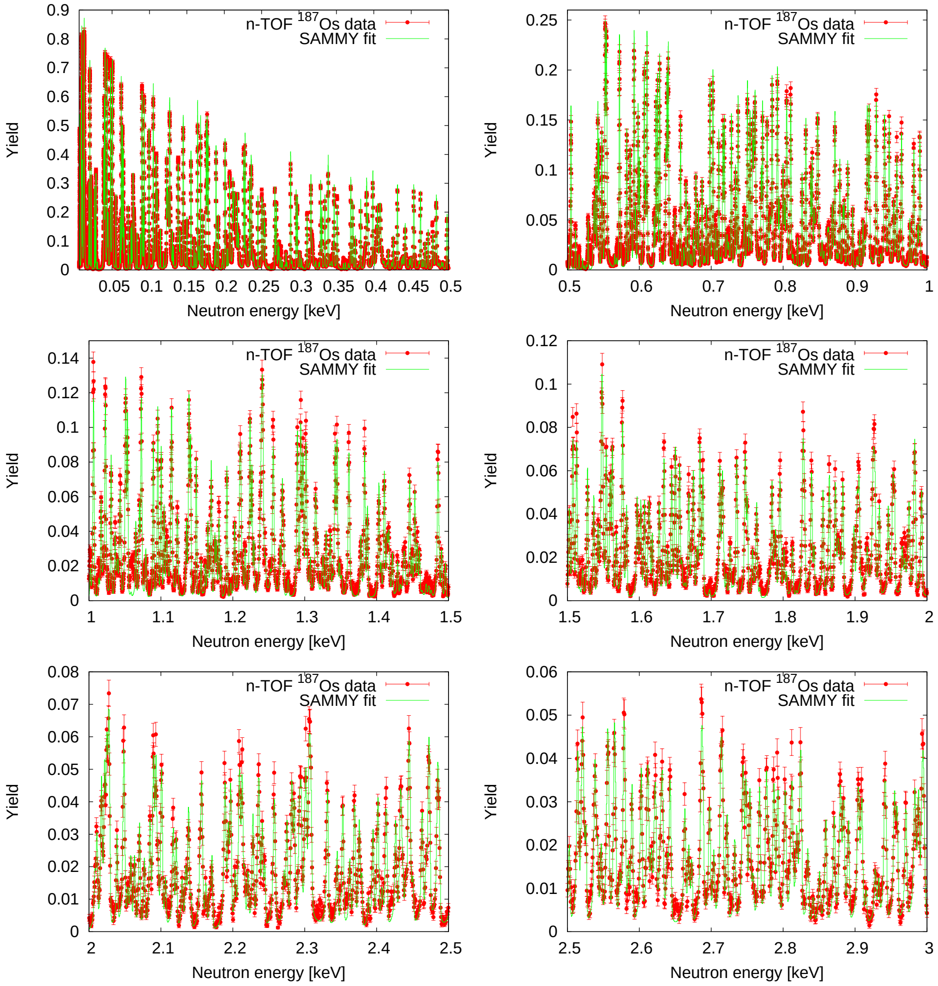

Figure 3.3: SAMMY fits of n_TOF ^{187}Os data

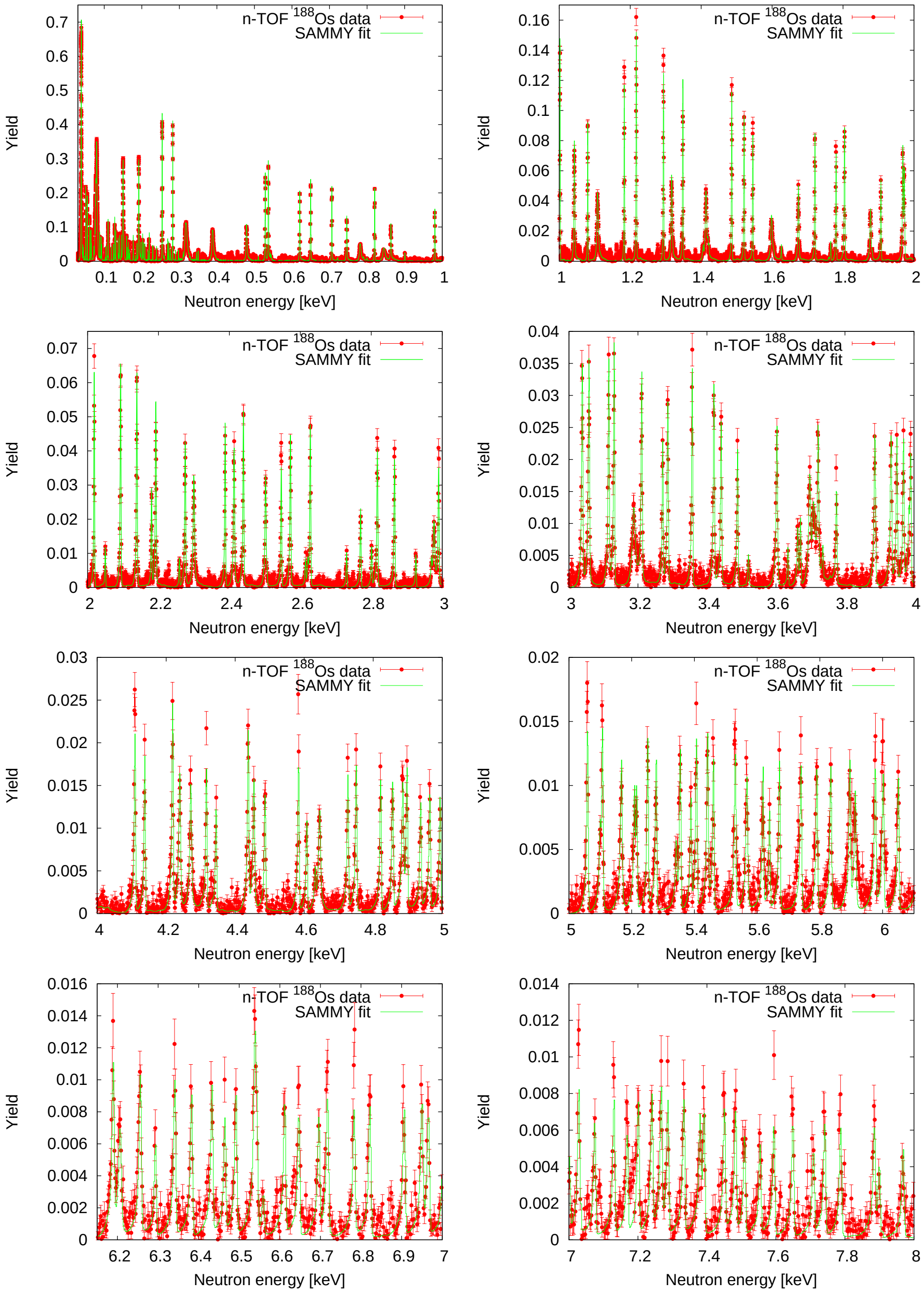

Figure 3.4: SAMMY fits of n_TOF ^{188}Os data

Chapter 4

Statistical analysis and average parameters

Once the study of a single resonance has been completed a statistical analysis of the whole set (E_n, Γ_γ, Γ_n) of obtained data is a very useful tool to investigate nuclear properties.

Besides the required parameters for statistical model calculations, average level spacing $\langle D_l \rangle$, average radiative (γ) width $\langle \Gamma_\gamma \rangle$ and neutron strength function S_l are estimated with the parameter sets obtained from the analysis of RRR. Here these parameters are discussed for $l = 0$, s-wave. It is used the accurate data up to 3.4 keV, 2.0 keV and 5.0 keV for ^{186,187,188}Os respectively (see Table 4.1). Several methods have been used for these estimates as described in the following.

Table 4.1: Os resonance numbers for each analysis (the maximum E_n in keV).

	Parameter analysis	Statistical analysis of levels	of widths
^{186}Os	186 (5.0)	126 (3.4)	122 (3.4)
^{187}Os	480 (3.0)	179 (1.0)	327 (2.0)
^{188}Os	199 (8.0)	125 (5.0)	125 (5.0)

4.1 Nearest-neighbor spacing distribution (NNSD)

A set of N resonance energy levels can be written as E_1, E_2, ..., E_N eV, where the level spacing between consecutive resonance energies ($E_{k+1} - E_k$) is set as s_k. The average level spacing for s-wave is $\langle D_0 \rangle$ (see Sec. 4.2). Histograms of the nearest-neighbor spacing (the unit of the averaged level spacing) for each spectrum in comparison with theoretical distribution models are shown in Fig. 4.1.

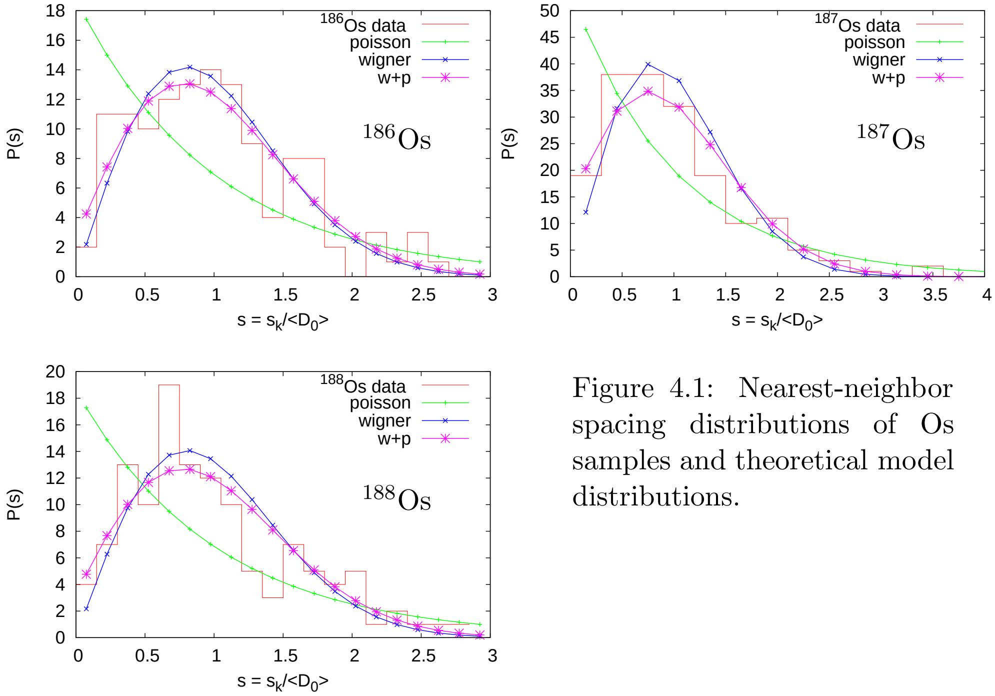

Figure 4.1: Nearest-neighbor spacing distributions of Os samples and theoretical model distributions.

The Poisson and Wigner distributions of $s(\equiv s_k \;/\langle D\rangle)$,

$$P_{\text{Poisson}}(s) = \mathrm{e}^{-s}, \tag{4.1.1}$$

$$P_{\text{Wigner}}(s) = \frac{\pi s}{2}\mathrm{e}^{-\frac{\pi s^2}{4}}, \tag{4.1.2}$$

show the two extreme cases. Poisson distribution is integrable system where the levels are uncorrelated (regular region). On the other hand Wigner distribution is chaotic for the non-integrable system where a repulsion between levels exists. It was surmised from the behavior of the eigenvalues of a symmetric matrix with random Gaussian distributed elements. Later on this has been known as the Gaussian orthogonal ensembles (GOE) of Random Matrix Theory and studied widely [48]. This chaotic quantum systems matched with good approximation experimental data. It is considered that real system is mixed system of regular and chaotic systems. Several forms have been proposed. One of them is the Berry-Robnik (BR) distribution [49],

$$P_{\text{BR}}(s) = \left[(1-q)^2\mathrm{erfc}\Big(\frac{\sqrt{\pi}}{2}qs\Big) + \Big(2q(1-q) + \frac{\pi}{2}q^3 s\Big)\mathrm{e}^{-\frac{\pi}{4}q^2s^2}\right]\mathrm{e}^{-(1-q)s},$$

$$\mathrm{erfc}(z) = \frac{2}{\sqrt{\pi}}\int_z^\infty \mathrm{e}^{-t^2}dt\ . \tag{4.1.3}$$

Where q is the fraction density of the phase-space. This distribution takes the form of Poisson for $q = 0$ the form of Wigner for $q = 1$.

As expected, the Wigner distributions give the good representations of the experimental data. It has to be noted that in the case of ^{187}Os two spin populations are combined. Therefore an increase small level spacings is expected, that is observed in Fig. 4.1.

4.2 Average level spacing

The average level spacing is defined as the average distance in the energy between following resonances. The three major methods to estimate the average level spacing are discussed below. Here E_i is the neutron energy of the resonance i and N is the total number of analyzed resonances.

4.2.1 Arithmetic (level set) method

This is very simple way, the average level spacing can be obtained by the ratio between the whole energy range and the number of resonances. This can be written as

$$\langle D_l \rangle_1 = \frac{(E_N - E_1)}{(N-1)}. \tag{4.2.1}$$

The uncertainty on $\langle D_l \rangle$ from the Wigner distribution is given by $\Delta \langle D_l \rangle = \langle D_l \rangle \times ((4-\pi)/\pi N)^{1/2}$ [44].

4.2.2 Best linear fit (BLF) method

The cumulative sums of numbers of resonances as a function of the neutron energy (so called staircase plot) are very popular ways to study level populations and missing levels. From the inverse slope of a least square straight-line fits ($N(E) = AE + B$) up to the neutron highest energy, s-wave average level spacings $\langle \mathrm{D}_0 \rangle$ are obtained. S.D. is standard deviation.

$$\langle D_l \rangle_2 = \frac{1}{A} \quad , \quad \text{S.D.} = \langle D_l \rangle \times \sqrt{\frac{\sum_{i=1}^{N} (N(E_i) - (AE_i + B))^2}{N}}. \tag{4.2.2}$$

Staircase plots of Os data sets and best linear fits are shown in Fig. 4.2. $N(E)$ is the corresponding cumulative number of energy levels as a function of energy.

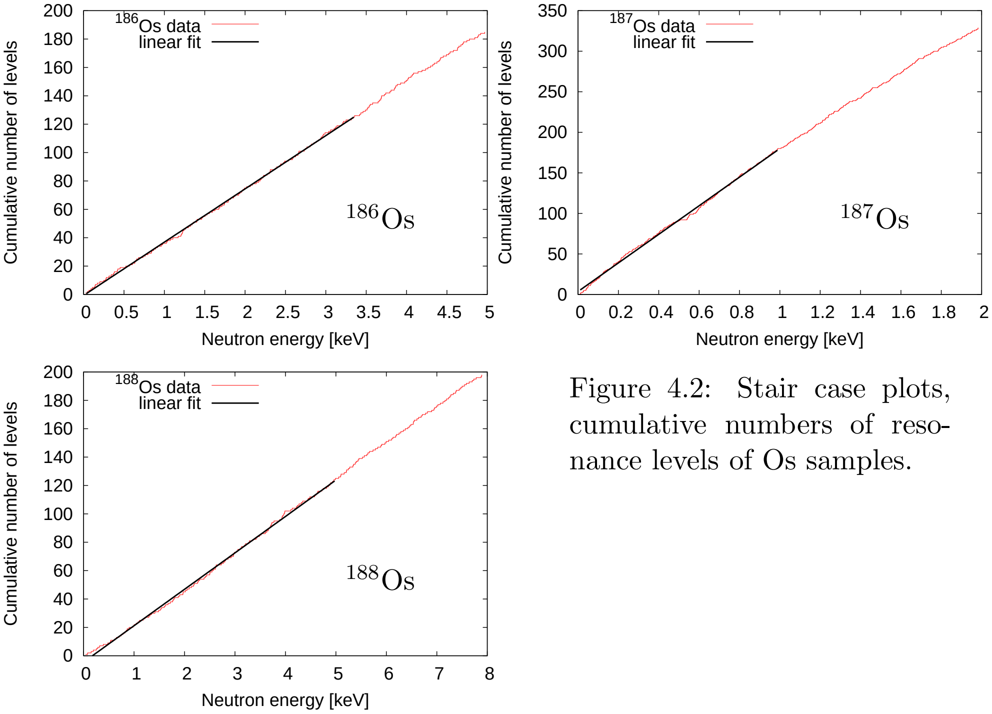

Figure 4.2: Stair case plots, cumulative numbers of resonance levels of Os samples.

4.2.3 Maximum-likelihood (ML) method

$\langle \mathrm{D}_0 \rangle$ can also be obtained using a maximum-likelihood estimate assuming a Wigner distribution for the level spacing.

$$\langle D_l \rangle_3 = \sqrt{\frac{\pi}{4N} \sum_{i=1}^{N-1} (E_{i+1} - E_i)^2} \ , \qquad \mathrm{S.D.} = \sqrt{0.27 \times \frac{\langle D_l \rangle^2}{N}}. \qquad (4.2.3)$$

The level spacings from these methods are shown in Table 4.2. The values obtained in ML way are completely consistent with those from the straight-line fit of the cumulative number of levels.

Table 4.2: Average level spacings $\langle D_0 \rangle$ [eV] evaluated from different methods.

	^{186}Os	^{187}Os	^{188}Os
Level set method	26.67 ± 1.25	5.47 ± 0.21	39.93 ± 1.87
BLF method	26.64 ± 0.23	5.67 ± 0.08	38.98 ± 0.47
ML method	27.24 ± 1.23	6.09 ± 0.24	41.73 ± 1.95

4.3 Statistical test of levels

4.3.1 Dyson - Mehta (Δ_3) statistics

The statistic Δ_3 approach was proposed by Dyson and Mehta [50][1]. This is a measure of long-range correlations. Δ_3 is defined as the mean square deviation of the cumulative number of the level (staircase plot) from a best fit straight line $AE + B$.

$$\Delta_3(L) = \min._{A,B} \frac{1}{L} \int_0^L (N(L') - AE - B)^2 dL', \tag{4.3.1}$$

where L represents the energy interval measured in units of the level spacing ($L = E_L/D_0$).
The analytical values of Δ_3 [51] can be calculated by

$$\begin{aligned} \text{Poisson} : \Delta_3(L) &= \frac{L}{15}. \\ \text{Wigner correlated} : \Delta_3(L) &= \frac{1}{\pi^2}\big(\ln(L) - 0.0687\big), \quad \text{S.D.} = 0.11. \\ \text{Wigner uncorrelated} : \Delta_3(L) &= \frac{L}{55 - (210/L)}, \quad \text{S.D.} = L/86 \quad (L > 10). \\ \text{BR (P+W)} : \Delta_3(L) &= \frac{(1-q)L}{15} + \frac{1}{\pi^2}\big(\ln(qL) - 0.0687\big). \end{aligned} \tag{4.3.2}$$

Here the fraction density q is of the same as the Eq. (4.1.3). q values are 0.93, 0.87 and 0.91 for each ^{186,187,188}Os of our data sets. Wigner uncorrelated is the intermediate behavior between Poisson and Wigner (GOE), a mixed phase space of regular and chaotic behavior. Δ_3 from our data sets are shown with the analytical values in Fig. 4.3. For L larger than 40, the Δ_3 statistic parameters become large and turned much further than theoretical expectations. It could be caused by large fluctuation of the cumulative level density.

4.3.2 Covariance of adjacent spacings

Also we can apply the correlation coefficient for adjacent nearest neighbor level spacings [51].

$$\rho(s_i, s_{i+r}) = \frac{\Sigma_{n=1}^{N-r}(s_n - \langle s_n \rangle)(s_{n+r} - \langle s_{n+r} \rangle)}{[(\Sigma_{n=1}^{N-r}(s_n - \langle s_n \rangle)^2)(\Sigma_{n=1}^{N-r}(s_{n+r} - \langle s_{n+r} \rangle)^2)]^{1/2}}. \tag{4.3.3}$$

s_i is the spacing between E_i and E_{i+1}. GOE theory shows this is sensitive to correlations between levels E_i and E_{i+2} and is predicted to have the

---

[1] They introduced Δ_1 and Δ_2 statistics also. Since their variances are larger than for Δ_3, these are not usually employed.

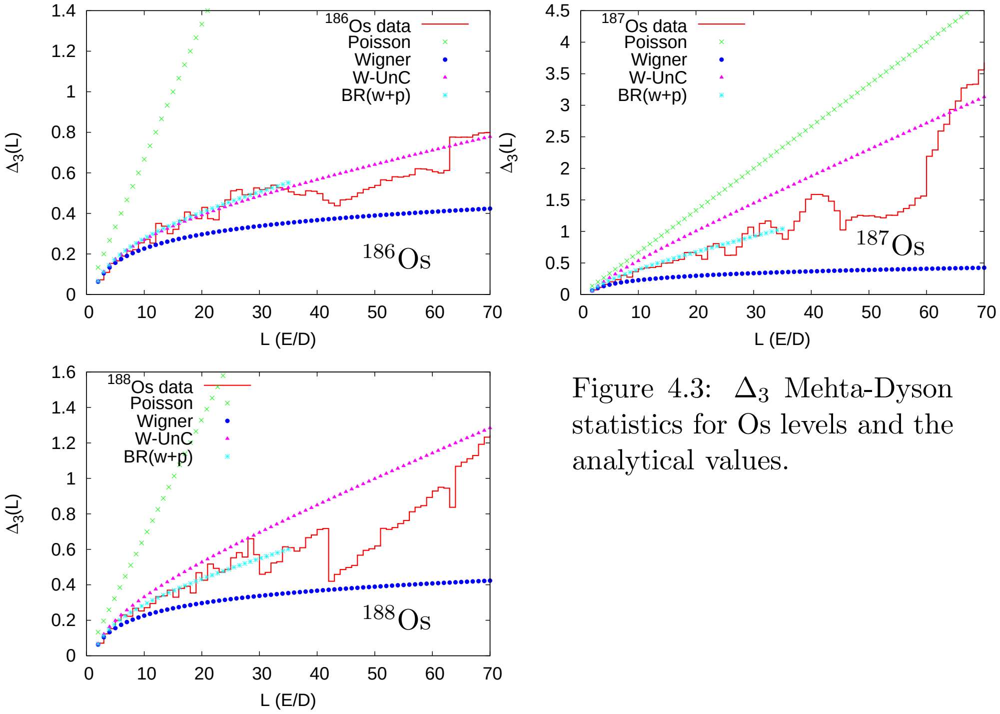

Figure 4.3: Δ_3 Mehta-Dyson statistics for Os levels and the analytical values.

values -0.27. The predicted value for Poisson is 0 which corresponds of no correlations of levels. ρ values of our data reported in Table 4.3 are small. To reach the GOE prediction, it might be necessary more unseen levels.

Table 4.3: Correlation of adjacent spacings from Os levels.

	$\rho(s_i, s_{i+1})$	$\rho(s_i, s_{i+2})$	$\rho(s_i, s_{i+3})$	$\rho(s_i, s_{i+4})$	$\rho(s_i, s_{i+5})$
^{186}Os	-0.14	-0.04	-0.09	-0.12	-0.08
^{187}Os	-0.08	-0.01	0.04	-0.09	-0.15
^{188}Os	-0.20	-0.01	-0.10	0.01	0.05

4.4 Average reduced neutron width

The neutron width distribution is only slightly affected by missing or spurious levels. As well known, a Gaussian distribution of reduced neutron width ($\Gamma_n^0 = \Gamma_n/\sqrt{E}$ for s-wave) amplitudes leads to the Porter-Thomas (P-T) distribution [52], χ^2-distribution with $\nu = 1$ degree of freedom,

$$f(x) = \frac{1}{\sqrt{2\pi x}}\exp(-\frac{x}{2}), \qquad x \equiv g\Gamma_n^0 \ / \ \langle g\Gamma_n^0\rangle. \tag{4.4.1}$$

For the strength function, the average reduced neutron width is needed.

The average reduced neutron width can be calculated simply by the total summation of the reduced neutron width divided by the number of widths. Otherwise using P-T distribution, several methods are adopted. Some of them are reported here below.

4.4.1 Missing level estimator (MLS)

This method has been initiated in 1976 by Keyworth and Moore then developed by Moore [53]. The total number of levels from a truncated neutron width distribution can be investigated using the method of moments. It is assumed that 1: the reduced neutron width obeys P-T distribution, and 2: larger widths are accurately known above $\langle g\Gamma_n^0\rangle/4$. The following properties can be shown,

$$\int_{\frac{1}{4}}^{\infty} f(x)dx = 0.617, \qquad \int_{\frac{1}{4}}^{\infty} \sqrt{g\Gamma_n^0} f(x)dx = 0.704\sqrt{\langle g\Gamma_n^0\rangle},$$
$$\int_{\frac{1}{4}}^{\infty} g\Gamma_n^0 f(x)dx = 0.969\langle g\Gamma_n^0\rangle. \tag{4.4.2}$$

This estimator uses this calculation,

$$A \equiv \frac{\sum_{(\langle g\Gamma_n^0\rangle/4)}^{\infty} g\Gamma_n^0}{(\sum_{(\langle g\Gamma_n^0\rangle/4)}^{\infty} \sqrt{g\Gamma_n^0})^2} = \frac{0.969}{(0.704)^2} \times \frac{0.617}{m} = \frac{1.2062}{m}. \tag{4.4.3}$$

where m is the number of levels that have Γ_n^0 larger than $\langle \mathrm{g}\Gamma_n^0\rangle/4$. Starting from the largest $g\Gamma_n^0$ value, the quantity of $A \times m$ is calculated. The summation is stopped at the point where the Am is 1.2062, here $4 \times g\Gamma_n^0$ = $\langle \mathrm{g}\Gamma_n^0\rangle$ and (m/0.617) gives the total number of levels in the interval. The estimated value is $\langle g\Gamma_n^0\rangle = \sum_m^N g\Gamma_n^0$ / ($m\times$ 1.715).

4.4.2 Method GAMN

This method uses the properties of the partial integrations of $f(x)$ [31].

$$A: \int_{1}^{\infty} f(x)dx = 0.32, \qquad B: \int_{0.5}^{1} f(x)dx = 0.17,$$
$$C: \int_{0.2}^{0.5} f(x)dx = 0.18, \qquad D: \int_{0.05}^{0.2} f(x)dx = 0.17. \tag{4.4.4}$$

Optional number that is expected averaged value sets as $\Gamma_n^{0\,\mathrm{est}}$. We can put that starting the arithmetic mean. These partial level numbers are N_A ($g\Gamma_n^0 > g\Gamma_n^{0\,\mathrm{est}}$), N_B ($1.0 \times g\Gamma_n^{0\,\mathrm{est}} > g\Gamma_n^0 > 0.5 \times g\Gamma_n^{0\,\mathrm{est}}$), N_C ($0.5 \times g\Gamma_n^{0\,\mathrm{est}} > g\Gamma_n^0 > 0.2 \times g\Gamma_n^{0\,\mathrm{est}}$), N_D ($0.2 \times g\Gamma_n^{0\,\mathrm{est}} > g\Gamma_n^0 > 0.05 \times g\Gamma_n^{0\,\mathrm{est}}$), respectively. When $N_A = 2N_B = 2N_C = 2N_D$ is satisfied, $\Gamma_n^{0\,\mathrm{est}}$ is decided

as $\langle\Gamma_n^0\rangle$ well.
Additionally the level spacing is delivered by these functions.
$D_1 = 0.32\times\Delta E_x/N_A$,
$D_2 = 0.49\times\Delta E_x/(N_A + N_B)$,
$D_3 = 0.69\times\Delta E_x/(N_A + N_B + N_C)$.

The average reduced neutron widths of the our Os data set are shown in Table 4.4. ^{187}Os data is used up to 2 keV of the neutron energy.

Table 4.4: Average reduced neutron widths $\langle g\Gamma_n^0\rangle$ [meV].

	^{186}Os	^{187}Os	^{188}Os
Arithmetic mean	7.2	2.21	9.6
GAMN method	6.1	1.37	5.6
MLS method	6.2 ± 0.7	2.00 ± 0.16	10.5 ± 1.5

4.4.3 Comparison of P-T distribution and the data

P-T distribution and our data sets are shown in Fig. 4.4. Distributions of ^{186}Os and ^{188}Os have good agreement with P-T distribution. Several small resonances ($x < 0.1$) of ^{187}Os can be missed; these resonances are probably located mainly at $E_n > 1.0$ keV. Moreover ^{187}Os has two spin populations of s-wave. This can be one reason of this disagreement.

The integrated P-T distribution for a single-level population can be written,

$$N(x) = N_0 \int_x^\infty f(x')dx' = N_0 \left[1 - \mathrm{erf}\sqrt{\frac{x}{2}}\right], \tag{4.4.5}$$
$$\mathrm{erf}(z) = \frac{2}{\sqrt{\pi}} \int_0^z e^{-t^2} dt = 1 - \mathrm{erfc}(z).$$

Here N_0 represents the number of resonances. The values of the $g\Gamma_n^0$ from our data sets are compared with the theoretical P-T distributions in Fig. 4.5. These of ^{186}Os and ^{188}Os have good agreements. Even if as mentioned in the last section, the data set of ^{187}Os included two spin populations, P-T distribution represents ^{187}Os level sets well.

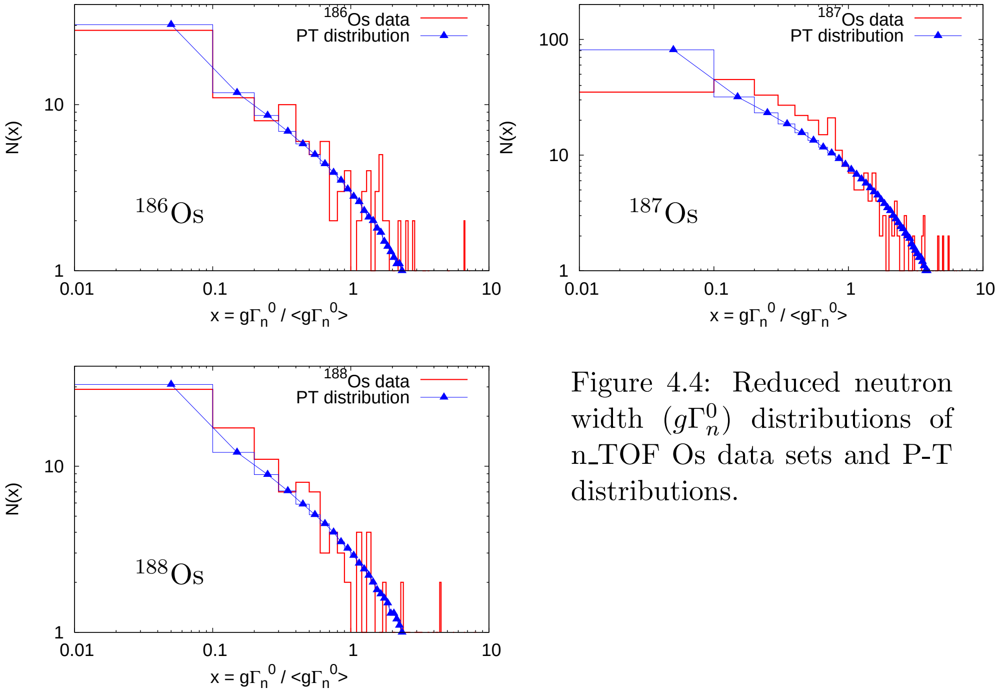

Figure 4.4: Reduced neutron width $(g\Gamma_n^0)$ distributions of n_TOF Os data sets and P-T distributions.

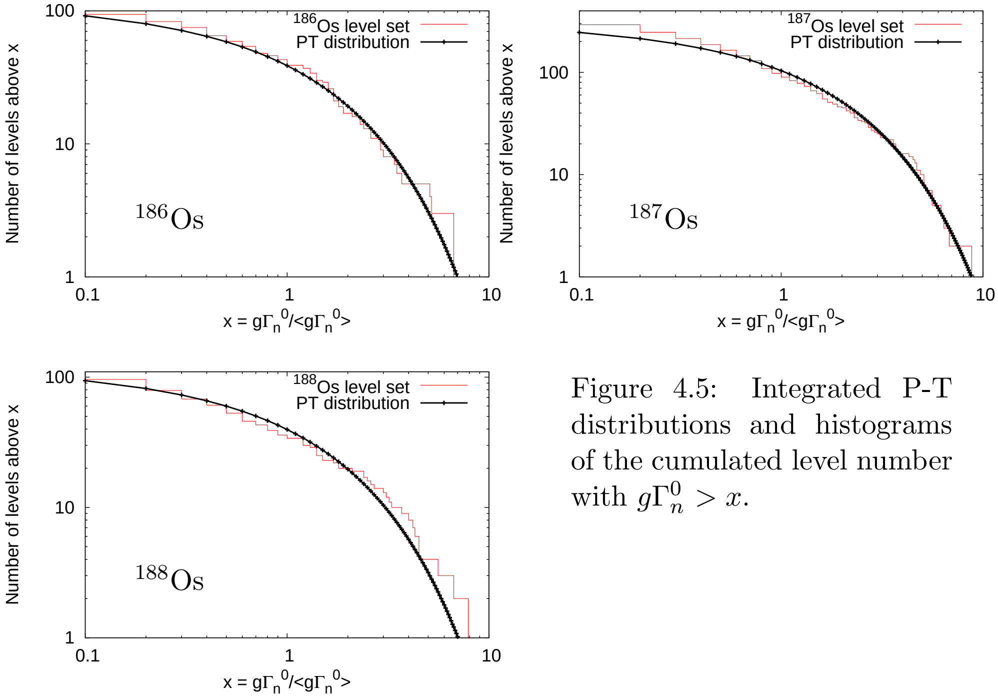

Figure 4.5: Integrated P-T distributions and histograms of the cumulated level number with $g\Gamma_n^0 > x$.

4.5 Neutron strength function

The neutron strength function for s-wave S_0 is defined as [54],

$$S_0 = \frac{\langle g\Gamma_n^0 \rangle}{\langle D_0 \rangle}\left(1 \pm \sqrt{\frac{2.27}{N_0}}\right) . \tag{4.5.1}$$

The uncertainty in S_0 is derived assuming a P-T distribution for the reduced neutron widths and a Wigner distribution for the level spacing, respectively. As I showed in the previous sections, there are several ways to determine D_0 and $\langle g\Gamma_n^0 \rangle$, I adopted BLF method for D_0, MLS method for $\langle g\Gamma_n^0 \rangle$.

4.6 Average radiative (γ) width

The average γ widths are delivered from resonances which have large neutron width (see Subsec. 3.2.1). The differences between these numbers and arithmetic averages of every resonance are less than about 3 %. The distributions of the radiative (γ) width are shown in Fig. 4.6. Large populations at $y = 1$, resonances which are fiexed the average radiative width are cut.

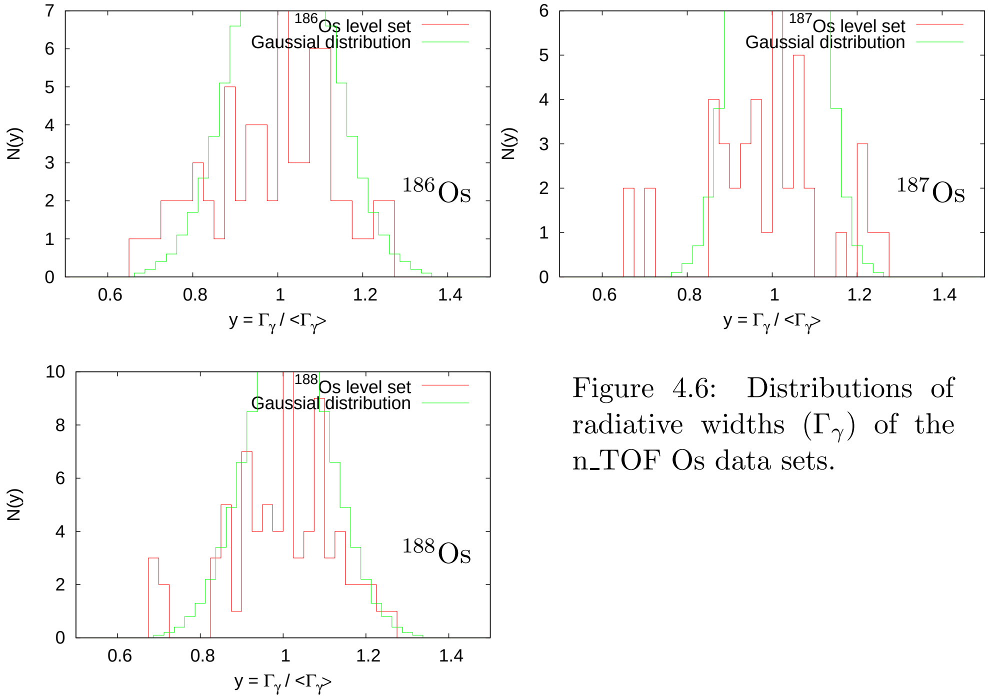

Figure 4.6: Distributions of radiative widths (Γ_γ) of the n_TOF Os data sets.

4.7 Summary of average resonance parameters

The statistical average parameters from our data sets of resolved resonance parameters are listed in Table 4.5. Also data from references are listed. The data proposed by Mughabghab (2006) [44] comes from a compilation of experimental informations and theoretical parameters. The data of Browne (1981) [55] and Winters (1982,1986) [56][57] are evaluated from experimental data.

In comparison to the reference data, the estimated average level spacings ($\langle \mathrm{D}_0 \rangle$) of ^{186}Os and ^{188}Os agree with Mughabghab and Browne reasonably, while ^{187}Os level density is larger than the references. It could be due to the uses of only few resonances, (26) in the evaluation [55] compared with the present analysis (176). n_TOF average radiative (γ) widths ($\langle \Gamma_\gamma \rangle$) appear smaller than the reference data. Neutron strength functions (S_0) have large uncertainties and n_TOF data is agreement within the quoted uncertainties with that of Mughabghab.

Table 4.5: Summary of average resonance parameters, average level spacings for s-wave ($\langle \mathrm{D}_0 \rangle$), average radiative widths ($\langle \Gamma_\gamma \rangle$), average reduced neutron widths ($\langle g\Gamma_n^0 \rangle$) and neutron strength functions for s-wave (S_0).

$\langle \mathrm{D}_0 \rangle$ [eV]	n_TOF	Mughabghab[44]	Browne [55]	Winters [56][57]
^{186}Os	26.6 ± 1.3	24.9 ± 0.4	30 ± 2	29.3 ± 2.7
^{187}Os	5.7 ± 0.1	4.56 ± 0.20	4.8 ± 0.2	10.8 ± 2.1 (J=0)
	-	-	-	6.4 ± 0.8 (J=1)
^{188}Os	39.0 ± 0.5	40 ± 2	40 ± 2	47.1 ± 5.5
$\langle \Gamma_\gamma \rangle$ [meV]				
^{186}Os	50 ± 1.5	60 ± 4	-	72 ± 5
^{187}Os	61 ± 1.7	76 ± 4	-	77 ± 2
^{188}Os	52 ± 1.8	82 ± 4	-	82 ± 4
$\langle g\Gamma_n^0 \rangle$ [meV]				$\langle \Gamma_n^0 \rangle$ [meV]
^{186}Os	6.2 ± 0.7	-	-	10.2 ± 3.3
^{187}Os	2.0 ± 0.2	-	-	8.7 ± 7.3
	-	-	-	2.1 ± 1.0
^{188}Os	10.5 ± 1.5	-	-	16.9 ± 7.4
$S_0 (\times 10^{-4})$				
^{186}Os	2.33 ± 0.32	2.30 ± 0.32	-	3.5 ± 0.9
^{187}Os	3.51 ± 0.29	3.04 ± 0.35	-	8.0 ± 4.5 (J=0)
	-	-	-	3.2 ± 1.1 (J=1)
^{188}Os	2.69 ± 0.36	2.39 ± 0.36	-	3.6 ± 1.2

Chapter 5

Implication on Re/Os clock

The results of the neutron capture cross sections measured at n_TOF including the unresolved resonance region (URR) [41] can be used to give an estimation of the universe age by means of the Re/Os clock method. If ^{186,187}Os cross sections are essential input data, on the other hand ^{188}Os data do not have direct implications. However for the application of the theoretical calculation, all three cross section data have to be treated.

In 1972 after proposing the idea of Re/Os clock by Clayton in 1963 [21], it was pointed out that ^{187}Os has a low-lying excited state at 9.75 keV which is strongly populated at $kT = 30$ keV [58]. This has widened the possibility of experimental and theoretical studies. Models that take into account Galactic chemical evolution (GCE, see Appendix F) were introduced in 1970s. Especially **astration** (transmutation of ^{187}Re and ^{187}Os) and the realistic ^{187}Re synthesis (r-process) have been studied theoretically as well as experimentally. The analysis of s-process branchings has developed with AGB stellar model calculation [59] since 1990s [60].

In Sec. 5.1, the estimation of the age of the universe using the original method [21] is shown. Later on, the final age evaluations, included additional contributions (the cross section enhancement and the AGB stellar model calculation) are discussed.

The thermal energy and the stellar temperature conversion is shown in Fig. 5.1. s-process studies are commonly focused at $kT = 30$ keV, $T8 \sim 3.5$, because this is the temperature at which AGB stars spend most of its time during the He burning phase (see Sec. 1.1.5).

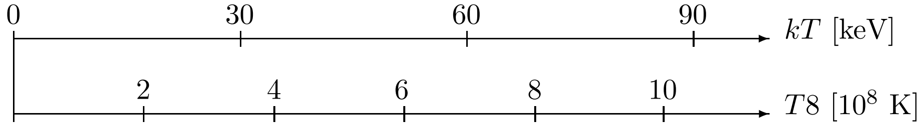

Figure 5.1: Conversion of the thermal energy into the temperature.

5.1 Basic idea and essential input data

5.1.1 Basic equations

In this section, the original idea shown by Clayton [21] is presented in its simple and approximated description.

The abundances N of elements in the relevant mass region can be expressed as follows :

$$
\begin{aligned}
&N^{\odot}_{186Os} = N^{s}_{186Os}\\
&N^{\odot}_{187Os} = N^{s}_{187Os} + N^{\beta}_{187Os}\\
&N^{\odot}_{187Re} = N^{r}_{187Re} - N^{\beta}_{187Re}\\
&N^{\beta}_{187Os} = N^{\beta}_{187Re}
\end{aligned}
$$

Here, s, r, β and $\odot$ represent the s-process, r-process, cosmoradiogenic origin productions and the solar system, respectively.

Using the s-process local approximation (Eq. (1.1.1)), $N^{s}_{187Os} \times \langle\sigma_{187Os}\rangle^{*} = N^{s}_{186Os} \times \langle\sigma_{186Os}\rangle^{*}$, one can write

$$N^{\beta}_{187Os} = N^{\odot}_{187Os} - N^{s}_{187Os} = N^{\odot}_{187Os} - \underbrace{\frac{\langle\sigma_{186Os}\rangle^{*}}{\langle\sigma_{187Os}\rangle^{*}}}_{\equiv f_s} \times N^{s}_{186Os}. \tag{5.1.1}$$

For the useful quantity, this can be rewritten as

$$\frac{N^{\beta}_{187Os}}{N^{\odot}_{187Re}} = \frac{N^{\odot}_{187Os}}{N^{\odot}_{187Re}} - f_s \times \frac{N^{s}_{186Os}}{N^{\odot}_{187Re}} \equiv R'. \tag{5.1.2}$$

A consideration of the simplest model of a closed system could lead to two equations,

$$\frac{dN_{187Re}(t)}{dt} = -\lambda_{\beta} N_{187Re}(t) + B(t), \tag{5.1.3}$$

$$\frac{dN^{\beta}_{187Os}(t)}{dt} = \lambda_{\beta} N_{187Re}(t). \tag{5.1.4}$$

λ_{β} is the β-decay rate of ^{187}Re, $B(t)$ is the r-process production rate of ^{187}Re. As it was discussed in Subsec. 1.1.6, even now r-process is less understood than s-process. It is assumed that r-process nucleosynthesis began at a time T before solar-system formation and decreased exponentially as $\exp(\Lambda t)$. Then the frequency of supernovae events at the time of the solar system formation is $\exp-(\Lambda t)$ times the initial frequency ($\equiv b$) in the Galaxy. Therefore $B(t) \equiv b \exp(-\Lambda t)$. t is measured backward in real time. Fowler and Hoyle have suggested this exponential decaying synthesis model [61]. This is so called Fowler[1]'s exponential model.

Using this model the left term of Eq. (5.1.2) can be written with λ_β,

$$\frac{N^{\beta}_{187Os}}{N^{\odot}_{187Re}} = \left\{\frac{\Lambda - \lambda_\beta}{\Lambda} \times \frac{1 - e^{-\Lambda t}}{1 - e^{-(\Lambda-\lambda_\beta)t}} e^{\lambda_\beta t}\right\} - 1 \equiv R. \tag{5.1.5}$$

Clayton used two special cases that were considered in B^{2}FH [1]

1. Sudden synthesis ($\Lambda \to \infty$) : R = e$^{\lambda_\beta t}$− 1,
2. Uniform synthesis ($\Lambda \to 0$) : R = (λ_βt / (1 − e$^{-\lambda_\beta t}$)) − 1,

and two models, in which the supernovae activity at solar-system formation is 37 and 14 % of the initial value. Originally Clayton showed the age of galaxy 11 Gyr for sudden synthesis model and 18 Gyr for uniform synthesis.

An intermediate case in which at the time of solar system formation the rate of r-process nucleosynthesis had decreased to 9 % of the initial value, i.e. $\Lambda = 1/0.43t$ [63] has served in the past as a convenient basis for comparison of results.

3. Fowler exponential rate synthesis ($\Lambda = 1/0.43t$).

This model is used for all present estimations.

5.1.2 Maxwellian averaged cross section (MACS)

Maxwellian averaged cross section is an important parameter which explains the cross sections at a given stellar temperature. The detail can be found in Appendix A. MACSs of our Os data set [64] are shown in Fig. 5.2, together with the data compiled by Bao [65]. MACSs of ^{186}Os and ^{187}Os are in agreement with previous measurements. Those of ^{188}Os are about 20% lower than previous data. In Table 5.1, MACSs at kT = 30 keV interesting for this analysis, are listed. These uncertainties are caused by the PHWT (2 %), the neutron flux (2 %), background corrections (∼ 2 %) and isotopic corrections (∼ 1 %) [41].

Table 5.1: n_TOF MACSs at kT = 30 keV (unit mbarn).

^{186}Os	^{187}Os	^{188}Os
414±17	969±32	294±14

---

[1] Fowler is one(F) of B^{2}FH (see Sec. 1.1) and won the Nobel price (shared with Subrahmanyan Chandrasekhar) in 1983 for his theoretical and experimental studies of the nuclear reactions of importance in the formation of the chemical elements in the universe [62].

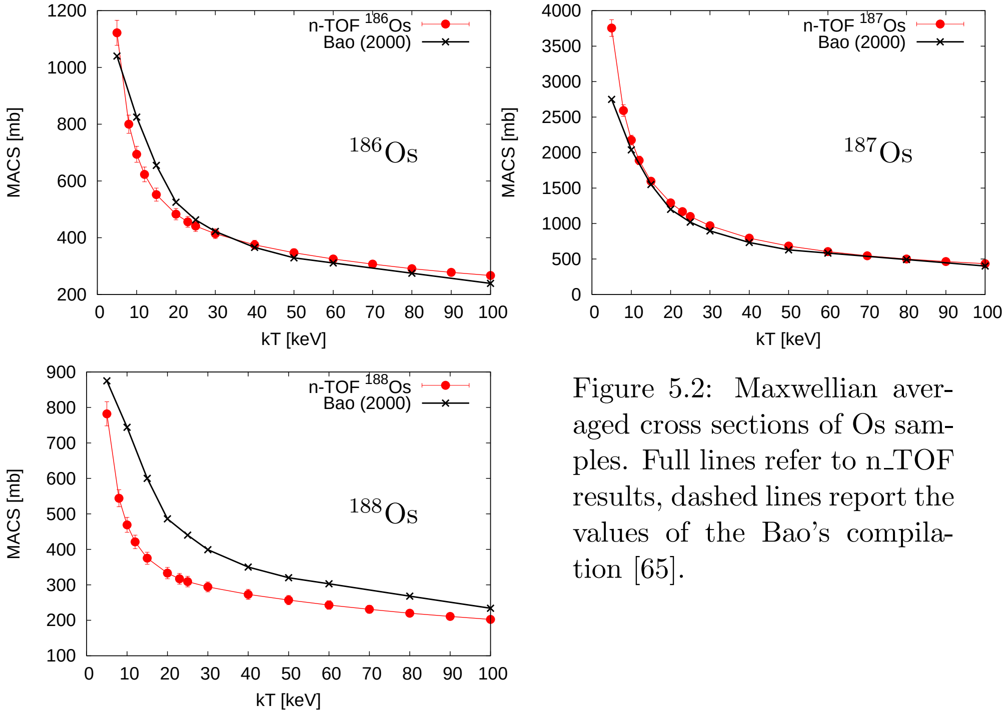

Figure 5.2: Maxwellian averaged cross sections of Os samples. Full lines refer to n_TOF results, dashed lines report the values of the Bao's compilation [65].

5.1.3 The solar system abundances

The solar abundances of several isotopes are available thanks to a fine job of Anders and Grevesse [14]; they started critical review of literature data, based on studies of C1 chondrites[2] and the solar photosphere and corona. The large uncertainties (~ 10 %) associated to these abundances have to be restrict for the calculations. Fästermann [66] reviewed the recent meteoritic data and showed the abundance normalized to ^{188}Os with small uncertainties (< 3 %).

5.1.4 ^{187}Re β decay rate

For the neutral ^{187}Re β-decay, only the first forbidden transition to the ground state of ^{187}Os is energetically possible. This transition has a small Q-value (2.66 keV) and a long half-life 41.2 ± 1.12 Gyr [20] which exceeds the age of the universe.

5.1.5 Original age estimation with n_TOF data

Using the input data listed in Table 5.2 ($(\langle\sigma_{186Os}\rangle^{\text{lab}}$ and $\langle\sigma_{186Os}\rangle^{\text{lab}}$ are used as $\langle\sigma_{186Os}\rangle^{*}$ and $\langle\sigma_{187Os}\rangle^{*})$, R' of Eq. (5.1.2) is evaluated as 0.10385 ±

---

[2] C chondrites are a class of chondritic meteorites comprising known groups and many ungrouped meteorites.

0.0091.

Table 5.2: Basic data for the present Re/Os clock estimation.

Quantity	Value	Reference
Abundance		
$N^{s}_{186Os}/N^{\odot}_{187Re}$	0.28452 ± 0.00712	[66]
$N^{\beta}_{187Os}/N^{\odot}_{187Re}$	0.22541 ± 0.00565	[66]
^{187}Re $t_{1/2}$ ($=\ln 2/\lambda_\beta$)[Gyr]	41.2 ± 1.12	[20]
MACS (30 keV) [mb]		
$\langle\sigma_{186Os}\rangle^{\mathrm{lab}}$	414 ± 17	[64]
$\langle\sigma_{187Os}\rangle^{\mathrm{lab}}$	969 ± 32	[64]
Age of solar system [Gyr]	4.559 ± 0.004	[15]

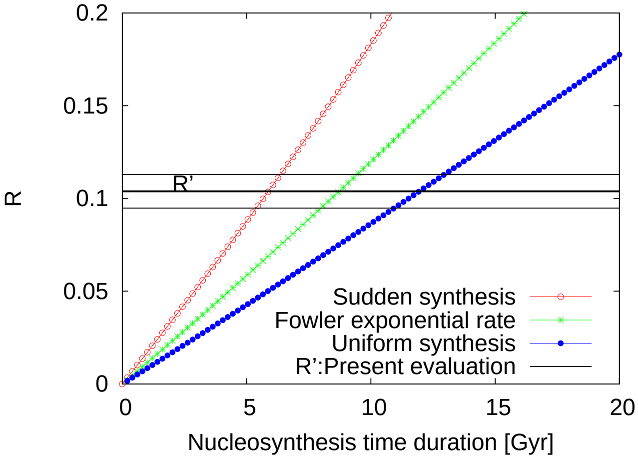

Figure 5.3: Relation between R ($\mathrm{N}^{\beta}_{187Os}/\mathrm{N}^{\odot}_{187Re}$) and the time duration of nucleosynthesis.

From Fig. 5.3 the nucleosynthesis time duration can be read from the cross point of our R' data and the galactic nucleosynthesis, R. The time age of the galaxy prior the formation of the solar system are respectively

Uniform synthesis : $\Delta_u = 11.95 \pm 1.06$ Gyr,
Fowler-model : $\boldsymbol{\Delta_{\mathrm{F}} = 8.72 \pm 0.77\mathrm{Gyr}}$,
Sudden synthesis : $\Delta_s = 5.87 \pm 0.52$ Gyr.

For the evaluation, Fowler-model is appropriated. Using the age of the solar system the age of the Galaxy is evaluated as $T_G = 13.28$ Gyr. Allowing for a time interval of 0.5 Gyr between Big Bang and the Galaxy formation, we can estimate an age of the universe of

$$T_u = (\Delta + 4.559 + 0.5) = 13.78 \pm 0.77 \text{ Gyr.} \qquad \text{(Age -1)}$$

This schematic description does not yet include the effect of enhancements of the excited states, astration and branchings. These effects are discussed here below.

5.2 Enhancement of the stellar cross section

5.2.1 Cross sections at stellar conditions

It is important to note that the high s-process temperatures imply that nuclei are excited by the intense and energetic thermal photon bath. This results in a significant population of low-lying states. In Fig. 5.4 the Os level schemes are shown. Only the energy of the first excited state level is reported.

Thermal population probability of the state of the excitation energy E_i is given by

$$P(E_i) = \frac{(2I_i + 1)\mathrm{e}^{-E_i/kT}}{\sum_j (2I_j + 1)\mathrm{e}^{-E_j/kT}}, \tag{5.2.1}$$

where I_i is the total angular momentum of the nuclear state i (i=0 is the ground state, i=1 is the first excited state, etc.).

Figure 5.5 shows the thermal populations of ^{186}Os and ^{187}Os. At kT = 30 keV, the ^{186}Os's ground state is populated at 95 %. For the ^{187}Os case, the ground state population is only about 30 %, therefore the remaining 70 % are the excited state populations. In particular the population of the first excited state is about 47 %, because this state is 9.75 keV low-lying. From experimental data, we have only the ground state's cross section which represents only about 30 % of the information required. To recover the missing information, a direct experiment is not possible, because of the infeasibility of maintaining a laboratory sample target in an excited state. Effective states are the ground state and up to 4th excited states for ^{187}Os, the ground state and the first excited state for ^{186}Os.

The real cross section at the thermal condition can be calculated by the sum of weighted cross sections with this factor $P(E_i)$. For the excited state's cross sections could be calculated in a consistent manner from theory or indirect measurements. This second item will be discussed in Subsec. 5.2.4.

5.2.2 Statistical model calculation

The approach most widely used for the reaction cross section calculations is the statistical model of compound nuclear reactions [67] (Hauser-Feshbach (H-F) statistical model [23]). This is based mainly on the assumption of a high level density in the compound nucleus, the cross section can then

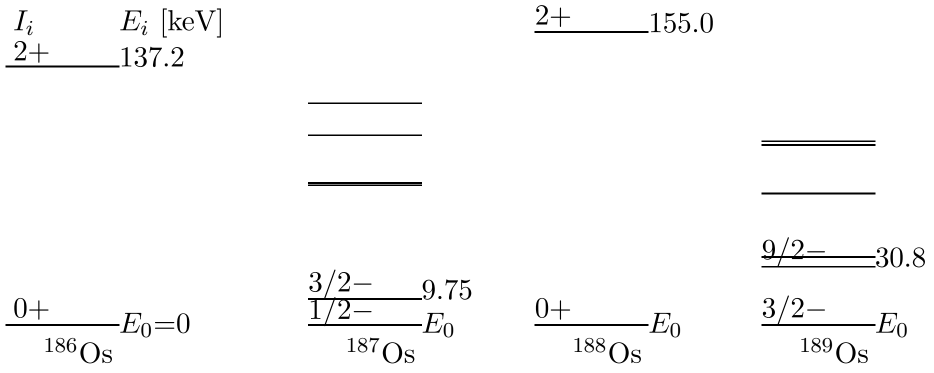

Figure 5.4: Nuclear level diagrams for Os isotopes.

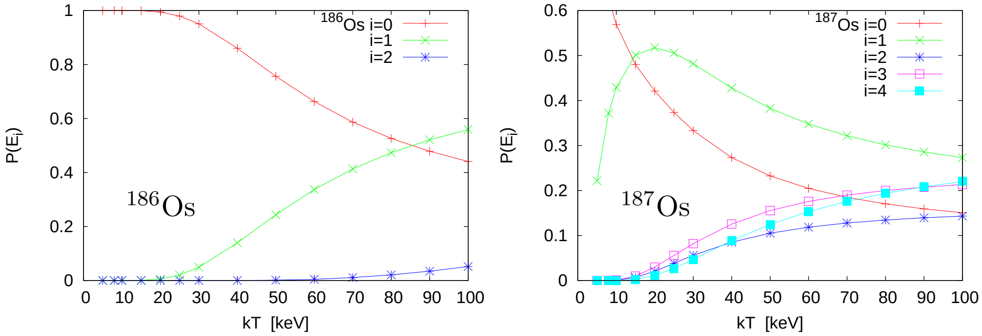

Figure 5.5: Thermal populations of ^{186}Os(left panel) and ^{187}Os(right panel).

be described by average transmission coefficients T. For the capture cross section, this leads to the well known H-F formula :

$$\sigma_{n,\gamma}(E_n) = \pi \bar{\lambda}_n^2 \sum_{J\pi} g_J \frac{\sum_{ls} T_{n,ls} T_{\gamma,J}}{\sum_{ls} T_{n,ls} + \sum_{ls} T_{n',ls} + T_{\gamma,J}} W_{\gamma,J}. \qquad (5.2.2)$$

Where $\bar{\lambda}_n$ is the neutron wavelength divided by 2π. Concerning parameters of spin (J, g, l, s), see Subsec. 1.4.5. The neutron and γ-ray transmission coefficients are denoted by T_n and T_γ respectively. W is the width fluctuation factor. The level density is the essential input parameter for transmission coefficients. The calculations are executed through the nuclear reaction code, TALYS [30].

1. Level density (ρ)

Several models were presented. The Gilbert-Cameron model ($\equiv$ GCM) [68] was adopted for the present data analysis.
At low energy, a constant temperature model (CTM $\equiv T$) is applied. This is based on the experimental evidence that the cumulated histogram $N(E_x)$

of the first discrete levels (the energy E_x) can be well reproduced by an experimental law of the type

$$N(E_x) = \exp\Big(\frac{E_x - E_0}{T}\Big), \tag{5.2.3}$$

where T is the nuclear temperature, and E_0 is the back-shift energy. For higher energies, Fermi gas model (FGM $\equiv F$) is applied.

The level density ρ corresponds to the number of nuclear level per MeV around an excitation energy E_x. This can be written for the total level density as,

$$\rho_T(E_x, J, \Pi) = P(E_x, J, \Pi) R_F(E_x, J) \underbrace{\frac{1}{T}\exp(\frac{E_x - E_0}{T})}_{= \rho_T^{\text{tot}}} : E_x \leq E_M.$$

$$\rho_F(E_x, J, \Pi) = P(E_x, J, \Pi) R_F(E_x, J) \underbrace{\frac{1}{\sqrt{2\pi}\sigma}\frac{\sqrt{\pi}}{12}\frac{\exp[2\sqrt{a(E_x - \Delta)}]}{a^{\frac{1}{4}}(E_x - \Delta)^{\frac{5}{4}}}}_{= \rho_F^{\text{tot}}} : E_x \geq E_M.$$

$$P(E_x, J, \Pi) = \frac{1}{2}, \quad R_F(E_x, J) = \frac{2J+1}{2\sigma^2}\exp\Big[-\frac{(J+\frac{1}{2})^2}{2\sigma^2}\Big]. \tag{5.2.4}$$

P and R_F are the distributions of parity and Fermi gas spin. a is the level density parameter and σ^2 is spin cutoff parameter. Δ, the energy shift, is an empirical parameter which is related to the pairing energy, which is included to simulate the known odd-even effect in nuclei. T, E_0 and E_M (matching energy) are chosen with the constraint $\rho_T^{tot}(E_M) = \rho_F^{tot}(E_M)$ between two models. a can be obtained from the average s-wave level spacing using $1/\langle D_0 \rangle = \rho_F(S_n)$. The parameters of the present Os analysis are listed in Table 5.3.

Histograms plots of levels and GCM, FGM model levels are shown in Fig. 5.6. It must be noted that the level spacing of ^{A}X is the averaged spacing of the unbound states of $^{A+1}$X. Therefore the level density of $^{A+1}$X is connected with the level spacing of ^{A}X directly.

Table 5.3: Summary of parameters for the level density calculations.

Sample	D_0 [eV]	T [K]	E_0 [MeV]	a (S$_n$)
^{186}Os	26.6	0.515	−1.136	23.6340
^{187}Os	5.7	0.510	0.027	22.6330
^{188}Os	39.0	0.504	−1.105	24.1705

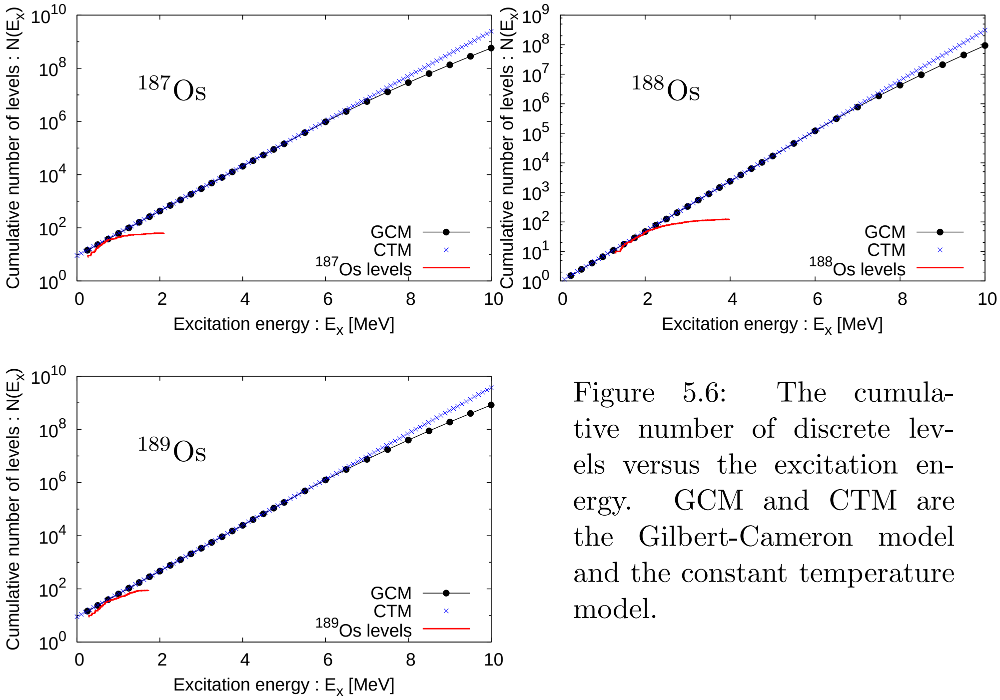

Figure 5.6: The cumulative number of discrete levels versus the excitation energy. GCM and CTM are the Gilbert-Cameron model and the constant temperature model.

2. Neutron transmission coefficients (T$_n$)

The neutron (also particle) transmission coefficients are normally derived from the optical model theory, both for the elastic and inelastic scattering channels. Traditionally phenomenological optical model potentials (OMP) have been used. The optical potential for nucleon-nucleus scattering can be written as

$$U(r) = U_V(r) + U_D(r) + U_{so}(r) + U_C(r) = V(r) + iW(r), \tag{5.2.5}$$

where $U_{V,D,SO,C}$ are the components of the volume-central (V), surface-central (D), spin-orbit (so) and Coulomb (C) potentials, respectively. $V(r)$ is the real part, $W(r)$ is the imaginary part. The OMP used in this work consists of V_V, W_D and W_{so}. These potentials can be written as

$$\begin{aligned} V_V &= v_V \cdot f(r, R_V, a_V), \\ W_D &= -4a_D w_D \cdot \frac{\mathrm{d}}{\mathrm{dr}} f(r, R_D, a_D), \\ W_{so} &= w_{so}\Big(\frac{\hbar}{m_\pi c}\Big)^2 \cdot \frac{1}{r}\frac{\mathrm{d}}{\mathrm{dr}} f(r, R_{so}, a_{so}). \end{aligned} \tag{5.2.6}$$

The $f(r, R, a)$ is Woods-Saxon form factor

$$f(r, R_i, a_i) = \frac{1}{1 + \exp[(r - R_i)/a_i]}, \tag{5.2.7}$$

where the geometry parameters are the radius $R_i = r_i A^{1/3}$, with A being the atomic mass number and diffuseness parameters a_i. This formalism assumes that nucleus is spherical, thus not strongly deformed. For a more general model, coupled-channels should be included, i.e. the coupling of the rotational states in the target such as the 0^+, 2^+ and 4^+ states in ^{186}Os and the $1/2^-$, $3/2^-$ and $5/2^-$ states in ^{187}Os. This deformation effect can be treated in TALYS calculation. However the calculations with the deformation are not able to reproduce the experimental data better than the spherical OMP model [69]. Thus, in this presentation no more care is devoted to this point.

In Table 5.4 the parameters used for the present calculation are listed.

Table 5.4: Optical model parameters (standard) for the present work [70].

v_V [MeV]	r_V [fm]	a_V [fm]	w_D [MeV]	r_D [fm]	a_D [fm]	w_{so} [MeV]	r_{so} [fm]	a_{so} [fm]
46.0	1.265	0.620	14.0	1.353	0.250	7.0	1.265	0.620

The s-wave neutron strength function is related to the imaginary part of the optical model phase shift [44]. A higher neutron energy gives a lower neutron strength function. The s-wave neutron strength functions obtained from OMP ($E_n < 1$ keV) are listed in Table 5.5.

Table 5.5: S-wave neutron strength functions from the optical model potential.

S_0 ($\times 10^{-4}$)	^{186}Os	^{187}Os	^{188}Os
Standard OMP	3.0	2.95	2.9
Applied OMP (Subsec. 5.2.5)		4.3	
n_TOF (Sec. 4.7)	2.33 ± 0.32	3.51 ± 0.29	2.69 ± 0.36

3. γ-ray transmission coefficients ($\mathbf{T}_\gamma$)

γ-ray transmission coefficient is given by

$$T_{Xl}(E_\gamma) = 2\pi E_\gamma^{(2l+1)} \underbrace{\frac{\langle \Gamma_{Xl}(E_\gamma) \rangle}{E_\gamma^{(2l+1)} D}}_{f_{Xl}(E_\gamma)} . \tag{5.2.8}$$

Where $f_{XL}(E_\gamma)$ is the energy-dependent γ-ray strength function for multipolarity L of type X (where $X = M$ or E). At sufficiently low incident neutron energies, the $f_{XL}(E_\gamma)$ can be delivered with average radiative (γ-ray) width $\langle \Gamma_\gamma \rangle$ and level spacing D extracted from experimental data. In the high energy region($E_\gamma > S_n$, the neutron separation energy), Giant dipole resonance (GDR) parameters are used. Some models were presented ; between them the Brink-Axel model with a standard Lorentzian form described the giant resonance shape [30] is adopted. The γ-ray strength function of this model can be written as :

$$f_{Xl}(E_\gamma) = \frac{1}{(2l+1)\pi^2\hbar^2c^2} \times \frac{\sigma_{Xl}E_\gamma\Gamma^2_{Xl}}{(E^2_\gamma - E^2_{Xl})^2 + E^2_\gamma\Gamma^2_{Xl}}, \tag{5.2.9}$$

where E_{Xl}, Γ_{Xl} and σ_{Xl} are the energy, width and strength of the giant resonance. The parameters of GDR for Os are listed in Table 5.6, these are experimental values. In Ref. [71] there is no data for ^{187}Os, therefore the parameters of ^{189}Os are applied. For M1 transitions, the parameters can be written as

$$\begin{aligned} &f_{M1}(7\text{MeV}) = 1.58A^{0.47},\ E_{M1} = 41.0A^{-1/3}\text{MeV},\ \Gamma_{M1} = 4\text{MeV} : (l=1). \\ &\sigma_{Ml} = 8\times10^{-4}\sigma_{M(l-1)},\quad E_{Ml} = E_{M(l-1)},\qquad \Gamma_{Ml} = \Gamma_{M(l-1)}. \end{aligned} \tag{5.2.10}$$

Table 5.6: Experimental giant dipole resonance parameters [71].

Nucleus	Xl	E_{Xl} [MeV]	Γ_{Xl} [MeV]	σ_{Xl} [mb]
^{188}Os	E1	12.81	2.71	268
^{188}Os	E2	14.68	3.62	395
^{189}Os , (^{187}Os)	E1	12.68	2.76	260
^{189}Os , (^{187}Os)	E2	14.88	4.19	390

Partial γ-ray strength functions of ^{187}Os are shown in Fig. 5.7.

The s-wave radiative (γ) width can be obtained by integrating the γ-ray transmission coefficients over the density of final states that may be reached in the first step of the γ cascade. The s-wave radiative (γ) widths delivered by the integration of T from GDR are shown as (A) in Table 5.7. Practically this radiative widths would be re-normalized to adjust optional data. To fix our Os data (practically reproducing the n_TOF MACSs at 30 keV), the radiative widths are chosen as (B) in Table 5.7.

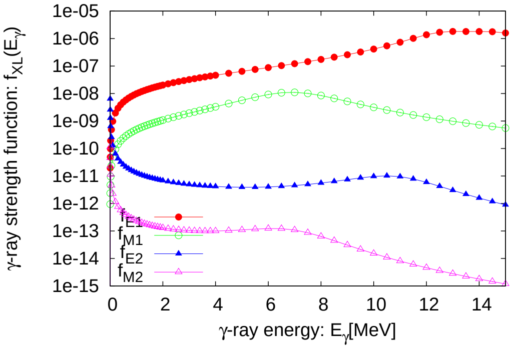

Figure 5.7: Partial γ-ray strength functions of ^{187}Os.

The γ- transmission coefficients are thus multiplied for the calculation.

There is discrepancy between average radiative widths obtained by the theoretical calculations and the experimental n_TOF data.

Table 5.7: Average radiative (γ) widths from the theoretical calculations.

Γ_γ [meV]		^{186}Os	^{187}Os	^{188}Os
From GDR	(A)	80.2	103.3	78.9
From GDR + renormalization	(B)	42.1	95.5	34.2
From n_TOF (Sec. 4.7)		50.0 ± 1.5	61.0 ± 1.7	52.0 ± 1.8

4. Width fluctuation (W)

In order to correlate width fluctuation between the incident and outgoing waves, the original H-F formula needs to be multiplied by a factor W, called width fluctuation correction factor (WFCF). The Gaussian orthogonal ensemble (GOE) approach can be used, but it needs a complicated integral calculation. For this reason parameterization ways have been studied widely. The comparisons of various available methods have been done [72]. The Moldauer method was then adopted for this analysis.

In the Moldauer approach, WFCF is based on the assumption that a χ^2 law with ν degree of freedom applies for the partial width Γ which can be calculated from a Porter-Thomas distribution. This can be expressed by the following expressions [30] :

$$W_{ab} = \Big(1+\frac{2\delta_{ab}}{\nu_a}\Big)\int_0^{+\infty} \underbrace{\Pi_c\Big(1+\frac{2T_c x}{\nu_c \Sigma_i T_i}\Big)^{-(\delta_{ac}+\delta_{bc}+\nu_c/2)}}_{\equiv A} \mathrm{d}x.$$

$$\nu_a = 1.78 + (T_a^{1.212} - 0.78)\exp(-0.228\Sigma_c T_c).$$

$$A \sim= \exp\Big(-\frac{T_\gamma^{\mathrm{eff}} x}{\Sigma_i T_i}\Big) \quad : \text{ Capture reactions.}$$

$$A \sim= \left(1+\frac{2T_{\mathrm{mean}}(U)}{\nu_{\mathrm{mean}}\Sigma_i T_i}\right)^{-N_{\mathrm{eff}}(U)\nu_{\mathrm{mean}}/2} \quad : \text{ Continuum reactions.} \quad (5.2.11)$$

For the capture reaction, a and b correspond n, γ respectively.

5. Cross section calculation

Following these parameters for the H-F model, Os cross sections can be calculated. Once the parameters are set for the cross section of the ground state, the calculation of cross sections at the excited states can be performed.

5.2.3 Stellar Enhancement Factor (SEF)

Once the cross sections in different states are calculated, we can have MACSs in each state. These MACSs weighted with the thermal population probability (Eq. (5.2.1)) give MACS at the stellar condition. As shown in Subsec. 5.2.1, for ^{186}Os, which states are not only the ground state, also first and the second excited state have to be calculated. These weighted cross sections are adopted to complete the stellar cross section. For ^{187}Os the same procedure is followed.

Stellar enhancement factor : SEF is defined as

$$(\mathrm{SEF})_{\mathrm{kT}} = \frac{\langle \sigma_{n,\gamma} \rangle^{*}_{\mathrm{kT}}}{\langle \sigma_{n,\gamma} \rangle^{lab}_{\mathrm{kT}}}. \tag{5.2.12}$$

Here lab means that MACS is obtained with the sample at the ground state (like in the laboratory) and * means in stellar environments.

At $kT = 30$ keV, the most interesting value for s-process studies, ^{186}Os has almost ground state, i.e. SEF_{186Os} is ~ 1.0. The key point is SEF_{187Os}, less populated at the ground state.

For $f_s (= \langle \sigma_{186Os} \rangle^{*}$ / $\langle \sigma_{187Os} \rangle^{*})$ in Eq. (5.1.1), the rate of MACS (lab. i.e. from the nuclei in the ground state) needs to be corrected with SEF_{186Os} / $\mathrm{SEF}_{187Os} \equiv F_\sigma$, this is the so called the correction factor. Originally F_σ was estimated $0.80 \sim 1.10$ [67].

5.2.4 Additional cross section data for Re/Os clock

In this section, the other cross section data which can not be determined directly by experiments and needs to be evaluated from a combination of theoretical considerations and laboratory information is reported.

To apply the issue for the correction factor F_σ (the SEF rate of ^{186}Os and ^{187}Os), especially on the effect of the neutron capture on the first excited state (9.75 keV) of ^{187}Os, additional cross section data was introduced.

Besides unstable nuclei cross sections can be obtained by means of calculations with the neighbor nuclei's cross section data.

5.2.5 ^{187}Os inelastic (n, n') cross sections

Woosley and Fowler [67] noted that if neutron scattering transmission coefficients (absorption probabilities) for the excited level happen to be much smaller than those for the ground state, then capture from the excited level at stellar temperatures would be weak. Then the factor F_σ would be $>$ 1.1. ^{187}Os inelastic cross section can directly measure the transmission from the $1/2^-$ ground state of ^{187}Os to its 9.75 keV, $3/2^-$ excited state. The statistical analysis of the capture data gave a lower bound to the inelastic scattering cross section at a neutron energy 30 keV. Adjustments of the calculated inelastic cross section to a measured value should increase the reliability of the predictions of the capture cross sections at $kT = 30$ keV.

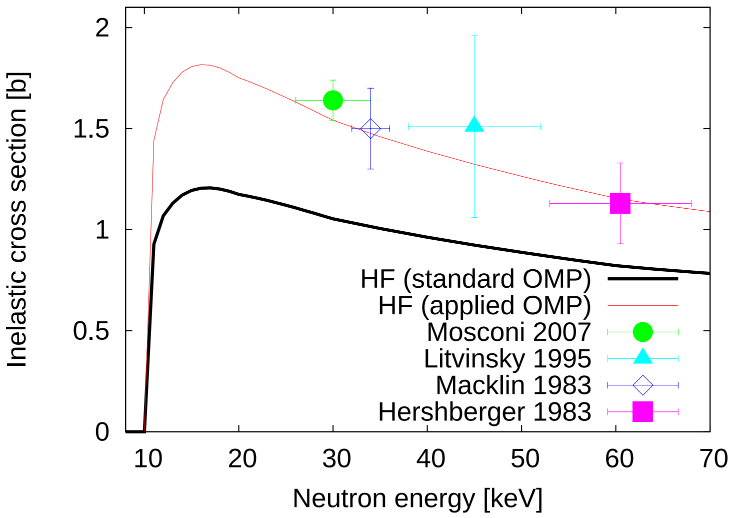

Figure 5.8: Inelastic scattering cross sections from reference data and H-F calculations.

For $\sigma_{nn'}$ at 30 keV ($\sigma_{nn'}$(30 keV)), Winters et al.(1979) [73] estimated $\sigma_{nn'}$(30 keV)$\lesssim$ 0.5 b, with the lower bound of 0.3 b $\lesssim \sigma_{nn'}$(30 keV) derived by Winters and Macklin (1982) [57], they lead to $1 \lesssim F_\sigma \lesssim 1.15$ at $kT = 30$ keV according to the calculation of [67].

For sake of comparison in Fig. 5.8 the experimental data of neutron inelastic scattering cross sections are shown including recent data, Mosconi 2007 [41], Litvinsky 1995 [75]. Macklin (1983) [76] and Hershbarger (1983) [77] reported $F_\sigma = 0.80$ and $0.80 \sim 0.83$, respectively.

The thick black line in Fig. 5.8 shows the H-F calculation from standard OMP (Table 5.4) of the present analysis. From the calculation with the applied OMP (v_V = 46 MeV → 43 MeV), the thin red line is obtained.

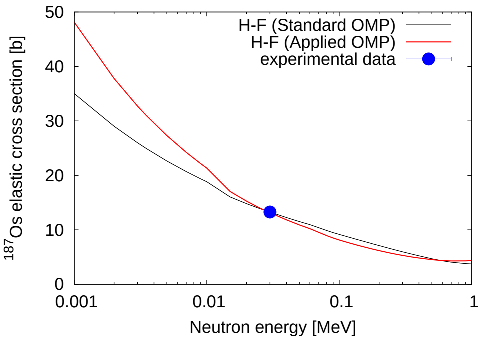

Figure 5.9: Elastic scattering cross sections from H-F calculations. The experimental data is from Ref. [75].

Elastic cross section calculated with these parameters, standard OMP and applied OMP are shown in Fig. 5.9. Obtained neutron strength functions with these OMPs are listed in Table 5.5.

5.2.6 ^{189}Os capture cross sections

^{189}Os nucleus have the $3/2^-$ for the ground state and $1/2^-$ for the excited state at 36.2 keV, these are reversed compared with the case of ^{187}Os that has $1/2^-$ ground state and $3/2^-$ for 9.75 keV level. In other words, the ground state of ^{189}Os has the same Nilsson[3] single-quasi-particle quantum numbers $K[Nn_n\Lambda] = 3/2$ [512] as for the first excited state of ^{187}Os. Then a H-F calculation which correctly reproduces both the ^{187}Os(n, γ) and ^{189}Os (n, γ) measured cross sections could be expected to accurately describe the capture cross section for ^{187}Os first excited state [78]. Moreover the elastic/inelastic scattering cross section was applied [79]. These analysis brought that $F_\sigma = 0.79 - 0.83$.

5.2.7 Photo-disintegration ((γ, n), inverse) cross sections

To estimate the neutron capture cross section on the basis of theoretical models, the inverse, photo-neutron (γ, n) reaction data can be used. The idea is to find a parameter set for the H-F model which reproduces the photo neutron cross sections and to apply this set for the calculation of the required inverse rate more reliably than by using the global or local parameter systematics constructed from neighboring nuclei. The measurements of ^{186,188,189,190,192}Os and giant resonance parameters are reported in [71]. For the investigation of the s-process branching (^{186}Re and ^{185}W are unstable see Subsec. 5.4.1), ^{187}Re and ^{186}W were measured [80] [81].

5.3 Age estimation adding SEF

In this section, the age estimation including SEF is discussed.

5.3.1 Calculated cross sections

The cross sections extracted from H-F calculation (Subsec. 5.2.2) are shown in Fig. 5.10 compared with the previous experimental data of Browne [55], Winters [74] and Segawa [82]. For the applied OMP calculation of ^{187}Os, see Subsec. 5.2.5. A very good agreement is found between H-F calculations and n_TOF experimental data for all Os isotopes. However it needs to note that these calculations are normalized in terms of T_γ (see Subsec. 5.2.2-3).

---

[3] The Nilsson model describes the single-particle states of deformed nuclei.

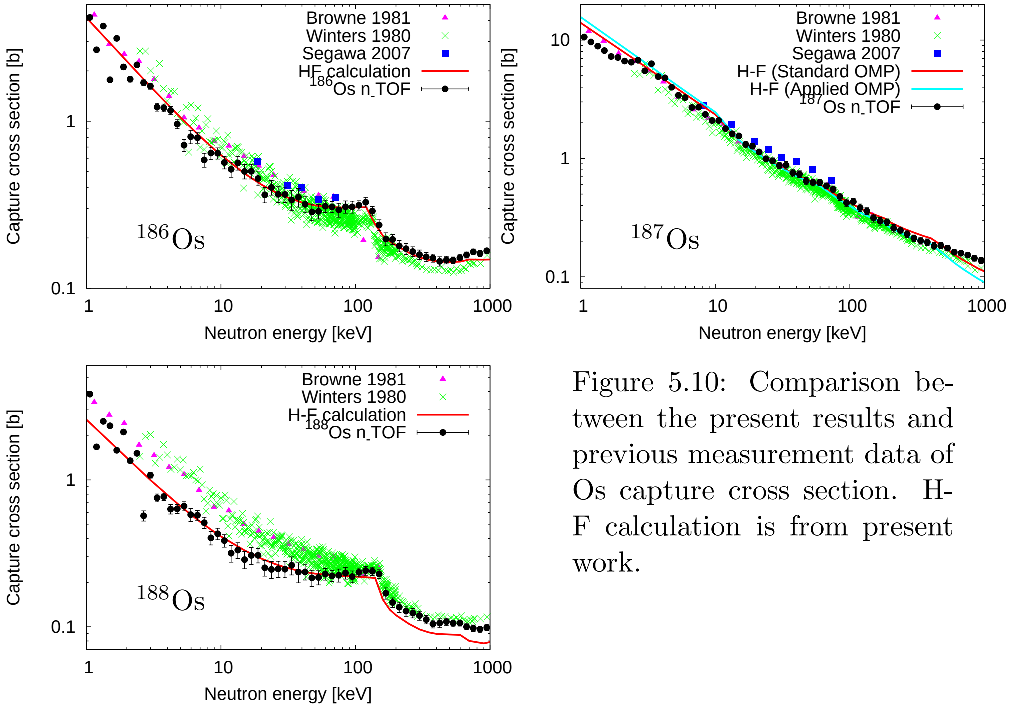

Figure 5.10: Comparison between the present results and previous measurement data of Os capture cross section. H-F calculation is from present work.

5.3.2 SEF from calculations

Figure 5.11 shows SEF of ^{186}Os, ^{187}Os from the present analysis calculation (Subsec. 5.3.1) with spherical OMP (see Subsec. 5.2.3).

Using the applied OMP (see Subsec. 5.2.5), this gives $\text{SEF}_{^{187}OS}$ (30 keV) = 1.2978 and F_σ is evaluated as 0.793. Considering these two values from standard OMP and applied OMP, adopted SEF numbers of the present analysis are listed in Table 5.8.

In Fig. 5.12 the SEF rates (F_σ) which are derived from the standard OMP and the applied OMP are shown.

Table 5.8: SEFs for the present Re/Os clock estimation.

Quantity	Data
SEF at 30 keV	
^{186}Os	1.0296
^{187}Os	1.2978 ± 0.0300
F_σ ($\text{SEF}_{^{186}Os}$ / $\text{SEF}_{^{187}Os}$)	0.7933 ± 0.0183

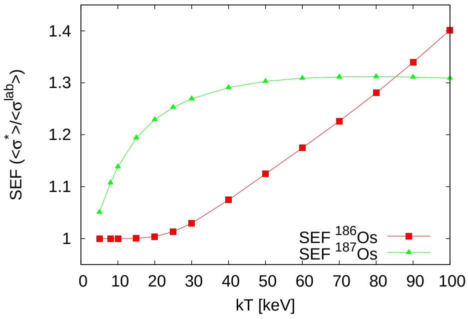

Figure 5.11: Stellar enhancement factors of ^{186}Os and ^{187}Os obtained by H-F calculations with spherical OMP.

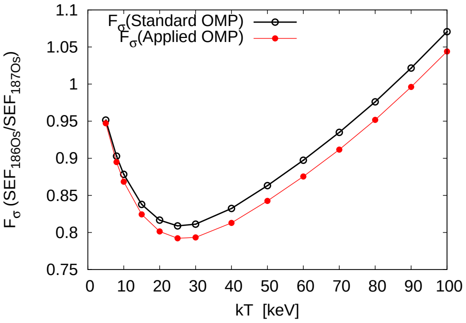

Figure 5.12: The SEF rates ($\mathrm{SEF}_{186Os}/\mathrm{SEF}_{187Os}$), F_σ evaluated from standard OMP and applied OMP.

5.3.3 Age estimation with SEF

In a following step MACS rate (f_s) is obtained multiplying the rate of our MACS data in Table 5.2 by F_σ. Using the same process in Sec. 5.1 and Fowler model, Δ is evaluated as 10.92 ± 0.71 Gyr and the age of universe is evaluated as

$$T_u = 15.78 \pm 0.72 \text{ Gyr.} \qquad \text{(Age -2)}$$

This age is 2 Gyr longer than the age evaluated without SEF (Age -1). In other words, starting from the original method, the contribution of SEF to the age is 2 Gyr.

5.3.4 The uncertainties on the evaluated age

The partial uncertainties of the age evaluated with the parameters in Table 5.2 and SEF are listed in Table 5.9. Thanks to the performance of the n_TOF facility, the uncertainty on the cross sections (MACS) is not longer dominating on the final result of the age.

Table 5.9: Age uncertainties from various components.

Δ	Uncertainties [Gyr]				
[Gyr]	Total	Abundances	β-decay	MACS	SEF-187
10.92	**0.72**	0.49	0.30	0.40	0.18

There are still another considerations. It is discussed in the next section.

5.4 Other considerations

In the previous sections, the s-process local approximation (Eq. (1.1.1)) and Fowler model are applied. To improve the Re/Os clock, further considerations of more realistic stellar condition are needed.

5.4.1 S-process branchings at ^{185}W and ^{186}Re

The branchings occur when the reaction flow reaches an unstable nucleus that exhibits comparable neutron capture and β-decay rates. The s-process flow in the W-Re-Os region branches at ^{185}W (terrestrial β-decay life time $\sim$ 75 days) and ^{186}Re (terrestrial β-decay life time of $\sim$ 4 days). These branching channels give s-process contribution to ^{187}Re (see Fig. 5.13).

MACS, SEF and β-decay rates become essential input data. Neutron capture cross sections of ^{185}W and ^{186}Re were derived with the statistical model parameters from ^{185}Re and ^{187}Re measurements [60].

As a first step, the branching problem was investigated within the framework of the schematic s-process models [83] and a factor for s-process branching correction (F_b ; $f'_s = f_s \times F_\sigma \times F_b$) was introduced. This can be called classical model.

Moreover it was shown that this classical approach is not suited for describing a realistic situation; therefore the stellar model for low AGB stars [59] is recommended [60].

The recent results of the AGB stellar model calculation [84] showed that the branching at ^{186}Re does not provide any appreciable contribution, on the other hand the branched path at ^{185}W results in a 10 % s-process contribution to ^{187}Re.

5.4.2 Temperature dependence of ^{187}Re β decay

Since ^{187}Re may become highly ionized in the hot plasma of a star, the β-decay rate may be substantially greater in certain astrophysical environments than in the laboratory. This phenomena is so-called astration effect.

The half life of a completely bare nucleus ^{187}Re^{75+} has been measured as 32.9 ± 2.0 yr [22]. The dramatic acceleration of the decay compared to 41.2 Gyr in standard conditions is due to bound - state β^- decay, where the decay electron is bound in the atomic K-shell of ^{187}Os^{75+}. Moreover at the high stellar temperatures, ^{187}Re decay could be drastically altered and even reversed; ^{187}Os electron capture (^{187}Os(e^-, ν_e)^{187}Re) is occurred. This should be studied in the framework of a full model for the Galactic chemical evolution [85]. Also for this treatment, a correction factor (F_λ (> 1.0) ; $\lambda_\beta^{\mathrm{eff}} = F_\lambda \times \lambda_\beta$) is used [80].

Astration during s-process in AGB stars can be treated with AGB stellar model calculation.

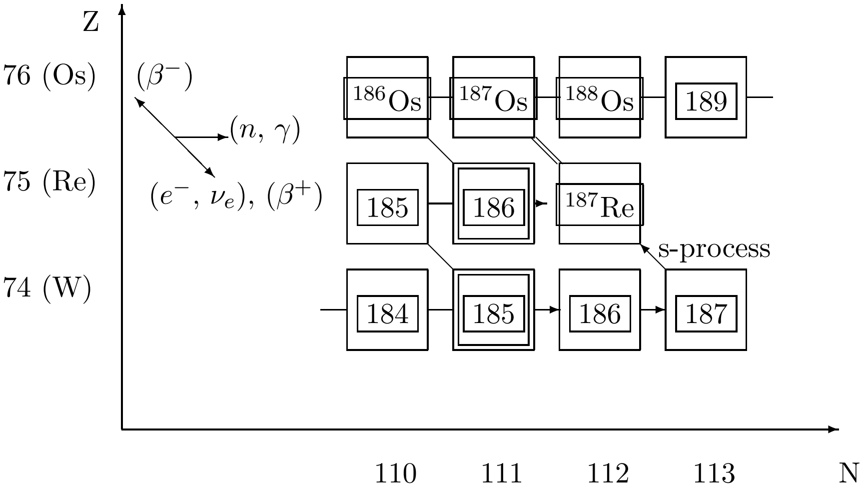

Figure 5.13: The branchings at ^{185}W and ^{186}Re. The line shows the main s-process path. The branching at ^{185}W gives the channel of ^{185}W$(n,\ \gamma)^{186}$W$(n,\ \gamma)^{187}$W(β-decay)^{187}Re. The branching at ^{186}Re gives the channel of ^{186}Re$(n,\ \gamma)$ ^{187}Re.

5.4.3 ^{187}Re production

For ^{187}Re production, the simple exponential model is applied. The reliable estimation of the time dependence for production rate of ^{187}Re requires a realistic model for GCE model.

5.4.4 Age estimation with AGB model calculation

The AGB stellar model calculation is performed with all parameters (MACS, SEF, β^+, β^- -decay rates) which are concerned in all the reaction network of s-process paths. The present calculation include n_TOF MACSs and SEF, the branching effect at ^{185}W and ^{186}Re and the temperature dependence of ^{187}Re β-decay rate. Thanks of this calculation [84], s-process yield fractions in terms of production factors respect to solar system are obtained; in particular the factor f_s in Eq. (5.1.1), MACS rate = s-process abundance rate of ^{186}Os and ^{187}Os is given (0.41 / 1.09). Using this f_s we can calculate Δ by the same way as Sec. 5.1 (Fowler model). For Δ we obtain the value of 9.88 ± 0.77 Gyr, and the age of the universe is given,

$$T_u = 14.94 \pm 0.77 \text{ Gyr.} \qquad \text{(Age -3)}$$

5.5 Summary of estimations from Re/Os clock

I showed ages estimated by three different modes using the present work results (MACSs and SEFs). These are shown in Table 5.10 with f_s, stellar cross section rates in Eq. (5.1.1). The first age (Age -1 in Sec. 5.1) is estimated by the original method, it needs corrections for stellar cross sections and other effects as mentioned.

Table 5.10: MACS rates (f_s) and evaluated time durations of nucleosynthesis (Δ) and the ages of the universe (T_u) from the present analysis.

Age	Model	f_s	Δ [Gyr]	T_u [Gyr]
1	Original [21]	0.427 ± 0.023	8.72 ± 0.77	13.78 ± 0.77
2	Original + SEF	0.339 ± 0.020	10.72 ± 0.72	15.78 ± 0.72
3	AGB model [84]	0.376 ± 0.023	9.88 ± 0.77	14.94 ± 0.77

In the present thesis, the accurate Os capture cross sections are reported. From these data, accurate MACSs are obtained. The corrections of MACSs for the stellar cross sections were established much better owing to developments of the theoretical calculation. All the procedure to obtain F_σ (SEF rate) is discussed in Sec. 5.2. Needless to say that $f_{s2} = F_\sigma \times f_{s1}$. The age obtained with SEF (Age -2 in Sec. 5.3) is 2 Gyr longer than the Age -1.

In Sec. 5.4 further applications are presented. Assuming $F_{b\lambda}$; $f_{s3} = F_{b\lambda} \times F_\sigma \times f_{s1}$, $F_{b\lambda}$ is obtained as 1.1. Age -3 is estimated using the results by means of the AGB stellar model calculation [84]. This is ~ 1 Gyr shorter than Age -2. The remained arguments in Sec. 5.4 are entrusted in a more realistic description of the GCE modelings.

5.6 Cosmochronometry

The dating of the universe can be obtained by means of various techniques. T_u, the ages of the universe obtained by the present Re/Os cosmochronometer analysis are compared to other methods. (See for instance at Fig. 5.6.)

Astronomical way

The age of universe is constrained by the age of its oldest known stellar components, the globular clusters. This is based on comparisons between the observed Hertzsprung-Russel (H-R), plot of the surface temperature of stars versus their luminosity, diagrams or color-magnitude diagram with theoretical diagrams, calculated as a function of time.

The classical method uses the luminosity of the stellar cluster main sequence turnoff (MSTO) point where the red giant branch starts [86].

White dwarfs cooling sequence (WDCS) is also used. Hotter white dwarfs are known to cool down more rapidly. The space density of white

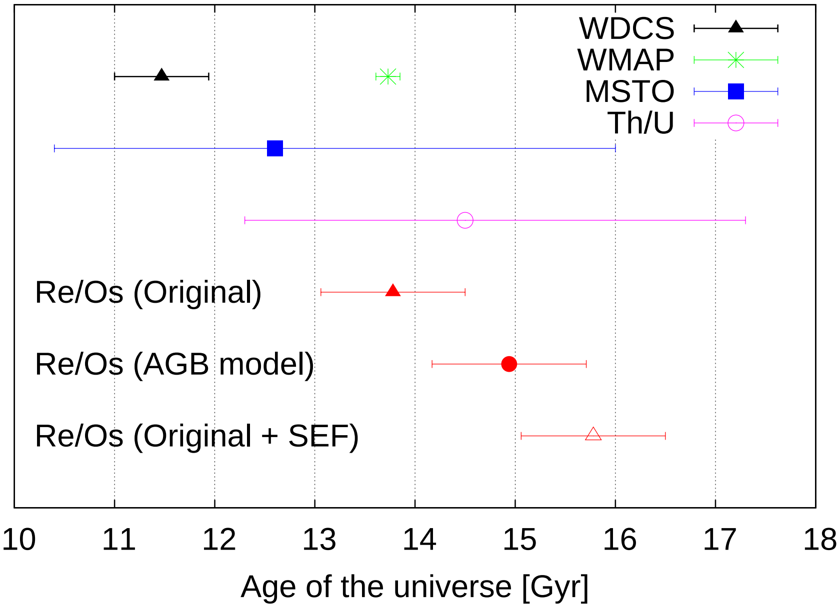

Figure 5.14: Age of the universe estimated from various methods. WDCS [87], WMAP [88], MSTO [86], Th/U [89], and Re/Os present works. See text for details.

dwarfs is therefore expected to increase monotonically with decreasing their luminosity [87].

Cosmological way

In this approach the age is obtained via observation of cosmic microwave background (CMB).

The Wilkinson Microwave Anisotropy Probe (WMAP) is Medium-Class Explorer satellite aimed at elucidating cosmology through full-sky observation of the CMB. Five-year's measurement data of WMAP gave Hubble constant $H = 70.1 \pm 1.3$ [(km/s)/Mpc] (one megaparsec (Mpc) is 3.26×10^6 light years) [88] and the age of the universe assumes the value $(1/H) = T_u = 13.73 \pm 0.12$ Gyr [88].

Nuclear physical way

The details of this approach are found in Subsec. 1.2.3. In addition to the present Re/Os clock results, U/Th ratio clock [89] is reported.

Assuming that the age from WMAP (13.73 ± 0.12 Gyr $\equiv T_u^{\mathrm{WMAP}}$) is the most reliable, the Re/Os value obtained in the pioneering work of Clayton [21] (Age -1) is in good agreement. However this original method is not a realistic model. The age including SEF (Age -2) is 2 Gyr longer than T_u^{WMAP}. The result that takes into account the AGB model calculation, considering SEF the s-process branching and the astration in AGB star (Age -3) is located between Age -1 and Age -2. This value is still 1 Gyr longer than the T_u^{WMAP}, however considering the uncertainty the difference is only ~ 0.5 Gyr.

Conclusions

The Re/Os abundance ratio can be used to make an estimation of the time-duration of the galactic nucleosynthesis and hence the age of universe. In order to perform the age estimation, the ^{186,187,188}Os capture cross section must be known with high accuracy in the neutron energy range of the RRR (resolved resonance region) and URR (un-resolved resonance region). In this thesis, the resonance analysis of these measurements and the implication on the Re/Os cosmochronometer are reported.

Capture cross sections of ^{186,187,188}Os were measured at CERN n_TOF (neutron time of flight). The pulsed neutron beam of the n_TOF facility is generated in spallation reactions in a massive lead target by 20 GeV protons. The resulting neutron spectrum runs from thermal energies up to 250 MeV. Two γ-ray detectors consisting of C_6D_6 liquid scintillator cells were used to detect the prompt γ-ray cascade following neutron capture events. The detectors were calibrated in regular intervals by means of reference sources.

Resonance parameter (resonance energy, radiative (γ) width and neutron width) analysis is completed up to 5.0 keV for ^{186}Os, 3.0 keV for ^{187}Os and 8.0 keV for ^{188}Os beyond any previous data. In total 865 resonances were analyzed (435 are new resonances). A statistical analysis of the resolved resonance parameters for the Os samples has been completed and the results are presented. Statistical averaged parameters (average level spacing, average radiative (γ) width and neutron strength function) are evaluated. Moreover contributions of these parameters to the HFSM (Hauser-Feshbach statistical model) calculation are investigated. In particular evaluated statistical averaged parameters are adopted to the HFSM in order to reproduce cross sections. For level density, average level spacings of the present analysis are inserted. Concerning average radiative (γ) width, which represents normalization for cross sections, discrepancies between evaluated values from present resonance parameters and the calculation parameters are observed.

Maxwellian average cross sections for the range of temperatures relevant for s-process nucleosynthesis have been derived from the combined information of the experimental data in the RRR and URR. For realistic cross sections in the stellar condition, SEF (stellar enhancement factor) is calculated by means of HFSM calculations. The implications of this analysis for the s-process component of ^{187}Os and the related estimation of the time-duration of the galactic nucleosynthesis through the Re/Os clock have been reported. Using a simple exponential model for the chemical enrichment of ^{187}Re over the galactic lifetime, we can estimate the impact of the capture cross section uncertainties on the nucleosynthesis time duration. This value turns out to be of the order of 0.5 Gyr. In other words, the uncertainty due to the nuclear physics input in the Re/Os clock can be presently estimated to be of the order of 0.5 Gyr.

As further applications, there are some arguments, astration, s-process branching and so on. AGB (Asymptotic Giant Branch) stellar models can evaluate effects of branchings and astration in AGB stars. Calculations including the n_TOF MACSs were performed. This showed that the branching at ^{185}W contributes the 10 % s-process production of ^{187}Re. In conclusion the evaluated age of universe with results from the AGB calculation is $\mathbf{14.94 \pm 0.77}$ Gyr. This is 1.21 Gyr longer than that obtained from WMAP (Wilkinson Microwave Anisotropy Probe) which could be the most reliable determination. Certainly a more realistic development of the GCE (Galactic Chemical Evolution) model will bring to advance in the Re/Os clock technique.

Appendix

Appendix A : Maxwellian averaged cross sections

Thermonuclear or stellar reaction rate are an essential input for nucleosynthesis models in nuclear astrophysics. This information is obtained from laboratory cross sections complemented by the effects of the stellar environment characteristic of the particular nucleosynthesis event.

For a capture reaction x(y,*)z, the thermally averaged reaction rate per unit volume is

$$r_{y,x} = n_y \cdot n_x \cdot \int_0^{\infty} \sigma(v) v dv = n_y \cdot n_x \cdot \langle \sigma v \rangle, \tag{A.1}$$

where n_i are the volume number densities of the reaction partners and $\sigma(v)$ the interaction cross section. The Maxwell-Boltzmann distribution for a certain temperature T is

$$\phi(v) = 4\pi v^2 \Big(\frac{m}{2\pi kT} \Big)^{3/2} \times \exp\Big(- \frac{mv^2}{2kT} \Big), \tag{A.2}$$

k being the Boltzmann constant.

The reaction rate can be derived by the convolution between the cross section $\sigma(E)$ and the Maxwell-Boltzmann distribution of the interaction particles in the stellar gas.

$$\begin{aligned} \langle \sigma v \rangle &= \int \int \phi(v_y) \phi(v_x) \sigma(v) dv_y dv_x \\ &= \Big(\frac{8}{\mu \pi} \Big)^{1/2} (kT)^{-2/3} \int_0^{\infty} E \sigma(E)_{y,x} \cdot \exp(-E/kT) dE, \end{aligned} \tag{A.3}$$

where μ denotes the reduced mass and v the center of mass velocity.

For neutron-induced reactions there is no Coulomb barrier. In the temperature range of hydrogen and helium burning scenarios the cross sections exhibit essentially a $1/v$ behavior due to the dominance of s-wave capture.

$$\sigma_{n,x} \ \propto \ \frac{\Gamma_n}{E} \ \propto \ \frac{1}{\sqrt{E}} \ \propto \ \frac{1}{v}. \tag{A.4}$$

This relation, which follows from the Breit-Wigner formula (see Sec. 1.4.2), the behavior of the reduced neutron width (see Subsec. 1.4.5), and $E = (1/2)mv^2$, results in a constant reaction rate $N_A \langle \sigma v \rangle \propto N_A \ \langle (1/v) \cdot v \rangle$. Using the mean thermal velocity $v_T = \sqrt{2kT/\mu}$, one obtains Maxwellian averaged cross section (MACS),

$$\langle \sigma \rangle = \frac{\langle \sigma v \rangle}{v_T} = \frac{2}{\sqrt{\pi}} \frac{\int_0^{\infty} \sigma(E_n) \cdot E_n \cdot \exp(-E_n/kT) dE_n}{\int_0^{\infty} E_n \cdot \exp(-E_n/kT) dE_n}, \tag{A.5}$$

where E_n is the neutron kinetic energy in the center-of-mass system. A comprehensive MACS data base *KADONIS* is available on line [90].

Appendix B : S-process abundances

The time dependence of the abundance N_A is given by

$$\frac{dN_A(t)}{dt} = N_n(t)N_{A-1}(t)\langle\sigma v\rangle_{A-1} - N_n(t)N_A(t)\langle\sigma v\rangle_A - \lambda_\beta(t)N_A(t). \quad \text{(B.1)}$$

$N_n(t)$ is the neutron density. λ_β is the β-decay rate. With the definition of the MACS (Appendix A) and neutron flux $\phi_n(t)$,

$$\langle\sigma\rangle = \frac{\langle\sigma v\rangle_A}{v_T} = \frac{\int \sigma(E)\phi_n(E)dE}{\int \phi_n(E)dE} \quad \rightarrow \quad \langle\sigma v\rangle_A = v_T\langle\sigma\rangle_A, \quad \text{(B.2)}$$

and assuming that
i) temperature ($T(t)$) constant and
ii) the β decay beings much faster than neutron capture ($\tau_\beta \gg \tau_{n,\gamma}$),
Equation (B.1) can be simplified

$$\frac{dN_A}{dt} = v_T N_n(t)(\langle\sigma\rangle_{A-1}N_{A-1} - \langle\sigma\rangle_A N_A). \quad \text{(B.3)}$$

By defining a time-integrated neutron flux,

$$\tau = \int_0^t \phi_n(t^{'})dt^{'} = v_T \int_0^t N_n(t)dt, \quad \text{(B.4)}$$

Eq. (B.3) becomes

$$\frac{dN_A}{d\tau} = \langle\sigma\rangle_{A-1}N_{A-1} - \langle\sigma\rangle_A N_A. \quad \text{(B.5)}$$

If flow equilibrium in the reaction chain along the s-process path is reached, $dN_A/d\tau = 0$, leading to

$$\langle\sigma\rangle_{A-1}N_{A-1} = \langle\sigma\rangle_A N_A = \text{constant}. \quad \text{(B.6)}$$

Assuming a continuous, exponential distribution of neutron exposures

$$\rho(\tau) = \frac{G \cdot N_{56}^{\odot}}{\tau_0}\exp(-\tau/\tau_0), \quad \text{(B.7)}$$

where G is the fraction of the ^{56}Fe abundance required as the s-process seed, $N_{56}^{\odot}$ is the solar ^{56}Fe abundance, and τ_0 is the mean neutron exposure in units of mb^{-1}. The solution of the coupled system of equations [9] is

$$\langle\sigma\rangle_A N_A = \frac{\langle\sigma\rangle_{A-1}N_{A-1}}{1 + 1/\tau_0\langle\sigma\rangle_A} = \frac{G \cdot N_{56}^{\odot}}{\tau_0}\prod_{i=56}^{A}\left(1 + \frac{1}{\tau_0\langle\sigma\rangle_i}\right)^{-1}. \quad \text{(B.8)}$$

Apart from the parameters G and τ_0 which are common for all species, the only remaining input parameter for this expression is the stellar (n,γ) cross sections $\langle\sigma\rangle$.

Appendix C : Reich-Moore approximation

For a given entrance channel c leading to an exit channel c', the angle integrated partial neutron cross section $\sigma_{cc'}$ is given as:

$$\sigma_{cc'} = \pi \lambda\!\!\!^{-2} g_c \mid \delta_{cc'} - U_{cc'} \mid^2, \tag{C.1}$$

where $\pi \lambda\!\!\!^{-2} g$ is same as Breit-Wigner formula (Subsec. 1.4.3). The scattering matrix $U_{cc'}$ can be written in terms of the W matrix as :

$$U_{cc'} = \Omega_l W_{cc'} \Omega_l', \qquad \text{with} \qquad \Omega_l = \mathrm{e}^{-\mathrm{i}\varphi_\mathrm{l}}. \tag{C.2}$$

The W matrix is related to the R-matrix via

$$W = P^{1/2}(I - RL)^{-1}(I - RL^*)P^{1/2} \quad \text{with} \quad L = (S - B) + iP. \tag{C.3}$$

The quantity I is the identity matrix. P is the penetration factor, S the shift factor and B the arbitrary boundary constant at the channel radius a_c. R is the R-matrix. For all binary reactions, the cross section can be described by the R-matrix theory. Also the R-matrix theory can be applied to cross section data in the RRR [42].

The Reich-Moore approximation neglects the off-diagonal contribution of photon channels. In this treatment, the R-matrix has the form

$$R_{cc'} = \sum_\lambda \frac{\gamma_{\lambda c}\gamma_{\lambda c}}{E_\lambda - E - i\Gamma_{\lambda\gamma}/2}\delta_{JJ'}, \tag{C.4}$$

where E_λ presents the energy of the resonance and the reduced width amplitude γ is related to the partial width Γ by $\Gamma_{\lambda c} = 2\mathbf{P_c}\gamma_{\lambda c}^2$. $\mathbf{P_c}$ is the penetrability. The final formula of capture cross section is

$$\sigma_{\mathrm{capture}}(E) = 4\pi\lambda\!\!\!^{-2} \sum_J g_{Ja} \sum_{\mathrm{incident\ channel}} \left[X_{cc'} - \sum_{\mathrm{all-ch}} X_{cc'}^2 + X_{cc'}^2 \right], \tag{C.5}$$

where X is defined by $X = P^{1/2}L^{-1}(L^{-1} - R)^{-1}RP^{1/2}$.

Appendix D : n_TOF resolution function

Researchers at Rensselaer Polytechenic Institute (RPI) have carefully developed the resolution function. The RPI resolution function has been extended for n_TOF and GELINA.

The resolution-broadened cross section $\bar{\sigma}(t)$ may be expressed as

$$\bar{\sigma}(t) = \int I(t-t')\sigma(t')dt', \tag{D.1}$$

t is the neutron time of flight (the flight path L) that is converted to the neutron energy E with $E = (1/2)m \times (L/t)^2$. Where the resolution function $I(t-t')$ is convoluted with independent components and defined as

$$I(t-t') = \int I_1(t-t_1)dt_1 \int I_2(t_1-t_2)dt_2 \cdot I_3(t_2-t'). \tag{D.2}$$

I_1 is the Electron burst term. For the capture ($E < 1$ MeV) of n_TOF, this is not included.

I_2 is the target plus detector term,

$$I_2(t) = A_0\left\{\frac{(t+\tau)^2}{2!\Lambda^3}\mathrm{e}^{-\frac{(t+\tau)}{\Lambda}} + \mathrm{A_1}\left[\mathrm{A_2}\cdot\mathrm{e}^{-\mathrm{A_3(t+t_0)}} + \mathrm{A_4}\cdot\mathrm{e}^{-\mathrm{A_5(t+t_0)}}\right]\mathrm{X(t)}\right\} \tag{D.3}$$

in which the function $X(t)$ is zero when $t+\tau < 0$, and unity otherwise. The value of A_0 is chosen to give an overall normalization of unity for this function. Other parameters are functions of the energy, the specific forms are respectively

$$\begin{aligned} \Lambda(E) &= \Lambda_0 + \Lambda_1\mathrm{ln(E)} + \Lambda_2[\mathrm{ln(E)}]^2 + \Lambda_3\mathrm{E}^{\Lambda_4}, \\ \tau(E) &= \tau_1 e^{-\tau_2 E} + \tau_3 e^{-\tau_4 E} + \tau_5 + \tau_6 E^{\tau_7}, \\ A_i(E) &= \left(a_{i1}e^{-a_{i2}E} + a_{i3}e^{-a_{i4}E} + a_{i5} + a_{i6}E^{a_{i7}}\right)\alpha_i. \\ &\left\{\begin{array}{ll} i=1 & \alpha_1 : 1 \\ i=3,\ 5 & \alpha_i : \text{unity or } \sqrt{E} \end{array}\right. \end{aligned} \tag{D.4}$$

The parameters for n_TOF resolution functions are listed in Table D.1. I_3 is the term of the time of flight channel width,

$$I_3(t) = \left\{\begin{array}{ll} 1/c & \text{for } -(c/2) < t < (c/2) \\ 0 & \text{otherwise} \end{array}\right. \tag{D.5}$$

For constant value of c within an energy range, in n_TOF case, the channel width (or bin width) is expressed as n bins per decade. When n is large $\sim$ 5000, it can be used the approximation $c \cong t{\cdot}\ln(10)/(2n)$. Present Os data are formed $n = 4000$ and 8000.

For n_TOF resolution function for I_2, the Monte carlo simulations were performed (Fig. D.1) and the parameters are shown in Table D.1.

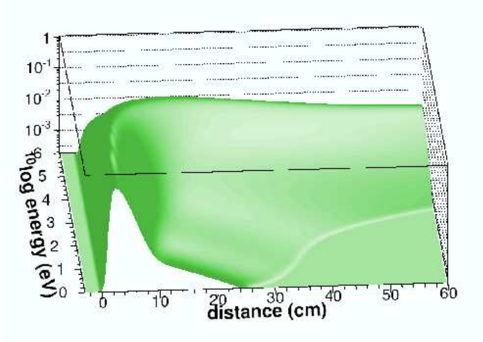

Figure D.1: n_TOF resolution function simulation fit [91].

Table D.1: Parameters of n_TOF resolution function [42]. Parameters not listed here have value zero.

Parameter	n_TOF value	Units
τ_5	-3.7004	ns
τ_6	-684.39	ns
τ_7	-0.5189	-
Λ_0	3.8457	ns
Λ_3	502.9930	ns
Λ_4	-0.4155	-
a_1	-0.381	$(\mathrm{ns})^{-1}$
a_2	9.974×10^{-6}	$(\mathrm{eV})^{-1}$
a_3	-0.01172	$(\mathrm{ns})^{-1}$
a_4	-0.381	$(\mathrm{eV})^{-1}$
a_5	1.019×10^{-4}	$(\mathrm{ns})^{-1}$
A_2	1.0	-
A_4	-1.0	-
a_{35}	-1.689×10^{-4}	$(\mathrm{ns} \times\sqrt{eV})^{-1}$
a_{36}	4.254×10^{-4}	$(\mathrm{ns} \times\sqrt{eV})^{-1}$
a_{37}	-0.06043	-
a_{55}	2.766×10^{-4}	$(\mathrm{ns} \times\sqrt{eV})^{-1}$

Appendix E : n_TOF ^{186,187,188}Os resonance parameters

Resonance parameters (RP) of extracted from the n_TOF data are listed in the following. There are two tables for each sample.

In the first table, the resonance energy(: E), the radiative(γ) width(: Γ_γ) and the neutron width (: Γ_n) multiplied by the spin statistical factor g (see Subsec. 1.4.5) are listed.

In the second table of a sample, new found resonances are reported. In particular n_TOF allowed for the investigation of new resonances for energies higher than 3.4 keV (^{186}Os), 1.0 keV (^{187}Os) and 4.96 keV (^{188}Os) respectively. Since for these new resonance I had not the possibility to access to the neutron width [44], the **kernel**,

$$\frac{g(\Gamma_\gamma \times \Gamma_n)}{(\Gamma_\gamma + \Gamma_n)} \quad \equiv K \tag{E.1}$$

is reported in the table.

All resonance spin is assigned as s-wave ($l = 0$) (see Sec. 1.4.5). For ^{186}Os and ^{188}Os there is one spin group, $l = 0$, $J = 1/2$. For ^{187}Os, there are two spin groups, $J = 0$ ($g = 1/4$) and $J = 1$ ($g = 3/4$). In the present analysis, spin group determinations are not done.

The parameters are shown as A(B). B is the uncertainty on these values from the SAMMY output. The forms 11.11(1), 11.111(11) show that the uncertainties are 0.01 and 0.011 respectively. (0) means that the value is fixed.

Table E.1: Resonance parameters of ^{186}Os -1

E[eV]	Γ_γ[meV]	$g\Gamma_n$[meV]
22.28(0)		
44.80(0)		
66.25(0)		
89.72(0)		
108.83(1)	50.0(0.0)	0.35(0.01)
137.886(3)	41.7(0.3)	435.0(0.0)
145.28(1)	50.0(0.0)	1.5(0.1)
169.797(2)	50.0(0.0)	5.3(0.0)
201.995(3)	50.0(0.0)	114.1(1.0)
249.642(3)	50.0(0.0)	13.5(0.2)
273.10(1)	50.0(0.0)	2.08(0.04)
281.21(1)	40.3(0.4)	181.3(2.4)
313.531(4)	34.1(0.5)	85.6(1.8)
342.80(2)	42.9(0.6)	673.8(0.0)
370.14(1)	39.2(0.5)	225.8(4.1)
380.25(1)	36.0(0.5)	189.5(3.9)
417.06(1)	37.9(0.5)	77.7(2.6)
423.39(1)	34.6(0.5)	187.7(3.2)
452.32(1)	50.0(0.0)	19.6(0.4)
521.36(1)	50.0(0.0)	272.7(4.9)
568.26(1)	32.4(0.5)	243.1(0.0)
604.93(1)	50.0(0.0)	157.6(4.3)
635.17(1)	50.0(0.0)	281.7(5.9)
643.95(2)	39.8(0.7)	509.0(0.0)
655.66(1)	40.5(0.8)	462.2(0.0)
680.16(2)	46.8(0.8)	342.1(0.0)
736.35(2)	50.0(0.0)	13.7(0.4)
763.50(1)	50.0(0.0)	174.3(8.1)
797.17(1)	50.0(0.0)	50.5(2.1)
837.71(2)	43.8(0.8)	362.0(0.0)
846.18(1)	50.0(0.0)	37.2(1.3)
869.15(4)	38.1(0.9)	724.5(0.0)
891.71(1)	50.0(0.0)	292.2(8.8)
916.01(3)	50.0(0.0)	5.8(0.3)
962.84(7)	43.6(1.1)	1611.(0.)
980.83(3)	41.5(1.1)	819.3(0.0)
1024.38(2)	50.9(0.8)	345.0(0.0)
1038.04(2)	46.7(0.8)	371.0(0.0)
1073.72(2)	49.3(1.4)	73.0(0.0)
1106.31(1)	50.0(0.0)	6.6(1.1)
1171.06(2)	50.0(0.0)	19.1(0.6)
1205.01(2)	50.0(0.0)	39.6(1.4)
1216.03(6)	50.0(0.0)	4.7(0.3)
1224.58(2)	50.0(0.0)	38.5(1.5)
1228.76(3)	36.5(0.9)	556.1(0.0)
1244.27(1)	50.0(0.0)	84.7(4.0)
1264.70(2)	50.0(0.0)	57.2(2.5)
1298.61(3)	55.0(1.0)	855.0(0.0)
1324.42(2)	44.0(1.0)	600.0(0.0)
1344.79(1)	50.0(0.0)	5.5(1.0)
1359.99(6)	56.2(1.3)	1750.(0.)
1402.92(6)	50.0(0.0)	5.1(0.3)
1405.29(1)	50.0(0.0)	4.4(0.8)
1462.99(2)	45.9(0.9)	311.0(0.0)
1476.90(2)	50.0(0.0)	77.5(4.8)
1504.44(2)	54.5(1.2)	169.0(0.0)
1529.16(1)	50.0(0.0)	13.0(2.1)
1559.55(4)	50.0(0.0)	10.1(0.4)
1597.45(3)	47.9(1.3)	139.0(0.0)
1626.87(3)	53.3(1.1)	489.0(0.0)
1674.85(1)	50.0(0.0)	107.5(16.0)
1687.37(2)	50.0(0.0)	64.4(6.1)
1713.66(3)	50.0(0.0)	168.0(0.0)
1742.42(3)	50.0(0.0)	49.9(7.6)
1748.28(3)	43.9(1.2)	413.1(0.0)
1790.23(2)	50.0(0.0)	15.7(3.0)
1797.56(4)	50.0(0.0)	23.7(1.1)
1821.70(3)	50.0(0.0)	109.3(10.9)
1860.11(3)	59.4(1.9)	130.0(0.0)
1876.08(3)	50.0(0.0)	3.6(0.7)
1919.51(3)	53.4(1.7)	113.0(0.0)
1936.88(4)	50.0(0.0)	29.1(1.5)
1957.36(2)	45.4(1.7)	253.0(0.0)
1971.87(10)	50.0(0.0)	5.4(0.4)

^{186}Os -1

E[eV]	Γ_γ[meV]	$g\Gamma_n$[meV]
1991.27(5)	38.8(1.2)	383.0(0.0)
2018.32(6)	50.0(0.0)	11.5(0.7)
2065.90(4)	56.7(1.4)	304.0(0.0)
2091.47(4)	51.6(1.5)	236.0(0.0)
2137.45(7)	50.0(0.0)	7.8(1.0)
2167.41(4)	55.1(1.7)	148.0(0.0)
2186.45(1)	50.0(0.0)	7.5(1.5)
2201.59(5)	50.0(0.0)	73.0(0.0)
2221.28(5)	50.0(0.0)	78.0(0.0)
2229.25(5)	43.8(1.5)	564.0(48.3)
2273.50(1)	50.0(0.0)	49.4(8.4)
2301.71(6)	53.3(1.8)	475.0(0.0)
2309.52(5)	52.3(2.0)	226.0(0.0)
2313.20(5)	45.6(1.8)	207.0(0.0)
2373.94(5)	53.1(1.5)	635.0(0.0)
2391.11(3)	48.9(1.6)	320.0(0.0)
2432.34(1)	50.0(0.0)	5.1(1.0)
2439.71(6)	45.8(1.6)	996.0(0.0)
2473.25(5)	56.4(2.0)	242.0(0.0)
2489.42(1)	50.0(0.0)	67.8(11.0)
2538.42(6)	50.0(0.0)	94.0(0.0)
2586.98(6)	50.3(1.6)	651.0(0.0)
2597.51(10)	50.0(0.0)	12.0(0.9)
2626.71(8)	50.0(0.0)	78.0(9.5)
2655.50(7)	50.0(0.0)	53.0(4.4)
2660.57(8)	47.2(2.2)	835.4(84.5)
2666.76(1)	50.0(0.0)	8.5(1.6)
2733.89(6)	56.9(1.8)	341.0(0.0)
2748.05(7)	50.0(0.0)	147.4(19.8)
2765.52(6)	50.0(0.0)	118.6(12.3)
2807.33(6)	60.5(2.0)	765.0(0.0)
2821.50(6)	62.7(2.2)	471.0(0.0)
2852.17(6)	55.1(6.3)	72.3(11.0)
2882.23(6)	60.4(2.5)	167.0(0.0)
2907.66(9)	53.4(1.9)	994.0(0.0)
2935.10(7)	50.0(0.0)	141.6(18.4)
2941.75(3)	50.0(0.0)	10.3(2.0)
2960.70(7)	55.2(3.0)	144.5(27.3)
2968.82(6)	47.6(2.0)	275.0(0.0)
2990.61(8)	52.3(3.4)	71.0(0.0)
3036.00(10)	50.0(0.0)	27.7(2.2)
3059.97(6)	51.8(2.1)	179.0(0.0)
3102.31(7)	51.1(1.9)	359.0(0.0)
3118.60(7)	45.1(1.8)	235.0(0.0)
3138.71(7)	49.0(2.0)	235.0(0.0)
3197.47(2)	53.3(10.3)	20.9(4.1)
3207.88(7)	55.2(2.5)	231.0(0.0)
3218.33(6)	61.7(2.7)	167.0(0.0)
3250.78(23)	50.0(0.0)	2690.(0.)
3317.97(9)	50.0(0.0)	160.4(23.7)
3338.33(8)	58.5(2.5)	268.0(0.0)
3356.35(13)	49.7(2.2)	1230.(0.)

^{186}Os -1

^{186}Os -1 (Table E.1)

All spins defined as s-wave, l=0, J=0.5 (g=1).

Table E.2: Resonance parameters of ^{186}Os -2

E[eV]	Kernel[meV]
3419.15(01)	14.9(2.9)
3434.5(1)	22.8(1.9)
3460.6(1)	44.2(7.0)
3489.9(1)	31.6(5.6)
3510.8(1)	44.6(7.0)
3521.6(2)	8.3(0.9)
3537.6(1)	48.8(0.0)
3549.1(1)	39.1(5.7)
3579.7(1)	35.0(4.4)
3647.7(1)	47.4(0.0)
3662.6(1)	40.3(7.6)
3681.4(1)	47.1(6.4)
3687.20(03)	14.8(2.9)
3690.54(01)	31.4(5.9)
3725.3(1)	35.2(4.1)
3742.4(1)	47.1(0.0)
3793.53(01)	33.6(6.5)
3807.9(2)	34.5(6.2)
3847.2(1)	43.2(8.0)
3857.6(3)	8.0(1.3)
3866.1(1)	21.2(3.6)
3884.0(1)	41.7(6.7)
3925.83(01)	40.7(6.4)
3978.06(01)	16.0(3.2)
3995.5(1)	31.8(3.8)
4015.4(1)	45.0(7.2)
4026.7(1)	47.0(6.6)
4055.6(2)	11.0(1.9)
4071.2(2)	44.0(8.3)
4085.5(1)	41.4(6.5)
4142.7(1)	43.3(7.3)
4191.4(1)	30.0(3.6)
4236.3(2)	47.2(0.0)
4264.83(05)	19.8(3.5)
4296.7(1)	43.5(7.6)
4325.5(1)	44.3(7.7)
4342.8(2)	46.4(8.1)
4376.71(02)	42.0(7.0)
4401.9(2)	15.7(1.9)
4414.6(2)	42.6(7.8)
4424.6(2)	41.6(7.0)
4454.0(2)	35.7(5.3)
4494.0(2)	38.1(5.7)
4523.00(01)	28.2(5.4)
4539.6(3)	35.7(5.8)
4579.7(2)	44.6(8.4)
4630.1(2)	44.9(9.1)
4632.6(2)	44.0(7.3)
4648.2(1)	43.7(7.9)
4673.69(02)	11.0(2.2)
4695.9(2)	42.6(8.8)
4706.9(1)	42.7(7.7)
4747.0(2)	48.6(5.9)
4778.8(1)	40.3(6.4)
4846.2(2)	45.4(7.9)
4881.6(2)	45.2(7.8)
4892.2(2)	42.8(7.5)
4917.3(1)	36.6(6.9)
4967.9(1)	38.0(6.7)
4983.8(2)	45.5(7.5)

^{186}Os -2

^{186}Os -2 (Table E.2)

All spins defined as s-wave, l=0, J=0.5 (g=1).

Table E.3: Resonance parameters of ^{187}Os -1

E[eV]	Γ_γ[me])	$g\Gamma_n$[meV]
9.479(0)		
12.700(0)		
20.230(0)		
26.351(1)	61.0(0.0)	0.25(0.00)
28.322(2)	61.0(0.0)	0.15(0.00)
39.550(0)	61.0(0.0)	0.91(0.01)
40.567(1)	61.0(0.0)	10.27(0.04)
43.455(1)	61.0(0.0)	11.07(0.05)
47.815(1)	61.0(0.0)	12.51(0.00)
50.160(0)	61.0(0.0)	25.00(0.00)
50.600(0)	61.0(0.0)	1.95(0.00)
62.188(1)	61.0(0.0)	4.50(0.00)
63.846(1)	42.7(0.4)	23.75(0.00)
65.092(2)	61.0(0.0)	1.00(0.01)
71.467(2)	61.0(0.0)	0.77(0.01)
78.050(0)	61.0(0.0)	1.88(0.00)
83.360(0)	61.0(0.0)	0.53(0.01)
89.975(1)	40.3(0.6)	27.51(0.37)
92.897(1)	61.0(0.0)	11.19(0.09)
99.333(2)	61.1(0.7)	20.32(0.24)
105.004(2)	61.0(0.0)	7.07(0.09)
108.853(1)	57.3(0.5)	129.1(0.8)
110.378(5)	61.0(0.0)	1.27(0.02)
114.695(3)	61.0(0.0)	0.90(0.01)
118.980(13)	61.0(0.0)	0.15(0.01)
123.060(0)	61.0(0.0)	4.34(0.05)
124.416(2)	53.1(0.6)	125.5(0.0)
126.944(1)	61.0(0.0)	53.26(0.00)
132.153(6)	61.0(0.0)	0.56(0.01)
138.281(2)	54.4(0.4)	122.1(0.0)
145.076(2)	61.0(0.0)	50.96(0.41)
155.446(2)	61.0(0.0)	6.06(0.06)
164.349(2)	61.0(0.0)	16.65(0.21)
168.371(2)	61.0(0.0)	11.17(0.12)
171.311(2)	61.0(0.0)	2.75(0.04)
175.748(2)	61.0(0.0)	10.87(0.15)
176.985(3)	59.0(1.7)	77.44(1.63)
178.418(3)	61.0(0.0)	8.49(0.09)
188.942(2)	61.0(0.0)	9.17(0.10)
196.807(26)	61.0(0.0)	0.24(0.02)
201.005(3)	61.0(0.0)	11.22(0.14)
207.003(4)	61.0(0.0)	27.50(0.00)
211.469(4)	61.0(0.0)	6.30(0.10)
213.366(13)	61.0(0.0)	206.3(0.0)
213.591(10)	61.0(0.0)	281.3(0.0)
217.675(4)	61.0(0.0)	4.95(0.08)
226.023(3)	52.9(0.6)	59.97(1.08)
227.858(3)	61.0(0.0)	17.06(0.21)
233.635(3)	61.0(0.0)	8.04(0.10)
236.033(2)	56.2(0.6)	112.0(0.0)
244.889(4)	61.0(0.0)	6.86(0.09)
250.320(3)	43.6(0.4)	125.1(1.6)
253.272(5)	61.0(0.0)	5.23(0.08)
267.599(4)	61.0(0.0)	9.54(0.13)
269.749(5)	61.0(0.0)	9.10(0.17)
273.270(6)	61.0(0.0)	1.86(0.18)
283.822(18)	61.0(0.0)	0.60(0.05)
288.681(3)	61.0(0.0)	26.94(0.48)
296.005(4)	61.0(0.0)	10.68(0.16)
297.651(5)	61.0(0.0)	8.53(0.14)
310.672(8)	61.0(0.0)	6.78(0.20)
315.757(6)	61.0(0.0)	21.74(0.47)
328.800(5)	61.0(0.0)	16.38(0.29)
330.393(3)	61.0(0.0)	8.80(0.16)
334.430(2)	61.0(0.0)	11.71(0.25)
338.904(4)	61.0(0.0)	39.59(0.77)
345.618(16)	61.0(0.0)	3.02(0.09)
346.891(5)	61.0(0.0)	18.31(0.34)
350.903(5)	61.0(0.0)	32.20(0.66)
369.115(6)	61.0(0.0)	25.57(0.54)
371.890(4)	61.0(0.0)	13.31(1.13)
375.223(4)	61.0(0.0)	6.20(0.20)
382.312(6)	61.0(0.0)	16.05(0.74)
390.254(6)	61.0(0.0)	90.01(0.00)

^{187}Os -1

E[eV]	Γ_γ[meV]	$g\Gamma_n$[meV]	E[eV]	Γ_γ[meV]	$g\Gamma_n$[meV]
391.683(9)	61.0(0.0)	10.38(0.21)	628.15(1)	61.0(0.0)	42.8(1.6)
398.565(4)	64.1(1.0)	73.50(0.00)	636.83(1)	61.0(0.0)	11.9(0.3)
403.624(9)	39.6(1.5)	99.97(0.00)	638.29(1)	61.0(0.0)	29.8(0.9)
404.880(0)	61.0(0.0)	12.39(0.34)	640.12(1)	61.0(1.3)	81.0(0.0)
408.307(5)	61.0(0.0)	300.2(0.0)	648.63(3)	61.0(0.0)	3.6(0.4)
419.237(13)	61.0(0.0)	4.07(0.13)	657.20(1)	61.0(0.0)	23.0(0.7)
423.867(44)	61.0(0.0)	0.72(0.06)	664.79(1)	61.0(0.0)	18.8(1.3)
425.911(4)	61.0(0.0)	6.46(0.44)	668.87(1)	61.0(0.0)	7.1(0.2)
431.463(8)	61.0(0.0)	38.36(1.73)	675.05(2)	61.0(0.0)	3.9(0.1)
441.858(7)	76.4(1.3)	79.54(0.00)	678.43(1)	61.0(0.0)	31.9(2.0)
447.480(20)	61.0(0.0)	1.53(0.08)	682.12(2)	61.0(0.0)	7.7(0.2)
453.322(6)	61.0(0.0)	43.88(1.11)	687.15(1)	61.0(0.0)	26.9(1.8)
462.381(6)	61.0(0.0)	34.13(1.04)	692.63(4)	61.0(0.0)	2.7(0.4)
468.304(11)	61.0(0.0)	7.76(0.23)	693.38(1)	61.0(0.0)	6.2(1.1)
472.509(10)	61.0(0.0)	10.34(0.21)	698.05(1)	61.0(0.0)	45.8(1.6)
483.500(7)	54.6(1.0)	102.0(0.0)	702.18(1)	58.9(1.2)	109.5(0.0)
497.703(8)	61.0(0.0)	19.45(0.44)	710.25(1)	61.0(0.0)	23.1(0.6)
504.88(1)	61.0(0.0)	13.5(0.3)	716.05(1)	61.0(0.0)	24.0(0.7)
539.46(1)	61.0(0.0)	14.3(0.6)	718.00(1)	61.0(0.0)	27.8(0.7)
542.19(1)	61.0(0.0)	15.6(0.4)	727.87(1)	61.0(0.0)	31.4(0.9)
543.70(1)	61.0(0.0)	11.0(0.3)	733.60(2)	61.0(0.0)	15.4(0.4)
547.66(1)	61.0(0.0)	11.7(0.3)	737.19(1)	61.0(0.0)	45.0(1.5)
548.86(2)	61.0(0.0)	4.1(0.2)	750.12(1)	61.8(1.7)	75.8(0.0)
552.40(1)	53.0(2.4)	38.0(4.7)	753.72(1)	61.0(0.0)	36.1(1.7)
554.15(1)	57.9(1.3)	190.6(5.0)	757.43(2)	61.0(0.0)	30.0(1.4)
572.28(1)	58.6(1.1)	64.0(0.0)	759.00(3)	61.0(0.0)	15.8(0.7)
582.41(1)	61.0(0.0)	15.2(1.3)	760.79(2)	55.5(1.5)	285.0(0.0)
587.04(1)	64.5(1.5)	72.0(0.0)	769.28(1)	61.0(0.0)	14.3(0.5)
589.00(0)	61.0(0.0)	2.9(0.1)	771.18(1)	61.0(0.0)	45.1(3.5)
592.68(1)	56.7(1.0)	80.5(0.0)	777.48(1)	61.0(0.0)	34.6(0.9)
594.70(0)	61.0(0.0)	6.0(0.2)	784.46(1)	66.6(1.6)	85.0(0.0)
598.13(1)	61.0(0.0)	19.2(0.5)	791.74(1)	73.2(1.8)	83.0(0.0)
599.92(1)	65.0(0.0)	10.7(0.2)	794.10(2)	61.0(0.0)	10.0(0.4)
606.80(1)	61.0(0.0)	33.5(0.9)	799.56(2)	73.6(2.3)	115.5(0.0)
608.43(2)	61.0(0.0)	6.6(0.4)	801.84(3)	61.0(0.0)	6.9(0.3)
610.52(1)	61.0(0.0)	63.1(2.4)	804.67(1)	61.0(0.0)	192.6(8.6)
622.99(1)	61.0(0.0)	25.0(0.6)	810.27(1)	53.7(3.0)	81.0(0.0)
625.25(1)	61.0(0.0)	33.9(1.0)	826.11(2)	61.0(0.0)	18.3(0.5)
^{187}Os -1			^{187}Os -1		

E[eV]	Γ_γ[meV]	$g\Gamma_n$[meV]
831.27(1)	61.0(0.0)	53.1(2.3)
838.09(2)	61.0(0.0)	16.7(0.6)
840.15(2)	61.0(0.0)	23.8(1.0)
842.67(4)	61.0(0.0)	6.5(0.7)
847.67(2)	65.7(1.6)	397.8(10.3)
853.76(2)	61.0(0.0)	3.2(0.2)
867.96(2)	52.0(1.8)	80.0(0.0)
871.68(1)	63.7(1.6)	80.0(0.0)
878.45(1)	61.0(0.0)	27.6(0.9)
882.89(2)	61.0(0.0)	10.2(1.0)
884.58(2)	61.0(0.0)	12.4(0.4)
889.53(1)	61.0(0.0)	27.4(0.8)
896.36(1)	61.0(0.0)	12.0(0.8)
906.01(3)	61.0(0.0)	9.0(0.5)
910.61(2)	61.0(0.0)	14.6(1.5)
916.65(2)	75.6(1.7)	195.0(0.0)
919.36(2)	70.6(1.8)	104.0(0.0)
929.09(2)	61.0(0.0)	54.3(3.7)
929.70(4)	61.0(0.0)	72.5(0.0)
940.53(1)	62.3(2.0)	150.0(0.0)
942.19(5)	54.7(3.1)	115.0(0.0)
947.10(1)	74.3(2.3)	63.5(0.0)
953.37(3)	59.9(2.1)	93.5(0.0)
957.73(2)	61.0(0.0)	35.4(1.8)
962.15(8)	61.0(0.0)	3.1(0.3)
964.29(2)	61.0(0.0)	77.0(4.6)
975.77(1)	65.0(0.0)	10.4(1.3)
981.44(1)	61.0(0.0)	50.0(0.0)
986.83(4)	61.0(0.0)	11.6(0.8)
989.71(2)	62.7(2.1)	75.0(0.0)

^{187}Os -1 (Table E.3)

All spins defined as s-wave (l=0).

Table E.4: Resonance parameters of ^{187}Os -2

E[eV]	K[meV]
1006.01(2)	36.0(2.4)
1016.48(3)	11.4(1.3)
1022.48(2)	38.7(2.2)
1030.45(2)	16.5(0.6)
1035.96(1)	6.7(1.2)
1039.21(1)	3.0(0.6)
1043.45(4)	9.2(0.9)
1050.62(2)	37.4(2.6)
1053.21(2)	22.9(1.0)
1064.60(3)	9.0(0.6)
1069.62(3)	9.5(0.4)
1072.37(2)	36.9(2.0)
1078.42(4)	5.4(0.3)
1089.02(1)	20.7(2.5)
1095.21(1)	27.5(1.0)
1100.02(2)	19.4(0.8)
1104.06(3)	11.0(0.4)
1114.34(2)	39.9(1.7)
1122.43(3)	14.0(0.7)
1135.04(3)	9.1(0.4)
1138.56(2)	31.5(1.8)
1140.77(2)	23.9(2.1)
1148.71(2)	19.4(0.9)
1155.42(5)	4.9(0.3)
1161.15(1)	4.1(0.8)
1164.79(3)	11.1(0.7)
1169.53(2)	20.3(0.9)
1174.42(4)	7.9(0.4)
1176.78(2)	7.5(1.3)
1180.20(4)	11.7(1.4)
1191.26(2)	19.7(0.9)
1202.02(3)	12.9(1.3)
1209.69(4)	41.3(2.5)
1210.73(8)	12.0(2.2)
1213.08(11)	3.1(0.3)
1223.34(2)	29.3(2.3)

^{187}Os -2

E[eV]	K[meV]
1226.01(3)	19.6(1.0)
1228.94(4)	7.7(0.6)
1239.43(4)	43.8(0.0)
1240.05(8)	37.6(4.6)
1241.05(5)	32.3(5.5)
1244.72(3)	3.7(0.7)
1255.70(2)	41.1(2.3)
1265.14(6)	6.3(0.4)
1268.19(4)	17.6(0.9)
1270.00(5)	10.9(0.7)
1289.20(2)	33.2(3.5)
1293.86(3)	34.1(4.1)
1296.98(3)	23.5(1.4)
1301.19(3)	41.0(2.6)
1307.27(7)	5.4(0.4)
1313.99(6)	9.7(0.9)
1315.13(7)	12.4(2.3)
1324.76(3)	6.2(0.5)
1329.22(3)	12.0(0.9)
1334.86(4)	11.7(1.3)
1341.55(3)	26.3(2.1)
1344.33(2)	36.7(3.7)
1360.92(3)	40.6(2.1)
1377.38(4)	12.0(1.3)
1382.61(2)	36.2(3.9)
1386.55(3)	18.1(0.9)
1402.44(3)	22.1(1.4)
1405.26(1)	5.7(1.2)
1409.96(3)	25.4(1.7)
1413.87(7)	6.6(1.2)
1416.22(5)	12.9(2.1)
1421.28(5)	8.2(0.8)
1428.44(1)	6.7(1.4)
1437.72(6)	14.7(0.0)
1445.19(3)	25.6(1.6)
1448.43(1)	7.1(1.4)
1452.35(1)	22.2(2.7)
1455.73(5)	10.8(1.4)

^{187}Os -2

E[eV]	K[meV]
1458.85(6)	9.7(1.0)
1484.59(3)	37.3(3.9)
1489.53(4)	10.8(1.3)
1494.85(7)	7.7(0.7)
1501.91(4)	14.8(0.8)
1507.03(4)	36.3(4.7)
1512.25(3)	37.3(5.1)
1527.27(3)	24.2(1.6)
1535.95(4)	18.6(1.0)
1541.84(6)	12.1(1.6)
1546.96(7)	26.9(3.5)
1548.13(5)	38.4(4.7)
1553.28(4)	28.4(3.1)
1558.73(2)	20.4(3.3)
1561.78(3)	29.7(2.4)
1567.42(3)	11.1(1.7)
1575.94(4)	39.0(3.3)
1581.55(4)	17.2(0.9)
1596.12(4)	16.6(0.9)
1601.30(2)	17.9(2.2)
1606.42(4)	18.8(1.1)
1612.10(7)	13.6(1.2)
1613.60(8)	12.4(2.3)
1617.27(3)	12.6(2.0)
1626.87(4)	17.8(1.5)
1633.57(1)	30.8(3.5)
1638.53(5)	8.8(0.9)
1644.15(4)	25.2(1.8)
1649.28(3)	34.1(3.4)
1655.16(4)	28.1(2.4)
1658.09(9)	6.7(0.7)
1667.92(1)	20.5(3.8)
1671.92(11)	8.0(0.7)
1674.43(4)	21.8(3.5)
1679.51(3)	7.7(1.4)
1683.43(3)	35.6(3.4)
1687.54(1)	27.1(3.7)
1711.05(4)	28.8(2.1)

^{187}Os -2

E[eV]	K[meV]
1714.52(6)	25.4(2.3)
1716.13(6)	10.3(1.8)
1725.46(4)	11.5(1.1)
1734.56(4)	34.8(4.2)
1746.38(5)	34.6(4.5)
1749.23(4)	23.2(1.8)
1756.50(7)	10.0(0.7)
1762.10(5)	19.6(1.4)
1783.56(5)	27.1(2.0)
1786.67(17)	7.9(1.0)
1788.56(7)	14.0(1.2)
1794.66(4)	40.4(4.7)
1800.14(8)	10.6(1.2)
1812.07(8)	13.0(2.0)
1826.47(6)	31.3(3.7)
1828.30(5)	40.5(4.5)
1838.51(4)	35.3(4.6)
1842.00(6)	12.5(0.9)
1854.43(2)	28.4(2.4)
1863.18(5)	34.8(3.9)
1871.55(2)	28.8(4.9)
1875.34(15)	14.6(0.0)
1881.96(4)	32.7(3.4)
1897.27(7)	16.4(1.1)
1901.93(8)	21.8(2.3)
1904.33(6)	34.4(4.0)
1915.75(10)	14.4(0.0)
1924.18(7)	41.5(5.6)
1926.29(6)	39.0(6.1)
1932.74(2)	25.4(3.9)
1945.13(2)	24.1(3.1)
1951.35(7)	28.2(4.2)
1953.53(6)	31.3(4.5)
1964.43(9)	12.8(1.6)
1973.95(5)	25.5(2.1)
1981.13(2)	28.2(5.4)
1982.38(6)	31.9(3.8)
1991.32(5)	32.7(3.2)

^{187}Os -2

E[eV]	K[meV]
2007.00(12)	8.6(0.8)
2009.78(01)	17.6(3.4)
2016.21(06)	27.8(2.8)
2020.50(01)	28.4(4.9)
2023.51(09)	36.1(6.6)
2025.97(11)	28.1(4.9)
2027.23(09)	28.6(4.7)
2037.86(06)	17.5(1.3)
2047.40(06)	40.4(5.0)
2052.85(18)	6.3(0.8)
2056.95(07)	13.8(1.0)
2062.10(08)	13.8(1.1)
2068.98(05)	21.3(1.4)
2075.75(02)	13.6(2.5)
2083.56(01)	19.1(3.5)
2088.47(07)	34.3(5.3)
2091.77(07)	35.6(4.3)
2094.39(12)	13.4(1.6)
2099.82(05)	39.1(4.8)
2105.19(03)	9.6(1.8)
2115.83(07)	19.5(3.5)
2120.12(06)	19.3(1.4)
2128.20(03)	9.3(1.8)
2133.18(11)	10.6(1.1)
2137.15(06)	26.6(2.1)
2140.43(13)	7.2(0.8)
2153.12(18)	9.6(1.5)
2155.44(08)	41.4(5.3)
2161.22(02)	8.7(1.7)
2166.75(01)	6.6(1.3)
2169.68(01)	16.3(3.1)
2187.80(06)	41.3(5.8)
2192.23(04)	18.2(3.4)
2195.66(06)	37.7(6.7)
2201.91(06)	10.2(1.7)
2207.86(07)	39.1(6.2)
2211.57(08)	37.9(6.0)
2214.81(14)	11.9(1.1)

^{187}Os -2

E[eV]	K[meV]
2219.74(01)	11.4(2.2)
2226.59(02)	25.0(4.4)
2234.70(07)	42.2(5.1)
2239.59(08)	21.9(2.2)
2243.00(00)	14.1(1.1)
2256.28(06)	42.8(2.9)
2269.81(14)	10.4(1.0)
2273.75(08)	24.8(2.2)
2280.67(07)	34.9(5.3)
2284.09(07)	32.2(4.0)
2291.08(01)	21.9(4.1)
2293.36(08)	33.7(5.2)
2299.87(08)	39.5(5.9)
2304.73(10)	41.5(5.5)
2306.89(09)	41.5(5.0)
2330.18(03)	38.4(4.5)
2343.50(00)	18.8(1.4)
2351.55(02)	36.3(3.6)
2360.96(09)	16.6(1.4)
2367.67(01)	34.2(5.8)
2374.30(08)	27.2(3.0)
2377.58(01)	13.9(2.7)
2386.96(01)	6.4(1.3)
2393.40(10)	24.5(2.6)
2400.21(07)	37.6(5.6)
2405.97(17)	8.1(0.9)
2411.79(07)	38.8(4.7)
2424.85(02)	28.0(5.2)
2431.75(09)	39.2(7.2)
2434.28(01)	15.4(3.0)
2438.55(01)	6.5(1.3)
2443.00(11)	38.2(7.3)
2444.60(11)	41.8(7.0)
2448.73(02)	11.9(2.3)
2461.62(07)	30.8(3.7)
2467.17(02)	11.5(2.2)
2471.07(09)	39.8(7.1)
2471.46(08)	39.8(6.9)

^{187}Os -2

E[eV]	K[meV]
2482.92(03)	35.6(6.7)
2485.02(09)	38.8(6.8)
2500.94(10)	16.9(1.5)
2512.76(08)	39.5(5.5)
2518.62(07)	30.5(4.4)
2520.60(21)	30.0(5.0)
2524.07(10)	22.3(2.2)
2536.81(08)	38.5(4.8)
2540.18(01)	17.0(3.3)
2545.36(14)	15.9(1.6)
2553.85(08)	27.5(4.0)
2555.49(05)	29.3(5.3)
2563.41(11)	29.7(5.5)
2564.88(07)	26.7(3.6)
2571.29(02)	7.6(1.5)
2576.65(13)	26.9(4.9)
2578.13(03)	30.7(5.3)
2583.14(02)	11.2(2.2)
2588.15(07)	33.3(4.9)
2600.98(07)	37.4(5.2)
2610.11(07)	42.2(4.9)
2615.00(00)	12.3(1.4)
2620.38(08)	42.8(4.8)
2627.62(02)	13.4(2.7)
2630.20(10)	40.3(6.0)
2637.19(01)	11.4(2.3)
2641.14(08)	38.2(5.2)
2661.48(02)	26.7(5.0)
2666.79(02)	17.5(3.6)
2671.04(12)	16.1(1.5)
2684.53(11)	37.9(6.5)
2686.53(11)	40.9(6.9)
2695.89(02)	29.3(5.4)
2701.72(02)	17.1(3.3)
2711.62(11)	39.0(7.9)
2713.96(09)	36.8(7.4)
2720.15(09)	28.4(3.3)
2730.91(10)	21.5(2.0)

^{187}Os -2

E[eV]	K[meV]
2742.43(10)	37.9(4.9)
2746.50(10)	35.7(6.0)
2751.96(08)	35.5(5.7)
2756.14(21)	11.7(1.6)
2765.30(08)	38.2(6.7)
2774.91(10)	38.4(7.0)
2778.04(16)	17.9(2.1)
2785.21(10)	35.0(5.2)
2790.70(10)	38.7(5.4)
2801.00(07)	38.5(5.3)
2810.27(10)	41.4(5.2)
2816.92(14)	20.9(2.4)
2821.74(18)	27.9(4.3)
2823.03(12)	28.2(4.3)
2832.47(11)	20.8(2.0)
2839.82(01)	7.0(1.4)
2848.55(01)	13.3(2.7)
2857.43(02)	29.8(5.1)
2868.97(01)	29.4(5.2)
2877.51(13)	38.6(6.0)
2882.00(10)	39.8(6.1)
2888.79(10)	30.6(4.1)
2902.61(12)	39.9(7.5)
2907.21(11)	39.6(7.3)
2913.23(01)	9.0(1.8)
2926.03(16)	14.6(1.6)
2930.70(02)	11.3(2.2)
2939.07(15)	28.2(4.0)
2940.88(02)	27.4(5.1)
2952.73(05)	35.2(6.4)
2956.29(12)	37.5(7.1)
2968.61(08)	37.6(5.4)
2980.97(11)	37.7(7.1)
2985.92(13)	36.5(7.0)
2991.48(16)	40.0(8.1)
2993.54(14)	41.3(7.6)

^{187}Os -2 (Table E.4)

All spins defined as s-wave (l=0).

Table E.5: Resonance parameters of ^{188}Os -1

E[eV]	Γ_γ[meV]	$g\Gamma_n$[meV]
38.68(0)	37.0(0.0)	55.0(0.0)
78.739(2)	35.6(0.5)	377.9(0.0)
150.066(3)	37.4(0.2)	159.8(1.0)
191.922(3)	36.1(0.3)	120.0(1.0)
254.208(3)	52.0(0.0)	77.1(1.0)
282.441(3)	52.0(0.0)	12.3(0.1)
317.23(0)	57.5(0.5)	960.8(0.0)
388.37(2)	43.8(0.5)	812.2(0.0)
478.92(2)	43.5(0.5)	490.1(0.0)
528.774(5)	52.0(0.0)	136.5(2.7)
536.97(1)	52.0(0.0)	125.9(2.7)
620.55(1)	52.0(0.0)	184.2(3.9)
649.55(1)	52.0(0.0)	130.0(4.1)
705.99(1)	52.0(0.0)	141.3(4.8)
745.70(2)	48.6(0.7)	313.0(0.0)
781.51(5)	44.6(1.0)	1125.(0.)
819.95(1)	52.0(0.0)	64.0(3.4)
844.41(6)	44.6(1.0)	1870.(0.)
863.11(1)	44.0(0.8)	380.0(0.0)
900.27(2)	52.0(0.0)	2.9(0.5)
980.03(1)	46.5(0.9)	140.0(0.0)
1001.523(3)	52.0(0.0)	41.0(0.0)
1042.15(2)	48.0(0.7)	529.2(0.0)
1079.76(1)	52.0(0.0)	20.2(0.5)
1107.78(4)	51.9(0.8)	1280.(0.)
1182.74(1)	52.0(0.0)	43.0(0.0)
1216.67(1)	64.6(1.1)	179.3(11.0)
1293.22(2)	52.0(0.0)	86.0(0.0)
1316.53(3)	52.1(1.0)	936.3(0.0)
1347.89(2)	54.1(1.8)	170.0(0.0)
1413.27(5)	59.5(1.2)	1330.(0.)
1485.60(2)	63.2(4.2)	94.5(13.0)
1520.35(2)	48.1(1.3)	122.0(0.0)
1544.931(4)	52.0(0.0)	52.0(0.0)
1598.14(7)	51.4(1.1)	1730.(0.)
1625.26(1)	52.0(0.0)	3.1(0.6)

^{188}Os -1

E[eV]	Γ_γ[meV]	$g\Gamma_n$[meV]	E[eV]	Γ_γ[meV]	$g\Gamma_n$[meV]
1673.73(4)	47.1(1.0)	678.1(0.0)	3056.03(8)	62.7(2.0)	730.0(0.0)
1719.94(2)	54.3(1.4)	113.0(0.0)	3113.30(8)	54.8(2.0)	403.0(0.0)
1764.43(1)	52.0(0.0)	5.0(1.0)	3128.95(8)	58.3(2.2)	210.0(0.0)
1779.50(3)	52.0(0.0)	63.0(0.0)	3186.54(12)	55.7(2.4)	4390.(0.)
1803.43(2)	57.8(1.4)	202.0(0.0)	3208.81(8)	55.9(2.2)	437.0(0.0)
1876.87(6)	45.2(1.1)	1020.(0.)	3269.43(9)	52.0(0.0)	49.0(4.2)
1905.748(3)	52.0(0.0)	42.0(0.0)	3284.27(7)	51.4(1.8)	448.0(0.0)
1967.62(1)	52.0(0.0)	113.0(0.0)	3355.03(6)	61.1(2.4)	237.0(0.0)
1971.65(3)	47.3(1.3)	303.9(0.0)	3417.95(8)	56.9(2.1)	360.0(0.0)
2017.89(3)	52.0(0.0)	84.6(6.3)	3438.86(8)	49.8(1.9)	528.0(0.0)
2049.07(9)	52.0(0.0)	5.9(0.4)	3486.12(8)	52.0(0.0)	59.9(4.9)
2092.24(3)	55.0(1.5)	219.0(0.0)	3517.56(01)	52.0(0.0)	7.0(1.4)
2138.05(3)	56.3(1.6)	306.0(0.0)	3600.22(10)	59.7(2.2)	786.1(0.0)
2179.42(2)	52.0(0.0)	21.4(3.8)	3632.02(01)	52.0(0.0)	10.0(2.0)
2191.59(5)	50.6(1.7)	351.1(0.0)	3660.31(01)	52.0(0.0)	15.0(3.0)
2257.79(1)	52.0(0.0)	5.0(1.0)	3668.31(02)	52.0(0.0)	20.2(3.9)
2274.38(5)	48.0(1.3)	540.9(0.0)	3695.02(20)	44.9(2.4)	1790.(0.)
2298.98(8)	50.1(1.5)	1360.(0.)	3706.35(52)	35.2(3.0)	4590.(0.)
2386.82(1)	52.0(0.0)	93.1(17.1)	3719.78(11)	55.9(2.5)	763.0(0.0)
2412.06(7)	47.1(1.5)	762.0(0.0)	3732.94(02)	52.0(0.0)	9.3(1.8)
2438.33(4)	52.6(1.7)	233.0(0.0)	3772.65(13)	52.0(0.0)	41.1(3.9)
2500.93(7)	45.3(1.4)	715.1(0.0)	3883.98(10)	62.1(2.4)	703.0(0.0)
2504.78(3)	52.0(0.0)	2.8(0.6)	3929.04(01)	52.0(0.0)	20.3(4.0)
2545.05(1)	52.0(0.0)	52.7(10.0)	3931.48(01)	52.0(0.0)	92.0(0.0)
2570.83(2)	46.8(1.6)	267.0(0.0)	3947.53(10)	56.3(3.1)	134.0(0.0)
2613.22(15)	52.0(0.0)	5.7(0.6)	3966.66(10)	59.0(3.6)	111.0(0.0)
2619.76(1)	52.0(0.0)	4.0(0.8)	3982.07(03)	52.0(0.0)	19.8(4.0)
2626.82(4)	55.5(2.2)	253.0(0.0)	3987.38(12)	52.0(0.0)	109.0(0.0)
2729.12(12)	52.0(0.0)	9.6(0.7)	4106.33(12)	52.0(0.0)	196.3(35.3)
2768.44(1)	52.0(0.0)	29.9(6.0)	4134.73(01)	52.0(0.0)	102.0(17.2)
2799.50(11)	52.0(0.0)	11.6(0.8)	4215.40(10)	65.1(3.3)	208.0(0.0)
2815.79(6)	52.0(0.0)	196.1(29.4)	4236.28(17)	55.9(2.4)	1451.(0.)
2864.00(6)	52.0(0.0)	118.6(12.5)	4268.21(19)	46.7(2.4)	1600.(0.)
2924.14(2)	52.0(0.0)	10.1(2.0)	4313.22(12)	52.0(0.0)	96.4(11.4)
2967.98(8)	52.0(0.0)	5.2(1.0)	4341.27(14)	52.0(0.0)	46.1(4.4)
2975.72(13)	47.3(1.9)	1670.(0.)	4434.27(06)	58.4(9.5)	263.0(0.0)
2988.42(6)	52.0(0.0)	154.9(18.9)	4450.93(16)	55.9(2.6)	1310.(0.)
3036.60(7)	58.4(1.8)	600.0(0.0)	4483.01(16)	52.0(0.0)	65.0(0.0)
^{188}Os -1			^{188}Os -1		

E[eV]	Γ_γ[meV]	$g\Gamma_n$[meV]
4579.92(12)	60.5(6.2)	129.8(23.3)
4603.79(06)	52.0(0.0)	49.0(9.4)
4628.01(02)	52.0(0.0)	10.0(2.0)
4641.47(25)	50.5(2.9)	2150.(0.)
4722.68(15)	50.7(3.0)	198.0(0.0)
4746.96(14)	56.0(3.3)	242.0(0.0)
4817.55(11)	54.2(8.3)	160.0(0.0)
4852.49(20)	50.0(3.0)	300.0(0.0)
4881.95(20)	50.2(2.9)	950.1(0.0)
4893.85(15)	56.8(3.5)	269.0(0.0)
4933.39(16)	52.0(0.0)	86.2(15.8)
4959.80(08)	47.9(7.7)	194.0(0.0)

^{188}Os -1 (Table E.5)

All spins defined as s-wave l=0, J=0.5 (g=1).

Table E.6: Resonance parameters of ^{188}Os -2

E[eV]	K[meV]
4989.75(08)	36.8(6.0)
5054.83(17)	44.0(8.0)
5094.82(04)	11.8(2.3)
5102.32(07)	47.7(6.9)
5163.11(17)	50.3(0.0)
5204.25(03)	22.8(4.5)
5211.34(02)	28.8(5.5)
5246.54(20)	41.3(7.0)
5273.56(03)	37.0(7.1)
5337.24(02)	13.3(2.7)
5350.27(02)	40.7(7.7)
5383.97(01)	25.2(5.1)
5401.93(18)	45.5(8.9)
5437.43(19)	47.4(9.2)
5455.92(19)	38.3(6.0)
5525.35(25)	47.6(9.0)
5562.64(26)	50.1(7.0)
5613.52(03)	38.4(7.1)
5634.56(01)	25.9(5.1)
5666.13(19)	42.3(7.1)
5734.31(23)	47.8(7.4)
5785.24(02)	44.6(7.6)
5829.58(25)	46.9(8.9)
5890.21(23)	41.9(8.0)
5907.67(27)	50.3(0.0)
5971.09(28)	47.1(9.3)
5996.10(31)	46.8(8.6)
6044.67(11)	42.1(8.0)
6104.952(4)	34.4(6.8)
6130.69(01)	14.4(2.9)
6183.73(28)	46.4(8.9)
6200.98(42)	51.0(7.6)
6250.33(29)	48.2(9.1)
6287.38(25)	24.5(3.9)
6335.08(36)	46.5(8.3)
6376.45(24)	41.8(7.4)

^{188}Os -2

E[eV]	K[meV]
6426.43(22)	46.6(8.8)
6458.35(04)	31.6(6.3)
6485.52(25)	43.4(8.1)
6531.91(46)	45.8(9.0)
6536.70(29)	37.3(6.9)
6552.94(38)	11.6(2.0)
6605.59(10)	39.1(7.1)
6640.15(01)	37.9(7.3)
6689.60(12)	34.0(6.6)
6711.04(31)	46.8(9.0)
6776.33(02)	38.9(7.6)
6815.15(30)	43.8(8.1)
6899.58(04)	44.9(8.7)
6943.11(02)	43.1(8.4)
6959.13(29)	43.1(7.7)
6993.97(01)	20.9(4.2)
7021.82(30)	46.2(8.8)
7067.64(01)	34.5(6.8)
7123.46(05)	44.9(8.7)
7161.65(01)	30.1(6.0)
7193.70(03)	42.5(7.7)
7233.28(34)	43.3(8.2)
7260.27(34)	46.7(9.2)
7279.47(28)	44.6(8.3)
7325.67(34)	45.4(8.8)
7372.49(05)	32.8(6.6)
7384.21(02)	43.3(8.3)
7443.22(36)	42.4(7.7)
7475.32(03)	41.5(8.1)
7501.36(08)	34.5(6.8)
7546.29(01)	30.0(6.0)
7585.96(02)	39.0(7.6)
7641.17(41)	42.4(7.3)
7700.73(03)	30.0(6.0)
7733.53(38)	41.9(7.5)
7779.48(03)	40.8(7.9)
7877.25(49)	38.3(6.5)
7891.27(01)	27.9(5.6)

^{188}Os -2

E[eV]	K[meV]
7960.26(42)	34.5(4.7)

^{188}Os -2 (Table E.6)

All spins defined as s-wave l=0, J=0.5 (g=1).

Appendix F : Galactic chemical evolution model

Studies of chemical evolution aim primarily to account for the distribution and abundances of the chemical elements in the stars and interstellar matter of galaxies. Nucleocosmochronology employs this knowledge to obtain information about time scales over which the solar system elements were synthesized.

In 1970s, sophisticated models of Galactic chemical evolution were introduced (for details on, see e.g. Tinsley (1980) [92]). In order to perform age determinations within the framework of cosmochronology, several r-process chronometer pairs have been investigated (for a general review see Ref. [16]). These calculations start from basic equations.

The total mas M_T consists of the gas mass M_G and the mass locked up in stars M_*. It can be written as $M_T = M_G + M_*$.

With all of these definitions and assumptions, the basic equations for chemical evolution follow,

$$\frac{dM_T(t)}{dt} = f(t). \tag{F.1}$$

$$\frac{dM_G(t)}{dt} = -\psi(t) + R(t)\psi(t) + f(t) - o. \tag{F.2}$$

Where
$f(t)$: the infalling gas into the disk from the galactic halo.
$\psi(t)$: the star-formation rate (SFR), the mass of gas turned into stars per unit time.
$R(t)$: the fraction mass ejected by stars during and at the end of their evolution.
$R(t)\psi(t)$: for the total ejection rate from those stars which had formed before.
o : a possible outflow into the galactic halo.

Basing on Eq. (F.2), it is possible to use the equation with the number of nuclei of nuclei of species i with decay rate for nuclei i, λ_i,

$$\begin{aligned}\frac{dN_i(t)}{dt} &= -\lambda_i N_i(t) + P_i\psi(t) - \underbrace{\left[\frac{1-R}{M_G}\psi(t) - \frac{f(t)}{M_G}\frac{Z_f}{Z} + \frac{o}{M_G}\right]}_{\omega(t)} N_i(t) \\ &= -\lambda_i N_i(t) + P_i\psi(t) - \omega(t)N_i(t) = -\lambda_i N_i(t) + B(t, N_i). \end{aligned} \tag{F.3}$$

The infall ($f(t)$) term has to be modified because of the contribution of the infalling gas. The abundance of a heavy nucleus i is then reduced according to its lower metallicity[4] Z_f, in comparison with the disk metallicity Z. $P_i\psi(t)$ describes the number of nuclei i being newly synthesized in material processed during stellar evolution and explosive processing. Finally the general equation governing the time evolution of the abundance N_i can be simply written with $B(t, N_i)$ $(= P_i\psi(t) - \omega N_i(t))$, the net time-dependent production function.

Taking into account infall, realistic assumptions for its amount and time dependence are necessary and solutions can be found numerically, e.g. by SW [93], Clayton [25], Yokoi et al. [85]. Using the Re/Os clock with Galactic chemical evolution models, Yokoi et al. [85] and Clayton [25] showed values is the approximate ranges $11 \lesssim T_G \lesssim 15$ Gyr and $14 \lesssim T_G \lesssim 20$ Gyr respectively. Clearly the yield evaluation also requires the modeling of a various stars with different masses and metallicities. Recent works for the Re/Os clock can be found in [94] [95].

---

[4] The metallicity of an object is the proportion of its matter made up of chemical elements other than hydrogen and helium.

Bibliography

[1] E.M. Burbidge, G.R. Burbidge, W.A. Fowler and F. Hoyle, Rev. Mod. Phys. **29**, 547 (1957).

[2] G. Wallerstein *et al.*, Rev. Mod. Phys. **69**, 995 (1997).

[3] J.N. Bahcall, Nucl. Phys. **B (Proc. Suppl.) 118**, 77 (2003).

[4] M.H. Ahn *et al.*, Phys. Rev. **D74**, 072003 (2006).

[5] D. Bemmerer *et al.* (The LUNA Collaboration), Eur. Phys. J. **A27**, s01, 161 (2006).

[6] F. Käppeler *et al.*, Annu. Rev. Nucl. Part. Sci. **48**, 175 (1998).

[7] R.N. Boyd, *Heavy Elements and Related New Phenomena*, Volume II, Chap. 22 (World Scientific Publishing Company, 1999).

[8] F. Käppeler, A. Mengoni, Nucl. Phys. **A777**, 291 (2006).

[9] F. Käppeler, H. Beer, and K. Wisshak, Rep. Prog. Phys. **52**, 945 (1989).

[10] J.J. Cowan, F.K. Thielemann and J.W. Truran, Physics Reports, Vol. **208**, Issue 4-5, 267 (1991).

[11] H. Schats *et al.*, Phys. Rep. **294**, 167 (1998).

[12] C. Fröhlich *et al.*, Phys. Rev. Lett, Vol. **96**, 142502 (2006).

[13] M. Arnould and S. Goriely, Phys. Rep. **384**, 1 (2003).

[14] E. Anders, N. Grevesse, Geochim. et Cosmochim. Acta, **53**, 197 (1989).

[15] G.R. Tilton, *Meteorites and the Early Solar System*, p.259 (Univ. Arizona Press, Tucson, 1988).

[16] J.J. Cowan, F.K. Thielemann and J.W. Truran, Annu. Rev. Astron. Astrophys. **29**, 447 (1991).

[17] J.J. Cowan *et al.*, Ap. J. **521**, 194 (1999).

[18] H.R. Butcher, Nature **328**, 127 (1987).

[19] B.E.J. Pagel, *Evolutionary Phenomena in Galaxies*, ed J.E. Beckman and B.E.J. Pagel, p.201 (Cambridge Univ. Press, Cambridge, 1989).

[20] M. Galeazzi *et al.*, Phys. Rev. **C63**, 014302 (2000).

[21] D.D. Clayton, Ap. J **139**, 637 (1964).

[22] F. Bosch *et al.*, Phys. Rev. Lett. **77**, 5190 (1996).

[23] H. Feshbach, C.E. Porter and V.F. Weisskope, Phys. Rev. **C96/2**, 448 (1954).

[24] M. Mosconi *et al.*, Nuclear Data for Science and Technology, **Vol.2**, eds. O. Bersillon*et al.* 1307 (CEA, Paris, 2007).

[25] D.D. Clayton, Mon. Not. R. Astro. Soc. **234**, 1 (1988).

[26] http://neutrons.ornl.gov/

[27] http://www.j-parc.jp/

[28] P. Mastinu et al. in preparation.

[29] L.P. Chau *et al.*, Proceedings of EPAC 2006, Edinburgh, Scotland, TUPLS082, 1690 (2006).

[30] http://www.talys.eu/

[31] ORNL/PSR-201, RSICC PERIPHERAL SHIELDING ROUTINE COLLECTION ESTIMA, Radiation safety information computational center.

[32] http://www.cern.ch/ntof

[33] C. Borcea *et al.*, Nucl. Instr. Meth. **A513**, 523 (2003).

[34] U. Abbondanno *et al.* (The n_TOF Collaboration), Report CERN-SL-2002-053 ECT (2003).

[35] G. Lurusso *et al.* (The n_TOF Collaboration), Nucl. Instr. and Meth. **A532**, 622 - 630 (2004).

[36] R. Plag *et al.* (The n_TOF Collaboration), Nucl. Instr. Meth. **A496**, 425 (2003).

[37] S. Marrone *et al.*, Nucl. Instr. Meth. **A517**, 389 (2004).

[38] F. Corvi *et al.*, Nucl. Sci. Eng. **107**, 272 (1991) ; J.N. Wilson, *et al.* Nucl. Instr. Meth. **A511**, 388 (2003).

[39] U. Abbondanno *et al.* (The n_TOF Collaboration), Nucl. Instr. Meth. **A521**, 454 (2004).

[40] G. Aerts *et al.*, Report DAPNIA-04-106, (CEA/Saclay France, 2004).

[41] M. Mosconi, PhD thesis, (University of Karlsruhe Germany, 2007).

[42] N. Larson, Report ORNL/TM-9179/R7 (Oak Ridge National Laboratory, 2006).

[43] M.C. Moxson and E.R. Brisland, AEA-InTec-0630, (AEA Technology, 1991).

[44] S.F. Mughabghab, *Atlas of Neutron Resonances* (Elsevier, 2006).

[45] S.F. Mughabghab, *Neutron Cross Sections* Vol.1 (Academic Press, New York, 1981).

[46] S. Kopecky, P. Siegler and A. Moens, Proceedings of the International conference on Nuclear Data for science and Technology, France, p623 (2007).

[47] S. Kopecky, private communication (2008).

[48] T.A. Brody *et al.*, Rev. Mod. Phys. **Vol.53, No.3**, 385 (1981).

[49] M.V. Berry, M. Robnik *et al.*, J. of Phys. **A17**, 2413 (1984).

[50] F.J. Dyson and M.L. Mehta, J. of Math. Phys. **4**, 701 (1963).

[51] D. Kilbane *et al.*, Chaos, Solitons and Fractals **30**, 412 (2006).

[52] C.E. Poter and R.G. Thomas, Phys. Rev. **104**, 483 (1956).

[53] M. Moore *et al.*, Phys. Rev. **C18**, 1328 (1978).

[54] H.I. Liou and J. Rainwater, Phys. Rev. **C6/2**, 435 (1972).

[55] J.C. Browne and B.L. Berman, Phys. Rev. **C23**, 1434 (1981).

[56] R.R. Winters *et al.*, Phys. Rev. **C34**, 840 (1986).

[57] R.R. Winters and R.L.Macklin, Phys. Rev **C25/1**, 208 (1982).

[58] W.A. Fowler, Bull. Am. Astron. Soc. **4**, 412 (1972).

[59] R. Gallino *et al.*, Ap. J. **497**, 388 (1998).

[60] F. Käppeler *et al.*, Ap. J. **366**, 605 (1991).

[61] W.A. Fowler and F. Hoyle, Ann. Phys. **10**, 280 (1960).

[62] W.A. Fowler, Rev. Mod. Phys **56**, No.2, Part I, 149 (1984).

[63] W.A. Fowler, Proceedings of the Welch Foundation Conferences on Chemical Research XXI Cosmochemistry, ed. W.D. Milligan, (1977).

[64] M. Mosconi *et al.* (The n_TOF Collaboration), in preparation.

[65] Z. Bao *et al.*, Atomic data Nucl. Data tables **76**, 70 (2000).

[66] T. Fästermann, Proceedings of the 9th Workshop on Nuclear Astrophysics, Germany, 172 (1998).

[67] S.E. Woosley and W.A. Fowler, Ap. J. **233**, 411 (1979).

[68] A. Gilbert and A.G. Cameron, Can. J. Phys. **43**, 1446 (1965).

[69] A. Mengoni, M. Mosconi, K. Fujii and F. Käppeler, Proceedings of the International Workshop on "The Origin of the Elements heavier than Iron", Torino Italy, Publications of the Astronomical Society of Australia, in press (2009).

[70] P.A. Moldauer, Nucl. Phys. **47**, 65 (1963).

[71] B.L. Berman *et al.*, Phys. Rev. **C19/4**, 1205 (1979).

[72] S. Hilaire, Ch. Lagrange and A.J. Koning, Ann. Phys. **306**, 209 (2003).

[73] R.R. Winters *et al.*, Bull. Am. Phys. Soc. **24**, 854 (1979).

[74] R.R. Winters *et al.*, Phys. Rev. **C21/2**, 563 (1980).

[75] L.L. Litvinsky *et al.*, Phys. At. Nucl. (translation of Yad. Fiz), **58(2)**, 164 (1995).

[76] R.L. Macklin and R.R. Winters *et al.*, Ap. J. **274**, 408 (1983).

[77] R.L. Hershberger and R.L. Macklin *et al.*, Phys. Rev. **C28**, 2249 (1983).

[78] R.R. Winters, R.L. Macklin and R.L. Hershberger, Astron. Astrophys. **171**, 9 (1987).

[79] M.T. McEllistrem *et al.*, Phys. Rev. **C40/2**, 591 (1989).

[80] T. Shizuma *et al.*, Phys. Rev. **C72**, 025808 (2005).

[81] S. Müller *et al.*, Phys. Rev. **C73**, 025804 (2006).

[82] M. Segawa *et al*, Phys. Rev. **C76**, 022802 (2007).

[83] M. Arnould, K. Takahashi and K. Yokoi, Astron. Astrophys. **137**, 51 (1984).

[84] R. Gallino, private communication (2009).

[85] K. Yokoi, K. Takahashi and M. Arnould, Astron. Astrophys. **117**, 65 (1983).

[86] L.M. Krauss and B. Chaboyer, Science **299**, 65 (2003).

[87] B.M.S. Hansen *et al.*, arXiv:0701738v2 [astro-ph] (2007).

[88] G. Hinshaw *et al.*, arXiv:0803.0732v1 [astro-ph] (2008).

[89] N. Dauphas, Nature **435/30**, 1203 (2005).

[90] http://www.kadonis.org/

[91] F. Gunsing, SAMMY users meeting, ND2004 at Santa Fe, (2004).

[92] B.M. Tinsely, Fond. Cosmic Phys. **5**, 287 (1980).

[93] D.N. Schramm and G.J. Wasserburg, Ap. J. **162**, 57 (1970).

[94] K. Takahashi *et al.*, Proceedings of the 9th Workshop on Nuclear Astrophysics, Germany, 175 (1998).

[95] K. Takahashi, Nucl. Phys. **A718**, 325c (2003).

Acknowledgments

This my work was supported by many persons. I thank everyone who contributed to this work. I am really glad to be gifted with kind and powerful colleagues.

First of all I appreciate for Prof. Stella and Prof. Montagnoli's supports of the doctor course.

Sincerely I thank Dr. Milazzo and Dr. Mastinu, they taught and helped me huge things.

For interesting considerations concerning Astrophysics, I thank Dr. Käppeler who advised me many important things, and Prof. Gallino who provided his calculations and many information.

I am also indebted to Dr. Kopecky for useful discussions on sample inhomogeneities.

I owe much Dr. Mengoni for the statistical analysis and theoretical calculations.

Dr. Mosconi, the basic data of my works are mainly contributed by her.

To Dr. Tagliente, Dr. Gunsing and Dr. Domingo-Pardo, I thank for all their supports and helps on SAMMY resonance analysis.

I would also like to thank to members of Italian n_TOF group, especially the great leader Dr. Colonna. I could do fruitful discussions with them.

Of course I would like to say thanks to n_TOF collaborators, this experiment is accomplishment by all of them.

Also Cristian, Marco, Francesca, Carlo, Lucia and members of the group III at INFN Trieste, my works could not be completed without their supports. I thank all of them.

Finally I write down special thanks to my family, Jun.